

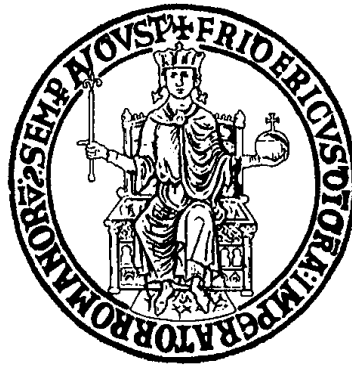
**Università degli Studi di Napoli Federico II**

**Dipartimento di Strutture per l'Ingegneria e l'Architettura**

PhD Programme in Seismic Risk

Coordinator: Professor Aldo Zollo

XXVII Cycle



PhD Thesis of

Georgios Baltzopoulos

**STRUCTURAL PERFORMANCE  
EVALUATION IN NEAR-SOURCE  
CONDITIONS**

Advisor

Professor Iunio Iervolino

# INDEX

Research Framework	v
Acknowledgements	vi
List of figures	viii
CHAPTER 1	2
INTRODUCTION	
1.1 Motivation	2
1.1.1 Near-Source Effects and Forward Directivity	3
1.1.2 Engineering Seismology Perspective on Directivity	4
1.1.3 Directivity from an Earthquake Engineering Perspective	6
1.2 Organization of the Thesis	8
Chapter 1 References	10
CHAPTER 2	12
INELASTIC DISPLACEMENT RATIO OF NEAR-SOURCE PULSE-LIKE GROUND MOTIONS	
2.1 Introduction	12
2.2 Dataset and Empirical Evidence	14
2.3 Functional Form and Regression Strategy	16
2.4 Results and Discussion	17
2.5 Conclusions	19
Chapter 2 References	21
CHAPTER 3	24
THE DISPLACEMENT COEFFICIENT METHOD IN NEAR- SOURCE CONDITIONS	
3.1 Introduction	24
3.2 The Displacement Coefficient Method	25
3.3 Displacement Ratios of Ordinary and Pulse-like Records	28
3.4 Near-Source Hazard, Disaggregation and Inelastic Demand	30
3.4.1 Near-Source Probabilistic Seismic Hazard Analysis	30
3.4.2 Hazard Disaggregation and Near-Source Inelastic Demand	31
3.5 Design Scenarios and Building Models	33
3.5.1 Probabilistic Hazard With and Without Pulse Like Effects	33

3.5.2 Disaggregation Results	37
3.5.3 Structural Models	37
3.6 Implementing the DCM in NS Conditions	39
3.7 DCM versus Non-Linear Dynamic Analysis	45
3.7.1 Selection of Ordinary Records	45
3.7.2 Selection of Pulse-Like Records	46
3.7.3 Non-Linear Response History Analyses	49
3.8 Discussion	50
Chapter 3 References	52
 CHAPTER 4	 56
BUILDING AN EXTENDED DATABASE OF NEAR-SOURCE GROUND MOTIONS AFFECTED BY DIRECTIVITY	
4.1 Introduction	56
4.2 Methodology	57
4.3 Seismic Events Considered	60
4.3.1 Parkfield, California 2004 Earthquake	60
4.3.2 New Zealand 2010 and 2011 Events	60
4.3.3 Chichi, Taiwan 1999 Earthquake	62
4.3.4 Other Notable Seismic Events	65
4.4 Results and Discussion	66
Chapter 4 References	69
 CHAPTER 5	 72
NEAR-SOURCE PULSE-LIKE SEISMIC DEMAND FOR MULTI- LINEAR BACKBONE OSCILLATORS	
5.1 Introduction	72
5.2 Incremental Dynamic Analysis and the <i>SPO2IDA</i> Tool	74
5.3 Modelling Near-Source Pulse-Like Demand for Tri-Linear Backbone Oscillators	77
5.3.1 Predictor Variables	77
5.3.2 Hysteretic Rule	78
5.3.3 Equivalent Ductility Concept	79
5.3.4 Scope of the Model	81
5.4 Development of the Analytical Model	83
5.4.1 Intermediate Steps Towards Attaining the Full Model	83

5.4.2 Curve-Fitting Strategy and Functional Forms	84
5.4.2.1 Bilinear oscillators with hardening post-yield behavior	84
5.4.2.2 Bilinear oscillators with softening (negative slope) post-yield behavior	87
5.4.2.3 Full trilinear backbone oscillator	91
5.5 Discussion of the Results	92
5.5.1 Comparison with Chapter 2 Data	92
5.5.2 Curve-Fitting versus Regression	94
5.5.3 Potential Applications	97
Chapter 5 References	101
 CHAPTER 6	 104
SUMMARY AND CONCLUSIONS	
APPENDIX A	109
APPENDIX B	112
APPENDIX C	120

## **Research Framework**

Parts of the work presented in this thesis have been developed within the activities of the the following projects:

*Rete dei Laboratori Universitari di Ingegneria Sismica (ReLUIS) 2010-2013 and 2014-2018 research programs.*

*Harmonized Approach to Stress Test for Critical Infrastructures Against Natural Hazard (STREST) project, as part of the activities of AMRA (Analisi e Monitoraggio dei Rischi Ambientali scarl).*

*Strumenti e Tecnologie per la gestione del Rischio delle Infrastrutture di Trasporto (STRIT) 2012-2015 project of the Italian Ministry of Education, University and Scientific Research (Ministero dell'Istruzione, dell'Università e la Ricerca Scientifica) as part of the activities of AMRA (Analisi e Monitoraggio dei Rischi Ambientali scarl).*

AXA-DiSt 2014-2017 research program of AXA-Matrix Risk Consultants, Milan, Italy and Dipartimento di Strutture per l'Ingegneria e l'Architettura.

## **Acknowledgements**

First and foremost, I owe thanks to my advisor, professor Iunio Iervolino. In the past three-and-a-half years, I came to realize that whenever professor Iervolino decides to tackle an academic problem, he does so with an intensity that renders him a force to be reckoned with. For this, I consider myself fortunate to have worked under his guidance.

I should also like to thank Dr. Eugenio Chioccarelli, not only for the support he gave me during my studies, but also for our harmonious collaboration, which speaks highly of his character.

Another thanks is due to professor Dimitris Vamvatsikos, not only for sharing his invaluable expertise with me but also for the warm academic hospitality he provided during my Attic sojourn.

Finally, I would be remiss if I neglected to thank my parents, Thomas and Daphne, for their unwavering and steadfast support.



# LIST OF FIGURES

Figure 1.1. Initial segment of the acceleration and velocity time history of the fault-normal component of ground motion recorded on the left abutment of the Pacoima Dam, during the 1971 San Fernando (California) earthquake. Impulsive waveform in the velocity record (Baker, 2008) indicated in red. .... 2

Figure 1.2. Snapshot of wave fronts; pictorial representation of the directivity of seismic energy adapted from Singh (1985). .... 3

Figure 1.3. Velocity time-history of the TCU068 record from the 1999 Chichi (Taiwan) earthquake. Typical example of a fling-step pulse. .... 4

Figure 2.1. (a) Elastic 5% damped spectra for FN pulse-like with  $1s < T_P < 2s$  and ordinary records; (b) empirical  $C_R$  for FN pulse-like records, for their FP components, and for ordinary records, at  $R = 4$ . .... 15

Figure 2.2. (a) Fitting of Equation (2.4) for pulse-like FN data ( $R = 4$ ) outside the  $]0.35, 0.775[ T/T_p$  range, and (b) fitting of Equation (2.6) for selected R-values. .... 18

Figure 2.3. (a) Double-bump fitted  $C_R$  trends; (b) comparison with empirical data for  $R = 4$ . .... 19

Figure 3.1: Inelastic displacement ratio of near-source pulse-like ground motions according to Iervolino et al. (2012). .... 29

Figure 3.2. Schematic representation of site-source configuration for the design scenarios considered. .... 33

Figure 3.3. Uniform hazard spectra computed for the various design scenarios by either performing classical PSHA calculations (a) or by considering NS-FD effects in the hazard computation (b). .... 35

Figure 3.4. PDFs of pulse period  $T_p$ , resulting from disaggregation of NS hazard, conditional on pulse occurrence and  $S_a(T) = s_a$ , referring to 2745yr return period for each scenario (histograms normalized to unit area). Dashed lines indicate the location of the mean,  $E[T_p | S_a = s_a]$ , whose value is also shown along with standard deviation  $\sigma_{T_p | S_a = s_a}$ . .... 37

Figure 3.5. Geometry, detailing (flexural reinforcement), modal information and pushover curves for the three R/C frames used in the application. .... 40

Figure 3.6. Graphical representation of application of the DCM for a 4-storey R/C frame ( $T=0.50s$ ) at Site A under G-R seismicity. Target displacement estimates for

near collapse performance level (TR=2475 yr) considering impulsive (a) and non-impulsive (ordinary) contributions (b)..... 42

Figure 3.7. Response spectra of the ordinary (a) and pulse-like (b) scaled records selected for the non-linear dynamic analysis of the 5-storey R/C frame (T=0.75s). Also shown is the NS uniform hazard (design) spectrum of the considered scenario and – in the case of the ordinary record set – the target conditional mean spectrum. .... 47

Figure 3.8. (a) PDF of pulse period from disaggregation of NS hazard (T=1.00s, TR=975 yr) and (b) corresponding CDF multiplied by intended number of pulse-like records to be selected and divided into five bins of equal probability for the calculation of inelastic displacement ratio corresponding to the average pulse period of each bin..... 48

Figure 3.9. Comparison of target densities of pulse period with  $T_p$  histograms of the selected pulse-like ground motion sets for the T=0.75s five-storey frame (a) and the T=1.00s six-storey frame (b). The probability densities have been scaled in order for their areas to coincide with those of the histograms. Relevant statistics also are shown. .... 49

Figure 3.10. Histograms of maximum inelastic roof displacement resulting from non-linear dynamic RHA for the five-storey ( $T_1=0.75s$ ) frame subjected to the pulse-like (a) and ordinary (b) excitation suite as well as the respective results for the six-storey ( $T_1=1.00s$ ) frame (c) and (d). .... 50

Figure 4.1: Examples of velocity pulses attributable to various causes (candidate pulses displayed in red). (a) Styx Mill Transfer Station record from the Darfield (New Zealand) 3/09/2010 event, pulse-like feature most likely caused by soft soil site-effects. (b) Lyttelton Port Company record from the Christchurch (New Zealand) 21/02/2011 event, impulsive characteristics possibly due to hanging-wall effects. (c) Lovall Valley, Loop Road record from the South Napa (California) 24/08/2014 event. Velocity pulse likely caused by forward rupture directivity. .... 61

Figure 4.2. Velocity time history of TCU068 record from the 1999 Chichi (Taiwan) earthquake and extracted pulse according to Shahi and Baker (2014) superimposed in red. The first component Daubechies wavelet pseudo-period results in pulse period determined at 12.3s. .... 62

Figure 4.3: Denali (Alaska) 3/11/2002, TAPS pump station 10 velocity time history (azimuth of horizontal component  $56^\circ$ ). .... 65

Figure 4.4: Linear regression of log-pulse period against magnitude (a) and linear correlation between pulse period ( $T_p$ ) and period of maximum PSV (or predominant period  $T_g$ ) (b)..... 66

Figure 4.5: Normalized residuals for the peak ground velocity (a) and spectral pseudo-acceleration at  $T=T_p$  (b) for pulse-like directivity ground motions. .... 67

Figure 5.1. Representation of trilinear backbone curve in normalized coordinates (ductility  $\mu$  in the abscissa and reduction factor  $R$  in the ordinate) and defining parameters: post-yield hardening slope  $\alpha_h$ , softening branch negative slope  $\alpha_c$  and capping ductility  $\mu_c$  which separates the hardening and softening branches..... 73

Figure 5.2. SPO2IDA estimates of the 16%, 50% and 84% fractile IDA curves for an oscillator with natural period of vibration  $T=1.0s$ , superimposed over the oscillator’s trilinear backbone curve. The backbone is defined by hardening post-yield slope 20% of the elastic, capping ductility at  $\mu_c = 3.0$  and a softening branch with descending slope of -200%. .... 76

Figure 5.3. Schematic representation of the “equivalent ductility”  $\mu_{eq}$  concept..... 79

Figure 5.4. Median pulse-like IDAs for a family of coincident post-capping slope oscillators with  $\mu_{eq} = 8$  and  $T/T_p = 0.40$ . Earlier arrival at capping ductility consistently leads to almost proportionately earlier arrival at capacity. .... 81

Figure 5.5. Schematic representation of the modular approach towards obtaining a model for the complete trilinear backbone: individual components of the model are developed separately and then combined. .... 83

Figure 5.6. Comparison of the fitted model of Equation (5.6) with the underlying data for SDOF systems (a) with  $\alpha_h = 3\%$  at  $T/T_p = 0.50$ , (b)  $\alpha_h = 15\%$  at  $T/T_p = 0.30$  and (c)  $\alpha_h = 50\%$  at  $T/T_p = 0.40$  ..... 87

Figure 5.7. Model fit of Equation (5.8) plotted over calculated SDOF pulse-like IDAs for oscillators with (a)  $\alpha_c = -0.20$  at  $T/T_p = 0.30$ , (b)  $\alpha_c = -0.50$  at  $T/T_p = 0.50$  and (c)  $\alpha_c = -0.90$  at  $T/T_p = 0.80$ . Note that the fitted model has been extended past the collapse capacity point only for presentation reasons..... 89

Figure 5.8. Model prediction of the fractile pulse-like IDAs for a trilinear backbone oscillator ( $\alpha_h = 0.20$ ,  $\alpha_c = -0.50$  and  $\mu_c = 6$ ) at  $T/T_p = 0.40$ . .... 91

Figure 5.9. Comparison between median pulse-like ductility demand given reduction factor  $\mu_{50\%}|R$  obtained by in Chapter 2 (see also Iervolino et al., 2012) and the present study for bilinear oscillators with (a)  $\alpha_h = 0.03$  at  $T/T_p = 0.50$ , (b)  $\alpha_h = 0.05$  at  $T/T_p = 0.70$ , (c)  $\alpha_h = 0.0$  at  $T/T_p = 0.20$  and (d)  $\alpha_h = 0.10$  at  $T/T_p = 1.00$  ..... 93

Figure 5.10. (a) Ordinary SPO2IDA median prediction for a bilinear oscillator with vibration period  $T=1.0s$ , post-yield hardening slope  $\alpha_h = 0.10$  and spectral acceleration at yield  $S_a^{yield} = 0.10g$  compared with curves incorporating pulse-like effects in both arbitrary and systematic fashion. .... 98

(b) Information obtained from site-specific NS hazard incorporated into the pulse-like IDA model to obtain site-specific IDA curves. .... 98



# Chapter 1

## Introduction

### 1.1 MOTIVATION

The present thesis confronts the problem of evaluating the seismic performance of structures in near-source conditions, when said structures are designed for inelastic response to strong ground motion. What sets near-source (NS) seismic input apart and causes it to merit particular attention, is the fact that NS ground motions often contain significant wave pulses (see for example Figure 1.1). The engineering relevance of NS pulse-like ground motions has been receiving increased attention during the past decade, since it has been recognized that such ground motions can be more damaging than ordinary ground motions and can induce a distinctive type of inelastic demand.

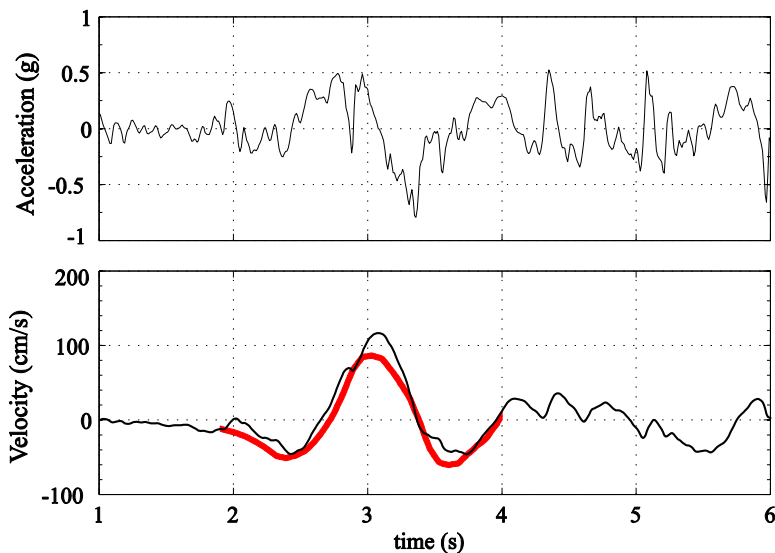


Figure 1.1. Initial segment of the acceleration and velocity time history of the fault-normal component of ground motion recorded on the left abutment of the Pacoima Dam, during the 1971 San Fernando (California) earthquake. Impulsive waveform in the velocity record (Baker, 2008) indicated in red.

The primary cause of impulsive characteristics in NS strong ground motion is rupture *forward directivity* (FD). This phenomenon, to be examined in more detail in the following, consists of most of the seismic energy from the extended fault rupture arriving at a site in a short time-interval, resulting in a single velocity pulse. The present work is concentrated on accounting for this NS effect in the assessment of structural seismic performance and, ultimately, design. The proposed methodologies seek to incorporate recent advances in near-source probabilistic seismic hazard analysis (NS-PSHA) but also entail the development of new analytical tools.

### 1.1.1 NEAR-SOURCE EFFECTS AND FORWARD DIRECTIVITY

Strong ground motion recorded at sites located in proximity to seismic faults, often bears the imprint of the rupture process, being subject to various phenomena collectively known as near-source effects.

The most important among these, from a structural engineering perspective, is forward rupture directivity. During fault rupture, shear dislocation may propagate at velocities very near to the shear wave velocity. As a result, there is a *probability* that, at sites aligned along the direction of rupture propagation, shear wave-fronts generated at different points along the fault arrive almost simultaneously, delivering most of the seismic energy in a single double-sided pulse registered early in the velocity recording (Singh, 1985, Somerville et al., 1997, Bolt, 2004). See Figure 1.2 for a schematic representation of this effect.

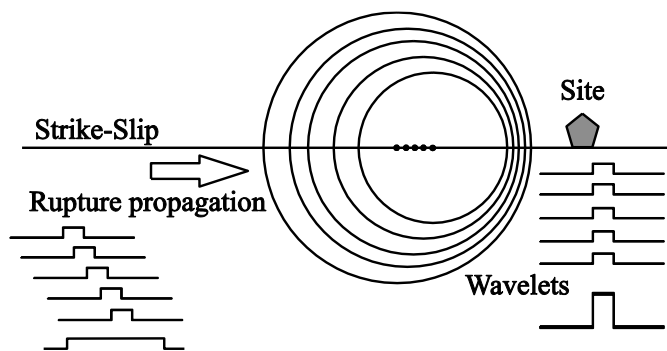


Figure 1.2. Snapshot of wave fronts; pictorial representation of the directivity of seismic energy adapted from Singh (1985).

Another frequently cited NS effect, which can also manifest itself in the form of impulsive behavior of the ground motion, is *fling-step*. Fling-step pulses occur when a site is located near a seismic source with significant surface rupture, on the ground motion component parallel to the slip direction. The fling-step velocity pulse is typically one-sided, integrating into the permanent tectonic displacement (Bolt, 2004). One such example is shown in Figure 1.3, where the velocity trace of one component of the notorious TCU068 recording from the 1999 Chichi (Taiwan) Earthquake is plotted.

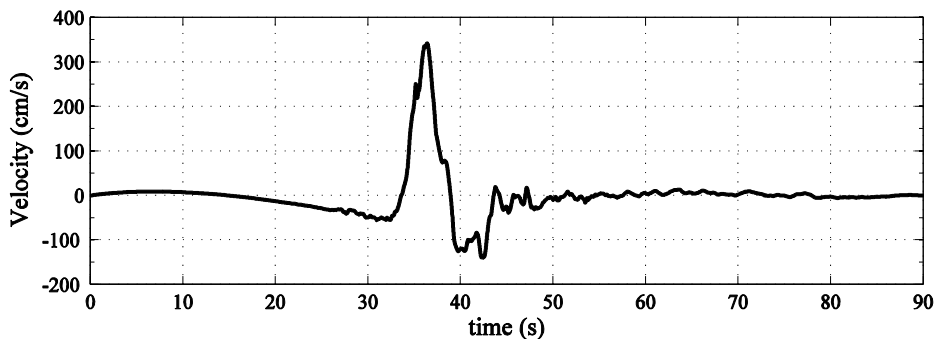


Figure 1.3. Velocity time-history of the TCU068 record from the 1999 Chichi (Taiwan) earthquake. Typical example of a fling-step pulse.

Despite the fact that this work focuses exclusively on directivity effects, fling-step pulses are nevertheless relevant. In the case of dip-slip faulting, directivity and fling-step pulses may occur on the same component (Bolt, 2004) thus becoming practically inseparable.

Finally, another effect that is sometimes mentioned in a NS context, is ground motion polarization, or *directionality* (Shahi and Baker, 2014). Although not exclusively NS in nature, directionality can nonetheless be systematically different for NS ground motions when compared to far-field records.

### 1.1.2 ENGINEERING SEISMOLOGY PERSPECTIVE ON DIRECTIVITY

The fault rupture process giving rise to earthquakes, consists of shear dislocation beginning on one point on the fault and propagating at a velocity approaching that of shear wave propagation. The effect of the rupture process on recorded ground motion, when the former is considered as a moving source of seismic waves, was

first described by Benioff (1955). The actual term *directivity* was first coined by Ben-Menahem (1961).

Directivity is sometimes cited as *analogous* to the Doppler effect in acoustics (Douglas et al., 1988). This entails a theoretical prediction of consistently increased amplitudes and heightened frequencies, for a narrow band of angles around the direction of rupture propagation (Joyner, 1991). However, even though the fundamental principle behind the Doppler effect and rupture directivity remains the same, a propagating shear dislocation is far from being a monochromatic oscillator (hence preference to the term “analogous” above).

According to Somerville et al. (1997), it is the radiation pattern of seismic energy encapsulated into horizontally polarized SH waves that can cause the aforementioned pulse of motion to occur. This is the reason for which directivity pulses are mainly expected in a direction normal to the strike of the fault. In this sense, directivity pulses can be regarded as the result of constructive interference of the seismic waves propagating towards the site.

The geometric conditions for the occurrence of forward-directivity can be met in both strike-slip and dip-slip faulting mechanisms (as alluded to during the brief discussion of fling-step). This is rather obvious in the case of strike-slip faulting, defined by a horizontal alignment of slip along the fault’s strike and rupture that also propagates horizontally along the strike, either unilaterally or bilaterally.

In normal or reverse faults, the simultaneous alignment of rupture and slip direction up the fault plane can produce rupture directivity effects at sites around its up-dip projection (or its actual surface exposure). However, it should be mentioned that in the latter case, some variability has been observed regarding the direction of motion in which directivity is identified (Howard et al., 2005).

When the rupture front propagates towards a given near-source location aligned with the fault, the conditions are met for most of the seismic energy to arrive in a single, low frequency pulse of ground motion.

This effect, known as forward-directivity. If one were to consider rupture propagation as a moving source of seismic wave emission, it would become apparent that in the case of the rupture propagating at about the same speed as the shear waves, these would ultimately arrive at sites meeting certain geometric condition almost simultaneously. Consequently, this pulse of motion will be characterized by early arrival in the recorded time-history.

From a theoretical point of view, there have also been attempts to relate the recorded characteristics of impulsive near-source ground motions to specific rupture models.

According to Aki and Richards (2002) for a Haskell-type moving dislocation with slip motion parallel to the direction of rupture propagation, the displacement near the fault has been predicted to have an impulsive form with width nearly equal to the *rise time*. Other models that can be mentioned in this context are the implementation of *isochrones* theory on S-wave emission and the specific-barrier model of fault rupture. Generally speaking, high isochrones velocities correspond to higher stress drops and ultimately stronger rupture directivity; this leads to forward-directivity effects being more pronounced when associated with reverse faulting as compared to strike-slip faulting. These models also predict that pulse duration should be proportional to rise time. The interested reader is referred to the works of Mavroeidis and Papageorgiou (2003) and Spudich and Chiou (2008) for further details. Finally, an important observation is that in a given event, not all sites satisfying a given set of geometric criteria will experience forward-directivity in the sense leading up to a coherent velocity pulse (Bray and Rodriguez-Marek, 2004). This introduces an additional stochastic parameter into the study of near-fault ground motions that has received due attention (Iervolino and Cornell, 2008).

### **1.1.3 DIRECTIVITY FROM AN EARTHQUAKE ENGINEERING PERSPECTIVE**

One of the first studies to make observations concerning the impulsive nature of a near-source record was made by Housner and Trifunac (1967), when these researchers were called upon to examine the record of after the 1966 Parkfield earthquake in California, which was recorded at a very small distance (~80m) from the fault rupture.

Following the 1971 San Fernando (California) earthquake, Bertero et al. (1978) went on to attribute the significant damages sustained by the Olive View Hospital to the effect of a long period fling-step pulse contained in the ground motion. This was the first time that structural damage was linked to the impulsive nature of near-fault seismic ground motion, highlighting in particular the susceptibility of flexible structures to the long-period pulses and their prodigious energy content. The same event also provided an early example of forward rupture directivity, detected in the record obtained at the left abutment of the Pacoima Dam (Bolt, 2004 – also see Figure 1.1).

The 1979 Imperial Valley, 1994 Northridge (both California) and 1995 Kobe (Japan) earthquakes not only provided an adequate number of NS records but also first-hand evidence of their damaging potential to engineered infrastructure. Consequently, this spurred systematic investigations into NS ground motions to begin in earnest. Baez and Miranda (2000) observed increased inelastic demand of some of these ground motions, which systematically overstepped the “equal displacement rule” (Veletsos and Newmark, 1960); they linked this behavior to the particular features observed in the velocity time-history, focusing on peak-to-peak velocity (PPV). Mavroeidis and Papageorgiou (2003) investigated the mathematical representation of the impulsive portion of NS ground motions and evaluated the effect of parameters such as pulse amplitude and pulse duration – or *pulse period*  $T_p$  – on the dynamic response of simple oscillators. Alavi and Krawinkler (2004) studied the effect of NS pulse-like ground motions on multiple-degree-of-freedom (MDOF) structures and consolidated the importance of pulse period in determining structural response. Akkar et al. (2004) also affirmed the importance of pulse period in their study of single-degree-of-freedom (SDOF) systems subjected to pulse-like records.

During the past decade, research in the subject of NS directivity and pulse-like ground motions has accelerated in pace and important contributions have been made. The inclusion of directivity effects in NS-PSHA (Tothong et al., 2007) and the systematic treatment and classification of pulse-like records (Baker, 2008) deserve mention. Nevertheless, methodologies of seismic structural assessment consistent with these advances are conspicuous in their absence from modern seismic codes. The main aspiration of the present work is to contribute in filling this void.

## 1.2 ORGANIZATION OF THE THESIS

In **Chapter 2** a dataset of previously identified impulsive near-source records is used to derive an analytical-form relationship for the inelastic displacement ratio by means of regression analysis. It is found that a double-opposite-bumps form is required to match the empirical data as function of the structural period over the pulse period ratio, similar to what has been proposed in the literature for soft soil sites. The relationship consistently builds on previous studies on the topic, yet displays different shape with respect to the most common equations for static structural assessment procedures. This reveals that inelastic seismic demand of near-source pulse-like ground motions can exhibit different trends than *ordinary* records i.e., records not identified as pulse-like.

**Chapter 3** discusses the extension of non-linear static procedures for seismic design and assessment, with respect to the inelastic demand associated with forward directivity. In this context, a methodology is presented for the implementation of the Displacement Coefficient Method towards estimating near-source seismic demand. This method makes use of the results of near-source probabilistic seismic hazard analysis and a semi-empirical equation for pulse-like inelastic displacement ratio, which was derived in Chapter 2. An illustrative application of the Displacement Coefficient Method, with explicit inclusion of near-source, pulse-like effects, is given for a set of typical, plane, reinforced concrete frames, designed under Eurocode provisions. Different scenarios are considered in the application and non-linear dynamic analysis results are obtained and discussed with respect to the static procedure estimates. Conclusions drawn from the results help to assess the importance of incorporating near-source effects in performance-based seismic design.

In **Chapter 4**, additional near-source ground motions from recent seismic events, that have been recently been made available to engineers, are examined for signs of directivity and impulsive characteristics. This investigation employs both well-established as well as more recent procedures of pulse identification. Ground motions identified as pulse-like are further examined with the help of the relevant literature, in an attempt to discern those pulses most likely caused by directivity rather than other unrelated phenomena. The result is the compilation of a more extended database of near-source pulse-like ground motions, intended to take advantage of and incorporate all this newly available information in the subsequent research.

In **Chapter 5**, the seismic demand of oscillators with more complex, trilinear, backbone curves to near-source pulse-like ground motions is examined. This study is motivated by the need for seismic demand estimates by nonlinear static procedures that delve deeper into the inelastic range and arrive at quantifying dynamic collapse capacity, which has already set researchers on this path for ordinary ground motions. Thus, this chapter closely follows the methodology of Vamvatsikos and Cornell (2006), employing incremental dynamic analysis and the suite of one hundred and thirty pulse-like-identified ground motions, presented in Chapter 4, in order to develop an elaborate  $R-\mu-T/T_p$  relation for pulse-like near-source motions and oscillators characterized by generic trilinear backbones. The resulting analytical model captures both central tendency and dispersion of near-source pulse-like seismic demand. The model also makes the important inclusion of pulse period as a predictor variable, whose importance is demonstrated in an illustrative application. **Chapter 6** offers a summary of the work presented in the thesis as well as a presentation of the principal conclusions derived from said work.

**CHAPTER 1 REFERENCES**

Aki K, Richards GP. Quantitative Seismology. 2nd Edition, University Science Books, Sausalito, CA; 2002.

Akkar S, Yazgan U, Gülkan P. Deformation limits for simple non-degrading systems subjected to near-fault ground motions. Proc 13th World Conf Earthq Eng 2004; Vancouver BC, Canada, Paper no. 2276.

Alavi B, Krawinkler H. Behavior of moment-resisting frame structures subjected to near-fault ground motions. Earthquake Engng Struct Dyn 2004; 33(6): 687–706.

Baez JI, Miranda E. Amplification factors to estimate inelastic displacement demands for the design of structures in the nearfield. Proc., 12th World Conf. on Earthquake Engineering, 2000; Auckland, New Zealand.

Baker JW. Identification of near-fault velocity and prediction of resulting response spectra. Proc Geotech Earthq Eng and Struct Dyn IV 2008; Sacramento, CA.

Benioff H. Mechanism and strain characteristics of the White Wolf fault as indicated by the aftershock sequence. In: Earthquakes in Kern County California during 1955, ed. Oakeshott GB, California Division of Mines Bulletin 1955; 171: 199-202.

Ben-Menahem A. Radiation of seismic surface waves from finite moving sources. Bulletin of the Seismological Society of America 1961; 51: 401-435.

Bertero VV, Mahin SA, Herrera RA. Aseismic design implications of near-fault San Fernando earthquake records. Earthquake Engineering and Structural Dynamics 1978; 6:31–42.

Bolt B. Engineering Seismology, In: Earthquake Engineering: From Engineering Seismology to Performance-Based Engineering, eds. Bozorgnia Y, Bertero VV, CRC Press, FL, 2004.

Bray JD, Rodriguez-Marek A. Characterization of forward directivity ground motions in the near-fault region. Soil Dynamics and Earthquake Engineering 2004; 24(11):815–828.

Douglas A, Hudson JA, Pearce RG. Directivity and the Doppler Effect. Bulletin of the Seismological Society of America 1988; 78(3): 1367-1372.

Housner GW, Trifunac MD. Analysis of accelerograms: Parkfield earthquake. *Bulletin of the Seismological Society of America* 1967; 57: 1193–1220.

Howard JK, Tracy CA, Burns RG. Comparing observed and predicted directivity in near-source ground motion. *Earthq Spectra* 2005; 21(4): 1063–1092.

Iervolino I, Cornell CA. Probability of occurrence of velocity pulses in near-source ground motions. *B Seismol Soc Am* 2008; 98(5): 2262–2277.

Joyner WB. Directivity for Nonuniform Ruptures. *Bulletin of the Seismological Society of America* 1991; 81(4): 1391-1395.

Mavroeidis GP, Papageorgiou AS. A Mathematical Representation of Near-Fault Ground Motions. *Bulletin of the Seismological Society of America* 2003; 93(3): 1099–1131.

Shahi SK, Baker JW. NGA-West2 Models for Ground Motion Directionality. *Earthquake Spectra* 2014; (30)3:1285-1300.

Singh PJ. Earthquake Ground Motions: Implications for Designing Structures and Reconciling Structural Damage. *Earthquake Spectra* 1985; 1(2):239–270.

Somerville PG, Smith NF, Graves RW, Abrahamson NA. Modification of empirical strong ground motion attenuation relations to include the amplitude and duration effects of rupture directivity. *Seismol Res Lett* 1997; 68: 199-222.

Spudich P, Chiou BSJ. Directivity in NGA Earthquake Ground Motions: Analysis Using Isochrone Theory. *Earthquake Spectra* 2008; 24(1): 279-298.

Tothong P, Cornell CA, Baker JW. Explicit directivity-pulse inclusion in probabilistic seismic hazard analysis. *Earthq Spectra* 2007; 23: 867-891.

Vamvatsikos D, Cornell CA. Direct estimation of the seismic demand and capacity of oscillators with multi-linear static pushovers through IDA. *Earthquake Engng Struct. Dyn* 2006; 35, 1097-1117.

Veletsos AS, Newmark NM. Effect of inelastic behavior on the response of simple systems to earthquake motions. *Proc., 2nd World Conference on Earthquake Engineering, Vol. II, 1960; Tokyo, 895–912.*

## Chapter 2

# Inelastic Displacement Ratio of Near-Source Pulse-Like Ground Motions

### 2.1 INTRODUCTION

In near-source (NS) conditions, ground motions may show special characteristics, which systematically affect seismic structural demand. This is believed to be due to rupture's forward directivity, which may show up at sites in particular geometrical configurations with respect to the rupture, and results in velocity fault-normal signals characterized by a large full-cycle pulse at the beginning of the record and containing most of its energy (Somerville et al., 1997). Previous studies (such as Chioccarelli and Iervolino, 2010), found particular effects on both elastic and inelastic seismic demand characterizing pulse-like records, when compared to those non pulse-like (hereafter *ordinary*).

The features of NS pulse-like records which may be of structural interest are:

1. Ground motion is characterized by fault normal (FN) rotated record of generally larger amplitude than the fault parallel (FP), while non-pulse-like ground motions have *equivalent* FN and FP components.
2. FN pulse-like signals are characterized by a non-standard pseudo-acceleration spectral shape with an increment of spectral ordinates in a range around the pulse period ( $T_p$ ), that is, a *bump* shape.
3. Inelastic to elastic seismic spectral displacement ratio for FN pulse-like records may virtually depart from the *equal displacement* rule (Veletsos and Newmark, 1960), and can be higher than that of ordinary motions. Increments are displayed in a range of period between about 30% and 50% of pulse period.

Items (1) and (2) refer to elastic seismic demand, and call for investigations about the need and feasibility to account for them in probabilistic seismic hazard analysis. Such studies are currently in progress; e.g., Tothong et al. (2007), Shahi and Baker

(2011), Chioccarelli and Iervolino (2013). Item (3) refers to inelastic demand, and is the subject of this chapter, in which the inelastic to elastic displacement ratio, or  $C_R$ , is studied by means of semi-empirical relationships (e.g., Ruiz-García and Miranda, 2003). In Equation (2.1),  $S_{d,e}(T)$  is the elastic spectral displacement at period  $T$  and  $S_{d,i}(T)$  is its inelastic counterpart for a given strength reduction factor (usually indicated as  $R$  or  $R_s$ ).

$$C_R = S_{d,i}(T)/S_{d,e}(T) \quad (2.1)$$

Current static structural assessment procedures (e.g., Fajfar, 1999) rely on prediction equations for this (or similar) parameters, in order to estimate inelastic seismic demand given the (elastic) seismic hazard. Because such relationships have to be estimated semi-empirically, in those cases where peculiar features in ground motions are expected, it is necessary to investigate whether they may exhibit special trends (e.g., Ruiz-García and Miranda, 2006). In fact, inelastic displacement for near-source conditions was studied already by a number of researchers such as Baez and Miranda (2000) and Akkar et al. (2004). The most up to date study with respect to this issue actually dealing with pulse-like records is that of Ruiz-García (2011), which also motivates this study by pointing out the need for further investigation on the  $C_R$  functional form. This is the scope of the study presented herein, where a series of bilinear (with 3% post-elastic stiffness) single-degree-of-freedom (SDoF) systems were analyzed when subjected to:

- (i) sets of FN impulsive records.
- (ii) the corresponding FP components.
- (iii) a set of ordinary ground motions.

The SDoF systems were designed to cover different nonlinearity levels, measured by means of  $R$ . The latter is given in Equation (2.2), where:  $F_e$  is the maximum elastic force induced by the ground motion on an infinitely elastic SDOF structure,  $S_{a,e}(T)$  is the elastic spectral acceleration,  $m$  is the mass of the SDoF system, and  $F_y$  is the yielding strength in the case of bilinear hysteresis' backbone (yielding strength was changed record by record to have uniform strength reduction factor, that is, a constant  $R$  approach). Results were employed to fit the observed trends, which were found to be different if compared to those of ordinary and FP records (at least in terms of amplitude in this latter case), as a function of the  $T$  over  $T_p$  ratio.

$$R = F_e/F_y = S_{a,e}(T) \cdot m/F_y \quad R = \{2, 3, \dots, 8\} \quad (2.2)$$

In the following, dataset and empirical trends are briefly described first, then the discussion of chosen functional form is given, along with a description of the

regression strategy. Finally, results are presented and discussed with respect to background research.

## 2.2 DATASET AND EMPIRICAL EVIDENCE

Pulse-like records considered are a set, from Chioccarelli and Iervolino (2010), identified with the algorithm of Baker (2007), which is extremely useful as it allows to remove most of the subjectivity in the analysis of directivity in ground motion (which comes in the usual approach of visual inspection of waveforms) and to search large datasets, enabling comparisons with the ordinary case.

The procedure of Baker (2008) is based on wavelets to extract the pulse at the beginning of a record and to determine its  $T_p$ . It also provides a score, a real number between 0 and 1, which is function of the energy and amplitude of the pulse with respect to the recorded ground motion. In fact, the dataset considered herein is comprised of impulsive FN components from the NGA database (<http://peer.berkeley.edu/nga/>) within 30 km from the source and with pulse score equal or larger than 0.85. This is the dataset also employed by Iervolino and Cornell (2008), to which L'Aquila records analyzed in Chioccarelli and Iervolino (2010) plus the recording of the same event by AQU station of the Mediterranean Network (MedNet, <http://mednet.rm.ingv.it/>) which was not yet available at the time, were added.

For comparison, also records identified as non-pulse-like (i.e., ordinary) according to the discussed procedure, yet within 30 km from the source, were considered. In Table 2.1 these datasets are summarized, in terms of number of earthquake events and records. Table.2 reports about distribution of pulse-like records in  $T_p$  bins. Moment magnitude ranges from 5.2 to 7.9 and the vast majority of records was from C and D NEHRP site classification.

Table 2.1. Pulse-like and ordinary datasets.

Mechanism	Earthquakes	Records	Earthquakes with Pulse-Like Records	Pulse-Like Records
Strike-Slip	22	133	12	34
Non-Strike-Slip	23	242	12	47
Total	45	375	24	81

Table 2.2. Distribution of pulse-like records in  $T_p$  bins.

$T_p$	[0s, 1s[	[1s, 2s[	[2s, 3s[	[3s, 4s[	[4s, 5s[	[5s, 6s[	[6s, 12s[
Number of records	22	20	8	11	10	5	5

The number of records from strike-slip events is 133, the records identified as pulses in the given dataset are 34. Records from other faulting mechanisms are in a unique category due to their relative paucity summing up to 375, 81 of which are identified as containing pulses. Note that in the following no distinction of ground motion with different source parameters is considered, as results in Chiocarelli and Iervolino (2010) do not support it. This is also because, consistent with existing literature on the topic (e.g., Ruiz-García, 2011), the period (i.e.,  $T_p$ ) is expected to be the most important characteristic of this kind of ground motions.

In Figure a FN elastic spectra, normalized to peak ground acceleration (PGA), are given for pulse-like records considered herein with  $T_p$  between 1s and 2s (*Average Pulse*) and for ordinary ground motions (*Average Non Pulse*). In Figure 2.1(b),  $C_R$  for R equal to 4 is also given for pulse-like and non-pulse-like records (*Pulse - FN* and *Non Pulse - FN*, respectively). For comparison, also  $C_R$  for the FP components of the pulse-like FN records (which not necessarily are pulse-like, even if indicated as *Pulse - FP*), are shown. The figures allow to appreciate systematic differences summarized in the introductory section, especially points (2) and (3), among the considered classes (the algorithm of Baker, 2008, assigns a  $T_p$  also to ordinary records, rendering a representation in terms of  $T/T_p$  feasible). Moreover it appears that FP records have a shape similar to FN in the low  $T/T_p$  range, yet with lower amplitudes. Same results hold for other R-values not shown.

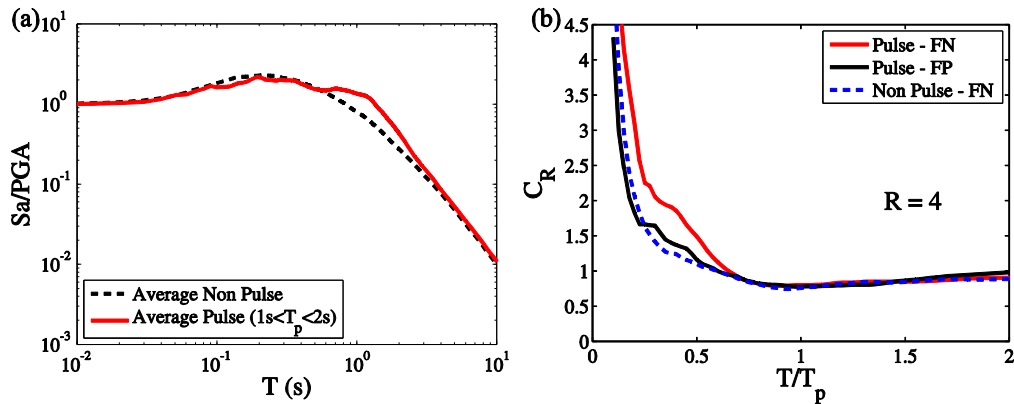


Figure 2.1. (a) Elastic 5% damped spectra for FN pulse-like with  $1s < T_p < 2s$  and ordinary records; (b) empirical  $C_R$  for FN pulse-like records, for their FP components, and for ordinary records, at  $R =$

4.

### 2.3 FUNCTIONAL FORM AND REGRESSION STRATEGY

In FEMA 440 (2005), the inelastic to elastic spectral response displacement coefficient,  $C_1$  (referred to therein as the maximum displacement ratio), is given by the relationship in Equation (2.3), where  $\alpha$  accounts for site subsoil conditions.

$$C_1 = 1 + (R - 1) / (\alpha \cdot T^2) \quad (2.3)$$

As mentioned, among other researches who have looked to near-source spectral amplification, the attention is focused herein on the work of Ruiz-Garcia (2011), who, based on empirical evidence, proposed a functional form of  $C_R$  of the type in Equation (2.4) to account for a dominant frequency in ground motion.

$$C_R = 1 + \theta_1 \cdot (T_g/T)^2 \cdot (R - 1) + \theta_2 \cdot (T_g/T) \cdot \exp\left\{\theta_3 \cdot \left[\ln(T/T_g - 0.08)\right]^2\right\} \quad (2.4)$$

In this equation the first two terms are (intentionally) similar to Equation (2.3) and the third term is a function akin to a upside-down asymmetric bell (similar to a lognormal probability density function) centered at  $T/T_g \approx 1.0$ , where  $T_g$  is the predominant period of ground motion, that is, the one corresponding to the peak of the 5% damped velocity spectrum. Although coefficient  $\theta_1$  appears in the same position as the  $\alpha$  of Equation (2.3), it is not calibrated for local soil conditions. Because of the strong correlation exists between the two period measures,  $T_p$  and  $T_g$  (see Ruiz-Garcia, 2011 and also Chapter 4 of the present work), in the following  $T/T_p$  will be used in place of  $T/T_g$ .

It was noted by Ruiz-Garcia (2011) and confirmed in the following, that Equation (2.4) is able to capture the shape of inelastic to elastic displacement ratio at  $T/T_p \approx 1$ , while it is not able to capture the bump in the low  $T/T_p$  range. This calls for a modification of the prediction equation for  $C_R$ , which is investigated herein. Equation (2.5) consists of adding another term, like the last one in Equation (2.4), to reflect the  $C_R$  trend in the low  $T/T_p$  range ( $R$  dependency in the argument of last term is explained in the following section). The resulting relationship has another bump (shifted and representing a peak rather than a valley). This equation has the same analytical form of that proposed by Ruiz-Garcia and Miranda (2006) for  $C_R$  in the case of soft soil sites. In fact, in that case, the SDoF response also is dominated by specific frequencies of ground motion, yet of different nature.

$$C_R = 1 + \theta_1 \cdot (T_p/T)^2 \cdot (R-1) + \theta_2 \cdot (T_p/T) \cdot \exp\left\{\theta_3 \cdot \left[\ln(T/T_p - 0.08)\right]^2\right\} + \theta_4 \cdot (T_p/T) \cdot \exp\left\{\theta_5 \cdot \left[\ln(T/T_p + 0.5 + 0.02 \cdot R)\right]^2\right\} \quad (2.5)$$

To determine the coefficients of Equation (2.5) for each of the  $R$ -values considered, nonlinear-segmented regressions were applied for  $0.1 \leq T/T_p \leq 2$ . The Levenberg–Marquardt algorithm (see Bates and Watts, 1988) as implemented in MATLAB<sup>®</sup> software, was employed for non-linear least-squares optimization. Moreover, the fitting was performed in two steps, such that the first three terms of Equation (2.5) were determined in the initial phase, then the residuals were computed and fitted via the fourth term; this was also to compare with Equation (2.4), and to determine efficiency of the considered functional form.

## 2.4 RESULTS AND DISCUSSION

This initial phase of the two-step procedure was to get coefficients for Equation (2.4), that is, first three terms of Equation (2.5), Table 2.3, for the bilinear SDoF systems herein investigated. This was carried out not considering data within the  $]0.35, 0.775[ T/T_p$  range. In fact, it fitted those segments of the forward-directivity data that seem to be captured by a relationship of the type in Equation (2.4); Figure 2.2(a).

Table 2.3. Coefficient estimates for Equation (2.4).

	R = 2	R = 3	R = 4	R = 5	R = 6	R = 7	R = 8
$\theta_1$	0.0151	0.0209	0.0211	0.0198	0.0184	0.0170	0.0157
$\theta_2$	-0.146	-0.230	-0.293	-0.343	-0.384	-0.417	-0.445
$\theta_3$	-2.878	-2.360	-2.375	-2.437	-2.444	-2.441	-2.434

The second step was to derive the residuals ( $\varepsilon_{C_R}$ ) of actual data with respect to Equation (2.4) and to fit them by the term in Equation (2.6), in which  $\overline{C_R}$  is the data average, and  $\hat{C}_R$  is the estimate from the model. This is similar to what was done by Baker (2008) to fit pulse-like ground motion elastic residuals to modify ordinary ground motion prediction equations. Table 2.4 reports the resulting coefficients.

$$\varepsilon_{C_R} = \overline{C_R} - \hat{C}_R \approx \theta_4 \cdot (T_p/T) \cdot \exp \left\{ \theta_5 \cdot \left[ \ln \left( T/T_p + 0.50 + 0.02 \cdot R \right)^2 \right] \right\} \quad (2.6)$$

Table 2.4. Coefficient estimates for Equation (2.6).

	R = 2	R = 3	R = 4	R = 5	R = 6	R = 7	R = 8
$\theta_4$	0.066	0.146	0.193	0.217	0.224	0.232	0.242
$\theta_5$	-47.931	-40.966	-32.697	-27.173	-20.973	-17.211	-15.177

Based on Figure 2.2(b) it should be noted that the amplification observed in pulse-like records when compared to ordinary ground motions, is around a  $T/T_p$  value whose location is a function of  $R$ . To capture this effect the linear term  $(0.50+0.02 \cdot R)$  appears in Equation (2.5) and Equation (2.6). For the sake of completeness it should be mentioned that the data, in the  $T/T_p$  range below 0.2, show another source of residual, for which Equation (2.5) does not attempt to account (in fact, it is not shown in Figure 2.2b which is plotted for  $T/T_p > 0.2$ ). This residual stemming from increased variance in the data due to the effect of low-period oscillators, has negligible effects on final fitting (i.e., Figure 2.3b); however, it may be of interest to mention that a similar problem was treated in a different manner in Chapter 5.

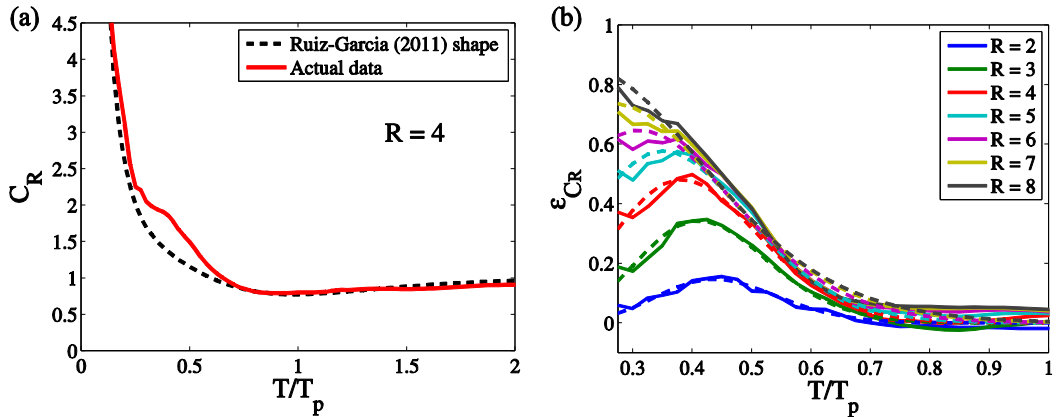


Figure 2.2. (a) Fitting of Equation (2.4) for pulse-like FN data ( $R = 4$ ) outside the  $]0.35, 0.775[$   $T/T_p$  range, and (b) fitting of Equation (2.6) for selected  $R$ -values.

Standard deviation ( $\sigma_{C_R}$ ) was also fitted as a function of  $T/T_p$  and  $R$ . In fact, functional form of the same type of Equation (2.5) was fitted on  $C_R$  plus one standard deviation data. Then, the relationship for  $\sigma_{C_R}$  the standard deviation was derived, Equation (2.7), whose coefficients are given in Table 2.5. This may be considered

the statistic of a lognormal random variable as it was found a more appropriate probability density function, rather than Gaussian, for the observed data.

$$\sigma_{C_R} = 0.1 + s_1 \cdot (T_p/T)^2 \cdot (R - 1) + s_2 \cdot (T_p/T) \cdot \exp\left\{\theta_5 \cdot \left[\ln\left(T/T_p + 0.50 + 0.02 \cdot R\right)\right]^2\right\} \quad (2.7)$$

In Figure 2.3(a) the composition of fitted coefficients of Table and Table to obtain the prediction relationship of the type in Equation (2.5), is given for all R-values investigated. As an example, actual data and fitted model are compared for R equal to four in Figure 2.3(b), in terms of average  $C_R$  and  $C_R$  plus one standard deviation. Goodness of fit holds for other R-values not shown.

Table 2.5. Standard deviation coefficients for Equation (2.7).

	R = 2	R = 3	R = 4	R = 5	R = 6	R = 7	R = 8
$s_1$	0.0170	0.0278	0.0306	0.0294	0.0262	0.0232	0.0208
$s_2$	0.0635	0.0837	0.0657	0.0516	0.0516	0.0485	0.0400

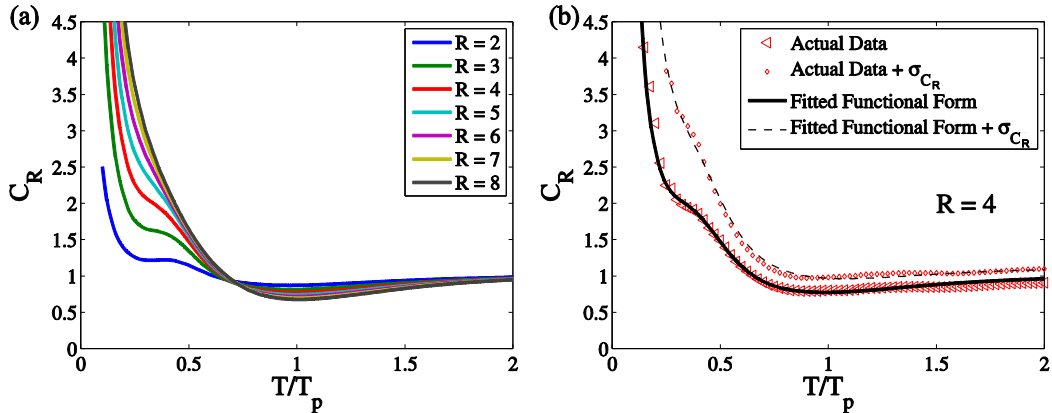


Figure 2.3. (a) Double-bump fitted  $C_R$  trends; (b) comparison with empirical data for  $R = 4$ .

## 2.5 CONCLUSIONS

In the presented study the functional form for prediction of near-source pulse-like inelastic displacement ratio, was investigated. This is required for structural assessment procedures in near-source conditions, and complements current efforts to model effects of forward directivity on elastic seismic structural demand, that is, seismic hazard.

It was found that an additional term is necessary with respect to those used to fit trends from ordinary ground motion as a function of  $T/T_p$ . An asymmetric-bell term,

centered at different points depending on  $R$ , was suitable to fit  $C_R$  in the low  $T/T_p$  range. This resulted in two opposite bumps in two different spectral regions, and builds up consistent with recent literature on the same topic and on what observed for soft soil site records, which are also characterized by a predominant period.

Coefficients for this relationship were determined in a two-step nonlinear regression, for a range of strength reduction factors, of a relatively large set of fault normal pulse-like records. Finally, standard deviation of residual data was also fitted by an analytical equation as a function of the  $T/T_p$  ratio. These results may be of some help in investigations concerning design procedures specific for near-source conditions, given that the pulse period is available from design scenarios based on near-source probabilistic seismic hazard analysis.

## CHAPTER 2 REFERENCES

Akkar SD, Yazgan U, Gulkan P. Deformation limits for simple non-degrading systems subjected to near-fault ground motions. *Proc. of the Thirteen World Conference on Earthquake Engineering*, Vancouver, CAN, 2004; paper no. 2276.

Baez JI, Miranda E. Amplification factors to estimate inelastic displacement demands for the design of structures in the near field. *Proc. of the Twelfth World Conference on Earthquake Engineering*, Auckland, NZ, 2000; paper no. 1561.

Baker JW. Quantitative classification of near-fault ground motions using wavelet analysis. *Bull. Seism. Soc. Am.* 2007; **97**(5):1486-1501.

Baker, JW. Identification of near-fault velocity and prediction of resulting response spectra. *Proceeding of Geotechnical Earthquake Engn. Struct. Dyn. IV* 2008; Sacramento, CA.

Bates DM, Watts DG. Nonlinear regression analysis and its applications. Wiley: New York, 1988.

Chioccarelli E, Iervolino I. Near-source seismic demand and pulse-like records: a discussion for L'Aquila earthquake. *Earthq. Engn. Struct. Dyn.* 2010; **39**(9):1039–1062.

Chioccarelli E, Iervolino I. Near-source seismic hazard and design scenarios. *Earthquake Engng & Struct Dyn* 2013; **42**: 603-622.

Fajfar P. Capacity spectrum method based on inelastic demand spectra. *Earthq. Engn. Struct. Dyn.* 1999; **28**(9):979-993.

Federal Emergency Management Agency. *Improvement of nonlinear static seismic analysis procedures*. Report FEMA 440. Washington DC, US, 2005.

Iervolino I, Cornell CA. Probability of occurrence of velocity pulses in near-source ground motions. *Bull. Seism. Soc. Am.* 2008; **98**(5):2262–2277.

Ruiz-García J. Inelastic displacement ratios for seismic assessment of structures subjected to forward-directivity near-fault ground motions. *Journal of Earthquake Engineering* 2011; **15**(3):449–468.

Ruiz-García J, Miranda E. Inelastic displacement ratios for evaluation of existing structures. *Earthq. Engn. Struct. Dyn.* 2003; **32**(8):1237-125.

Ruiz-García J, Miranda E. Inelastic displacement ratios for evaluation of structures built on soft soil sites. *Earthq. Engn. Struct. Dyn.* 2006; **35**(6):679-694.

Shahi S, Baker JW. An empirically calibrated framework for including the effects of near-fault directivity in probabilistic seismic hazard analysis. *Bull. Seism. Soc. Am.* 2011; **101**(2):742-755.

Somerville PG, Smith NF, Graves RW, Abrahamson NA. Modification of empirical strong motion attenuation relations to include the amplitude and duration effect of rupture directivity. *Seism. Res. Lett.* 1997; **68**(1):199-222.

Tothong P, Cornell CA, Baker JW. Explicit directivity-pulse inclusion in probabilistic seismic hazard analysis. *Earthquake Spectra* 2007; **23**(4):867-891.

Veletsos AS, Newmark NM. Effect of inelastic behavior on the response of simple systems to earthquake motions. *Proc., 2nd World Conference on Earthquake Engineering*, Vol. II, 1960; Tokyo, 895-912.



## Chapter 3

# The Displacement Coefficient Method in Near-Source Conditions

### 3.1 INTRODUCTION

Sites located in proximity to seismic faults are prone to phenomena collectively known as near-source (NS) effects. The most important among these, from a structural engineering perspective, is forward rupture directivity (FD). During fault rupture, shear dislocation may propagate at velocities similar to the shear wave velocity; as a result, there is a probability that, at sites aligned along the direction of rupture propagation, shear wave-fronts generated at different points along the fault arrive at the same time, delivering most of the seismic energy in a single double-sided pulse registered early in the velocity recording. Such impulsive behavior, which is actually the result of constructive interference of horizontally polarized waves, is most prominent in the fault-normal component of ground motion (Somerville et al., 1997). These pulses have an appreciable effect on spectral pseudo-acceleration ( $S_a$ ) (Baker, 2008).

Recent advances in probabilistic seismic hazard analysis (PSHA), expressed in terms of rate of exceedance of ground motion intensity measures (IMs), allow FD effects to be accounted for during hazard calculations (Tothong et al., 2007, Iervolino and Cornell, 2008). On the other hand, inelastic structural response to pulse-like ground motions may be systematically different from that to non-impulsive, or *ordinary*, records. Previous investigations have shown that impulsive FD records may exhibit unexpected inelastic displacement demand at periods of elastic vibration equal to some fraction of the pulse period,  $T_p$ , or other ground motion parameters (e.g., predominant period) (Ruiz-García, 2011, Iervolino et al., 2012, Akkar et al., 2004). These issues motivate the investigation of FD effects on current structural design procedures. The objective of the present study is to address the importance of extending the applicability of a non-linear static procedure of structural analysis, namely the displacement coefficient method (DCM), to cases where the structure is found under NS conditions. Recent research results about estimation of elastic and

inelastic near-source seismic demand are combined in order to develop the methodology.

The remainder of this chapter is structured so that an introductory presentation of key concepts associated with the DCM is given first. Then, the evaluation of NS elastic and inelastic seismic demand, the former corresponding to seismic hazard analysis, is briefly outlined. At this point, specific NS design scenarios, deemed meaningful for the following investigations, are presented. Subsequently, implementation of the DCM in NS conditions is illustrated by means of example applications. Results are discussed with respect to the case in which FD effects are not explicitly accounted for, and also with respect to the different site-to-source geometric configurations and the source seismicity models considered. Sets of design ground motions representative of some of these NS scenarios are assembled, and non-linear dynamic analysis results are obtained and discussed against DCM-estimated inelastic demand. Finally, conclusions regarding performance based seismic design in NS environments are presented.

### **3.2 THE DISPLACEMENT COEFFICIENT METHOD**

Performance-based seismic design of new structures – or assessment of existing ones – requires that the engineer be able to obtain estimates of structural response well into the inelastic range. Traditional methods based on linear-elastic analysis may be inadequate, while fully non-linear dynamic analysis can present the engineer with a task of daunting effort demand. The development of approximate procedures, based on static non-linear analysis of structures, thus emerged as a compromise, offering relative simplicity, while still explicitly treading beyond the elastic limit.

The key concept underlying static non-linear analysis procedures is to represent the structure by a substitute yielding single degree of freedom (SDOF) system and to subsequently use the inelastic spectral response of this system (for given elastic demand at each performance level) as a proxy for the inelastic demand of the original structure. Typically, a *capacity* or *pushover* force versus displacement curve is derived starting from a non-linear model of the structure. This curve is then approximated by a simpler (typically bilinear) relation, which is in turn used to derive the characteristics of the substitute (or equivalent) yielding SDOF system representing the structure. It is well known that this representation has limitations, depending primarily on the structure of interest. The interested reader is referred to Krawinkler and Seneviratna (1998) for a more thorough discussion.

The transition from elastic demand (e.g., determined by seismic hazard) to inelastic displacement at the SDOF level, is generally achieved by employing inelastic response spectra (Miranda, 2001). The required inelastic spectra are traditionally derived via semi-empirical models based on the response of yielding SDOF oscillators subjected to a sample of recorded ground motions. These can be presented in the form of constant-strength ( $C_R$ ) or constant-ductility inelastic displacement ratios.

As far as the DCM in particular is concerned, the conceptual foundations were developed by Seneviratna and Krawinkler (1997). It was widely introduced to engineers with its adoption by the publications on seismic rehabilitation by FEMA (1997, 2000). Improvements to the method were subsequently suggested in FEMA 440 (2005) and are also considered here. The DCM attempts to estimate the inelastic displacement demand of the structure, which corresponds to a reference degree of freedom and is termed the target displacement,  $\delta_t$ , by applying a succession of modification factors upon the elastic spectral response of the *corresponding* infinite-strength linear SDOF system, Equation (3.1).

$$\delta_t = C_0 \cdot C_1 \cdot C_2 \cdot C_3 \cdot S_a \cdot \frac{T^2}{4\pi^2} \quad (3.1)$$

In Equation (3.1),  $S_a$  is chosen to represent elastic demand and forms the basis for design. It is derived from seismic hazard provided in the form of a pseudo-acceleration design spectrum corresponding to the performance level considered. Thus,  $S_a \cdot (T^2/4\pi^2)$  represents elastic spectral displacement,  $S_{d,e}$ , of the corresponding SDOF system having a period of natural vibration equal to  $T$ . Coefficients  $C_0, C_1, C_2, C_3$  are intended to transform this elastic SDOF response to inelastic structural response.

More specifically,  $C_0$  converts the displacement of the equivalent SDOF system into that of the original multiple degree of freedom (MDOF) structure and is given by Equation (3.2).

$$C_0 = \frac{\{\varphi\}^T [M] \{r\}}{\{\varphi\}^T [M] \{\varphi\}} \quad (3.2)$$

In Equation (3.2),  $[M]$  is the lumped mass matrix of the structure,  $\{r\}$  is a vector coupling foundation motion with degrees of freedom of the structure, and vector  $\{\varphi\}$

is the generalized displacement used for the SDOF approximation, normalized so that unit value corresponds to the degree of freedom the target displacement refers to (e.g., the roof displacement).  $C_0$  is the modal participation factor when  $\{\phi\}$  is an eigenvector of the system.

$C_1$  is termed the (constant strength) inelastic displacement ratio and is defined as the peak displacement response  $S_{d,inel}$  of an inelastic SDOF system divided by the displacement of the corresponding indefinitely elastic SDOF oscillator with period  $T$ ,  $S_{d,e}$ ; see also the next section.

$C_2$  is intended to account for the effect of hysteretic behavior on maximum inelastic displacement, in the case of cyclic stiffness and/or strength degradation. This implies that for the derivation of  $C_1$  non-evolutionary hysteretic relationships are used, as originally envisioned by Seneviratna and Krawinkler (1997). An alternative approach can be to evaluate inelastic displacement ratios for degrading SDOF systems directly, as was the case in Chenouda and Ayoub (2008) and also in Dimakopoulou et al. (2013) for NS-FD ground motions. In the work of Ruiz-García (2011), the effect of cyclic structural degradation on inelastic displacement ratios for pulse-like ground motions was studied but without suggestion of any relation applicable for  $C_2$  in NS conditions. Another study, by Erduran and Kunnath (2010), proposed an improved relation for  $C_2$ , having also investigated the effect of degradation on the inelastic response to pulse-like NS records. According to Akkar and Metin (2007), implementing *moderate* stiffness degradation during response history analysis (RHA) of several generic frames, led to an average increase of peak roof displacement of the order of 7%, when compared to corresponding analyses with bilinear behavior. While following one of the aforementioned approaches to also incorporate a modified coefficient  $C_2$  in this adaptation of the DCM for NS conditions appears feasible, the added complexity could hinder the objective evaluation of the resulting demand estimates. With this in mind, in the applications presented later on in this paper, exclusively modern code-conforming buildings are considered, exhibiting a beam-sway mechanism at collapse, for which it is assumed that only limited degradation occurs. Therefore,  $C_2$  coefficient is constrained to unity in what follows.

Last, coefficient  $C_3$  was aimed at accounting for increased inelastic displacements in cases where second order (or P- $\Delta$ ) effects become an important factor resulting in negative post-yield stiffness for the equivalent SDOF approximation. In FEMA 440 (2005), it was suggested that instead of a displacement modification coefficient, an

upper limit on strength reduction factor (to follow) should be considered, beyond which dynamic instability is likely to occur. Alavi and Krawinkler (2004) reported that pulse-like ground motions may be more sensitive to phenomena of dynamic instability due to P- $\Delta$  effects than non-pulse-like ground motions. However, the issue of whether or not the  $C_3$  coefficient should be maintained remains outside the scope of the present study and  $C_3$  is also taken as unity hereafter.

### 3.3 DISPLACEMENT RATIOS OF ORDINARY AND PULSE-LIKE RECORDS

In FEMA 440 (2005) it was recommended that inelastic displacement ratio  $C_1$  be estimated from Equation (3.3), depending on strength reduction factor  $R$  and a site-subsoil-dependent parameter  $\alpha$  ( $T$  is the period of vibration).

$$C_1 = C_{R|nopulse} = \begin{cases} 1 + (R - 1) / (0.04 \cdot \alpha) & T < 0.20s \\ 1 + (R - 1) / (\alpha \cdot T^2) & 0.20s \leq T < 1.00s \\ 1.00 & T \geq 1.00s \end{cases} \quad (3.3)$$

The strength reduction factor  $R$  appearing in Equation (3.3), is the reciprocal of SDOF yield strength,  $F_y$ , normalized with respect to the maximum elastic force induced by the ground motion on an infinitely elastic SDOF structure,  $F_e$ ,  $R = F_e / F_y$  (as already defined in Equation 2.2).

As already discussed in Chapter 2, inelastic displacement ratios of NS pulse-like ground motions, systematically differ, both in amplitude and shape, from those obtained for ordinary ground motions. Also, according to Ruiz-García (2011),  $C_1$  as given by Equation (3.3), is not explicitly representative of the particular spectral shape associated with impulsive records. Hence the notation  $C_{R|nopulse}$  for  $C_1$ , which indicates that Equation (3.3) is hereafter only used when ordinary (non-impulsive) ground motions are considered.

In Chapter 2 (see also Iervolino et al., 2012), Equation (3.4) was proposed for the (constant-strength) inelastic displacement ratio,  $C_{R|pulse}$ , based on a dataset of pulse-like FD ground motions identified as such in the previous works of Baker (2008) and Chioccarelli and Iervolino (2010). Using non-linear least-squares, regression estimates that were obtained for the parameters  $\theta_i$   $\{i = 1, 2, 3, 4, 5\}$  in Chapter 2 are also given here in Table 3.1, along with a plot of Equation (3.4) which is provided as Figure 3.1. As previously discussed, the most important feature of this

analytical model for  $C_{R|pulse}$ , is the use of normalized period  $T/T_p$  as a predictor variable in order to capture the spectral regions of inelastic response amplification.

$$\begin{aligned}
 C_{R|pulse} = & \frac{S_{d,inel}}{S_a \cdot \left(\frac{T^2}{4\pi^2}\right)} = 1 + \theta_1 \cdot (T_p/T)^2 \cdot (R-1) + \\
 & + \theta_2 \cdot (T_p/T) \cdot \exp\left\{\theta_3 \cdot \left[\ln\left(T/T_p - 0.08\right)\right]^2\right\} + \\
 & + \theta_4 \cdot (T_p/T) \cdot \exp\left\{\theta_5 \cdot \left[\ln\left(T/T_p + 0.5 + 0.02 \cdot R\right)\right]^2\right\}
 \end{aligned} \tag{3.4}$$

Table 3.1. Coefficient estimates for Equation (3.4).

	R = 2	R = 3	R = 4	R = 5	R = 6	R = 7	R = 8
$\theta_1$	0.0151	0.0209	0.0211	0.0198	0.0184	0.0170	0.0157
$\theta_2$	-0.146	-0.230	-0.293	-0.343	-0.384	-0.417	-0.445
$\theta_3$	-2.878	-2.360	-2.375	-2.437	-2.444	-2.441	-2.434
$\theta_4$	0.066	0.146	0.193	0.217	0.224	0.232	0.242
$\theta_5$	-47.93	-40.97	-32.70	-27.17	-20.97	-17.21	-15.18

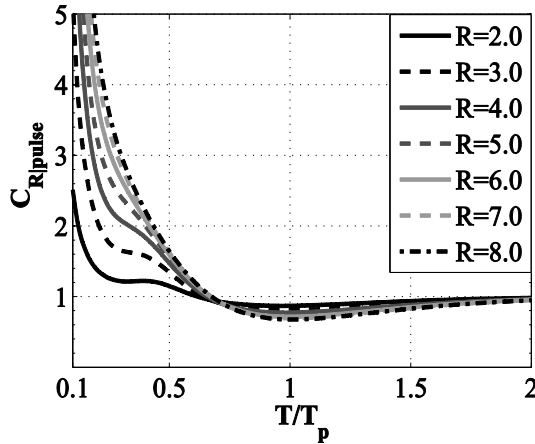


Figure 3.1: Inelastic displacement ratio of near-source pulse-like ground motions according to Iervolino et al. (2012).

### 3.4 NEAR-SOURCE HAZARD, DISAGGREGATION AND INELASTIC DEMAND

#### 3.4.1 NEAR-SOURCE PROBABILISTIC SEISMIC HAZARD ANALYSIS

Near-source probabilistic seismic hazard analysis (NS-PSHA, see Tothong et al., 2007, Iervolino and Cornell, 2008 and Chioccarelli and Iervolino, 2013) at present state computes the mean annual frequency (MAF or  $\lambda$ ) of exceedance of an IM value (spectral pseudo-acceleration at 5% damping ratio is invariably used hereafter), as the sum of two rates, one accounting for events without pulse-like characteristics in the ground motion ( $\lambda_{S_a, \text{no pulse}}$ ) and one for those with pulses ( $\lambda_{S_a, \text{pulse}}$ ), as shown in Equation (3.5).

$$\lambda_{S_a}(s_a) = \lambda_{S_a, \text{no pulse}}(s_a) + \lambda_{S_a, \text{pulse}}(s_a) \quad (3.5)$$

In the NS case, the first term on the right-hand side of Equation (3.5) is calculated by implementing some modifications to classical PSHA (e.g., Reiter, 1990), resulting in the integral shown in Equation (3.6) for a single fault case. The contribution of pulse-like ground motions to hazard is expressed by the second right-hand term of Equation (3.5), which is given in Equation (3.7).

$$\begin{aligned} \lambda_{S_a, \text{no pulse}}(s_a) &= \\ &= v \cdot \int \int_{m \underline{z}} P[\text{nopulse} | m, \underline{z}] \cdot G_{S_a | M, \underline{z}}(s_a | m, \underline{z}) \cdot f_{M, \underline{z}}(m, \underline{z}) \cdot dm \cdot d\underline{z} \end{aligned} \quad (3.5)$$

$$\begin{aligned} \lambda_{S_a, \text{pulse}}(s_a) &= \\ &v \cdot \int \int \int_{m \underline{z} t_p} P[\text{pulse} | m, \underline{z}] \cdot G_{S_a, \text{mod} | M, \underline{z}, T_p}(s_a | m, \underline{z}, t_p) \cdot f_{T_p | M, \underline{z}}(t_p | m, \underline{z}) \cdot \\ &\cdot f_{M, \underline{z}}(m, \underline{z}) \cdot dm \cdot d\underline{z} \cdot dt_p \end{aligned} \quad (3.6)$$

In these equations  $v$  is the mean annual rate of event occurrence on the source, which is assumed to follow a homogeneous Poisson process (HPP).  $M$  represents magnitude of the seismic event (not to be confused with the mass matrix appearing in Section 2 of this Chapter). A relationship between  $M$  and rupture dimensions proposed by Wells and Coppersmith (1994) is used, in order to derive the joint probability density function, or PDF,  $f_{M, \underline{z}}$ . Vector  $\underline{z}$  holds various parameters, which define rupture-site geometry and are required in order to evaluate the probability of pulse occurrence,  $P[\text{pulse} | m, \underline{z}]$  according to Iervolino and Cornell

(2008). The PDF  $f_{T_p|M,Z}$  is taken from an empirical regression model of  $T_p$  from Chioccarelli and Iervolino (2010). Finally,  $G_{S_a}$  indicates a complementary cumulative distribution function defined by an ordinary ground motion prediction equation (GMPE), while  $G_{S_a,mod}$  represents a GMPE modified to account for NS FD spectral shape in accordance with the suggestions of Baker (2008); see Chioccarelli and Iervolino (2013) for additional details on NS-PSHA.

It should be mentioned that in a recent paper by Shahi and Baker (2011), a modified GMPE was proposed for the non-impulsive case as well. This admittedly more rigorous approach, was not followed here for the sake of simplicity, taking into consideration the fact that the mean standardized residuals of ground motions whose pulse has been removed with respect to traditional GMPEs is very close to zero (Shahi and Baker, 2011). Ideally, one should use distinct GMPEs derived from regression models fitted against impulsive and ordinary records separately; however, such models are not available to date.

### 3.4.2 HAZARD DISAGGREGATION AND NEAR-SOURCE INELASTIC DEMAND

Disaggregation of NS seismic hazard can be performed once NS-PSHA results are available. Given, for example, the exceedance of an IM threshold of interest, it serves to obtain the probabilities (or probability functions) of some variables appearing in Equations (3.5-6) being causative for such an event 0 and Iervolino, 2013). In fact, hazard may be disaggregated given either the exceedance or the occurrence of a fixed level of the IM and therefore all directly obtainable results are conditional on either  $S_a(T) > s_a$  or  $S_a(T) = s_a$ .

The probability density of pulse period  $f_{T_p|S_a(T)=s_a,pulse}$  conditional on occurrence of a given design hazard threshold,  $S_a(T) = s_a$ , is relevant in the implementation of the DCM in NS conditions, as it is required in order to directly compute the expected value of  $C_R$  given the hazard level, according to Equation (3.7).

$$\begin{aligned}
 E[C_R | S_a(T) = s_a, pulse] &= \\
 &= \int_{t_p} E[C_R | S_a(T) = s_a, T_p = t_p, pulse] \cdot f_{T_p|S_a(T)=s_a,pulse}(t_p) \cdot dt_p
 \end{aligned} \tag{3.7}$$

Note that the conditional expectation  $E[C_R | S_a(T) = s_a, T_p = t_p, \text{pulse}]$  appearing in Equation (3.7) corresponds to Equations (3.4) and (2.5) herein.

Some attention should be drawn to the occurrence of the given hazard level, rather than its exceedance, as the conditioning event. One interpretation may be that even if the design elastic demand is usually determined on the basis of the exceedance probability of an IM within a time-frame at the site of interest (i.e., from the hazard curve), the subsequent structural analysis may be seen as conditional to that IM level (e.g., given the occurrence of the design spectral value). Indeed, in modern seismic code approaches, the structure is not required to be safe for the occurrence of IMs larger than that considered for design. In fact, assuming zero failure probability for IMs lower than that used for design and disregarding additional safety factors, the probability of the design IM being exceeded virtually coincides with the, implicitly accepted, risk of the structure overstepping a performance level, up to – and including – collapse.

The choice of *occurrence* of IM as a condition for disaggregation, which was made by Tothong et al. (2007) and Champion and Liel (2012), may be considered consistent with this argument, the former having been made with the objective of selecting representative records for dynamic structural analysis while the latter intended to obtain disaggregation results compatible with fragility curves. Conversely, in Baltzopoulos et al. (2013) the author of the present work and his co-authors considered  $T_p$  density conditional on exceedance of the hazard threshold, given that in most of the ordinary cases only this type of disaggregation is directly made available by seismologists (e.g., by the United States Geological Service at <https://geohazards.usgs.gov/deaggint/2008/>, last accessed November 2013).

Apart from PDFs of pulse period, another useful result can be obtained from disaggregation of NS hazard, namely, the conditional probability of pulse occurrence,  $P[\text{pulse} | S_a(T) = s_a]$ . This can be alternatively expressed as the probability that a pulse-like ground motion will be causative for the given hazard level.

Obtaining disaggregation results conditional on  $S_a(T) = s_a$  may be approximated by hazard results referring to exceedance, considering instead that  $S_a$  belongs to a small interval  $(x_1, x_2]$  around  $s_a$ . In this manner, the PDF of pulse period given that the design hazard threshold has been reached can be evaluated by Equation (3.8), while the probability of pulse occurrence is given by Equation (3.9).

$$f_{T_p|S_a=s_a,pulse} \approx \frac{f_{T_p|S_a>x_1,pulse} \cdot \lambda_{S_a,pulse}(x_1) - f_{T_p|S_a>x_2,pulse} \cdot \lambda_{S_a,pulse}(x_2)}{\lambda_{S_a,pulse}(x_1) - \lambda_{S_a,pulse}(x_2)} \quad (3.8)$$

$$P[pulse | S_a = s_a] \approx \frac{\lambda_{S_a,pulse}(x_1) - \lambda_{S_a,pulse}(x_2)}{\lambda_{S_a}(x_1) - \lambda_{S_a}(x_2)} \quad (3.9)$$

The latter probability may in turn be used to estimate NS inelastic demand  $\delta_{t-NS}$ , via the conditional expectation theorem, as an average of two separate contributions: target displacement given pulse occurrence  $\delta_{t|pulse}$  and absence thereof  $\delta_{t|no pulse}$ . These two terms are weighted by their probability of occurrence conditional to the scenario of interest, Equation (3.10).

$$\delta_{t-NS} = \delta_{t|pulse} \cdot P[pulse | S_a = s_a] + \delta_{t|no pulse} \cdot (1 - P[pulse | S_a = s_a]) \quad (3.10)$$

### 3.5 DESIGN SCENARIOS AND BUILDING MODELS

#### 3.5.1 PROBABILISTIC HAZARD WITH AND WITHOUT PULSE LIKE EFFECTS

Three design scenarios were considered to evaluate the impact of adjusting the DCM to near-source conditions. All of them refer to a hypothetical 200 km long strike-slip seismic source and two possible construction sites (Figure 3.2). Site A is aligned with the fault's strike and is located at a distance of 5 km off the tip. Site B is at 9 km from the same extremity, but in a direction normal to the fault's strike.

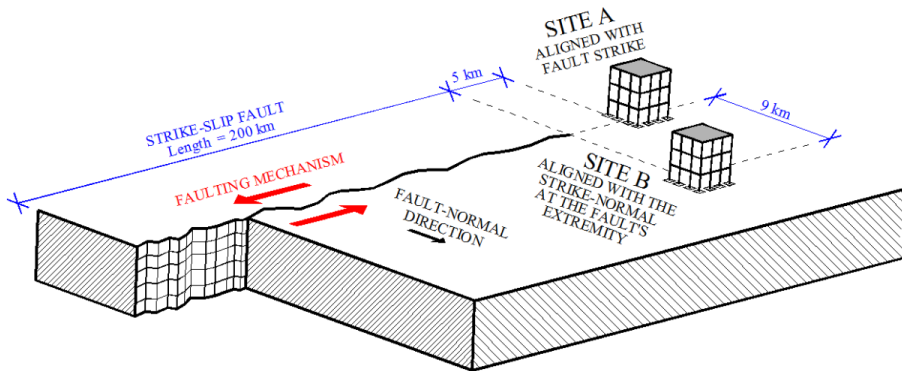


Figure 3.2. Schematic representation of site-source configuration for the design scenarios considered.

The main criterion for selecting these specific positions relative to the fault was for the two sites to exhibit the same level of design hazard (i.e., elastic spectrum ordinates) over a period range of interest ( $T = 0.50s \div 1.00s$ ), when said hazard is estimated by means of *classical* PSHA (i.e., where NS effects are not explicitly considered – Reiter, 1990) for a return period of 975 yr. This was to ensure that similar structures located at either of these sites would be designed to resist the same base shear. Thus, observed differences in terms of strength reduction factors  $R$  will be attributable to NS effects, as will be elaborated later on. In order to also exclude potential soft soil site effects, subsoil conditions at both sites were taken to correspond to stiff soil deposits with a shear wave velocity averaged over the first 30 m of terrain,  $V_{s,30}$ , equal to 400 m/s.

The first two design scenarios correspond to these two sites when seismicity on the fault is (arbitrarily) assumed to follow a Gutenberg-Richter (G-R) relationship (Gutenberg and Richter, 1944) bounded between magnitude  $M$  4.5 and  $M$  7.5, with unit negative slope and a mean annual rate of event recurrence  $\nu = 0.20$ . A third design scenario, the choice of which will be clear later on, was also considered with reference to Site A. In this case, source seismicity was assumed to correspond to a simplified characteristic earthquake (CE) model; i.e., a single magnitude  $M$  7.0 is assumed. Annual rate of earthquake recurrence for the third scenario was assumed to be 1 event/200 yr ( $\nu = 0.005$ ) which was selected on the basis that classical hazard in the  $T = 0.50s \div 1.00s$  range be approximately equal to the one resulting from the G-R model assumption. This extends the premise of shared design spectral values among all considered scenarios.

Recalling the assumption that earthquake recurrence follows a homogeneous Poisson process, uniform hazard spectra (UHS) were computed for two return periods  $T_R = 975$  yr and 2475 yr (5% and 2% probability of  $S_a(T) > s_a$  in 50 yr respectively) for all three scenarios. The UHS from classical hazard calculations are shown in Figure 3.3(a).

Regarding NS-PSHA, point A and point B were intentionally selected to correspond to site-to-source configurations both prone to FD effects, yet to a different extent; e.g., the probability that the 2475 yr return period  $S_a(T = 0.50s)$  will be exceeded due to an impulsive - rather than an ordinary - record was computed to be 76% for Site A, while for Site B the same probability was found to be 32% (assumptions underlying these calculations to follow). In all three scenarios, seismic hazard was

calculated through NS-PSHA (as outlined in Section 4). For this computation, a uniform distribution of potential epicenters along the fault was assumed.

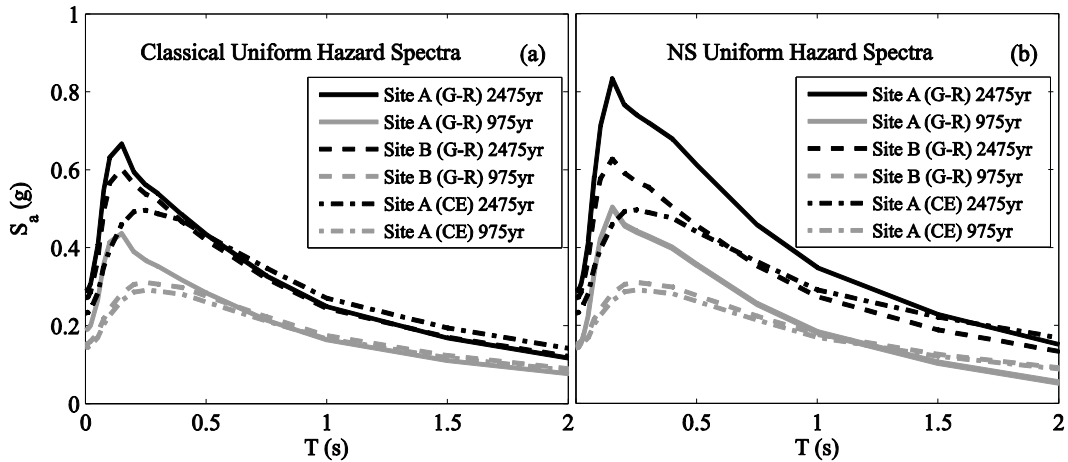


Figure 3.3. Uniform hazard spectra computed for the various design scenarios by either performing classical PSHA calculations (a) or by considering NS-FD effects in the hazard computation (b).

UHS were computed for the same two return periods of 975 and 2475 yr as in the classical hazard case above. In Figure 3.3(b), the NS spectra for the three cases are presented. Note that in the G-R scenario there is visible spectral amplification due to FD - with respect to the classical (Figure 3.3a) case - mostly affecting periods around  $T=0.50$ s. This is a consequence of  $T_p$  dependence on causal magnitude combined with the narrowband amplification scheme of Baker (2008) adopted in the NS-PSHA calculations (note that the exponential magnitude distribution of G-R seismicity leads to a preponderance of lower magnitudes in the determination of hazard at nearby sites while median  $T_p$  for M 5.0 is 0.43s). On the other hand, FD in the CE case mostly affects a range of longer spectral periods beyond those represented in the figure, which explains the proximity of the classical and NS-UHS (median  $T_p$  for M 7.0 being 3.67s).

In Table 3.2,  $S_a(T)$  values defining NS seismic hazard are reported for the three design scenarios described above, two return periods corresponding to design performance levels and three spectral periods ( $T$  equal to 0.50s, 0.75s and 1.00s), which correspond to the fundamental periods of the structures considered in the following. The lower spectral ordinates encountered at Site B in comparison with Site A are attributable to the different orientation of the two sites with respect to the

fault, which, as mentioned, makes the former less prone to FD (i.e., lower conditional pulse occurrence probability) than the latter (see Chioccarelli and Iervolino, 2014).

Table 3.2. Spectral acceleration values at periods of interest.

	$T_R=2475\text{yr}$			$T_R=975\text{yr}$			$T_R=975\text{yr}$ <i>classical</i> hazard, equal in all cases
	SITE A		SITE B	SITE A		SITE B	
	G-R	CE	G-R	G-R	CE	G-R	
$S_a(T=0.50\text{s})$	0.612 g	0.466 g	0.456 g	0.418 g	0.296 g	0.309 g	0.293 g
$S_a(T=0.75\text{s})$	0.458 g	0.382 g	0.352 g	0.294 g	0.221 g	0.229 g	0.215 g
$S_a(T=1.00\text{s})$	0.348 g	0.303 g	0.271 g	0.213 g	0.167 g	0.172 g	0.161

### 3.5.2 DISAGGREGATION RESULTS

Disaggregation of NS hazard was performed conditional on *occurrence* of  $S_a(T) = s_a$ , at the three periods of vibration in Table 3.2, and for both return periods considered. The PDFs of  $T_p$  for the 2475 yr return period are shown in Figure 3.4.

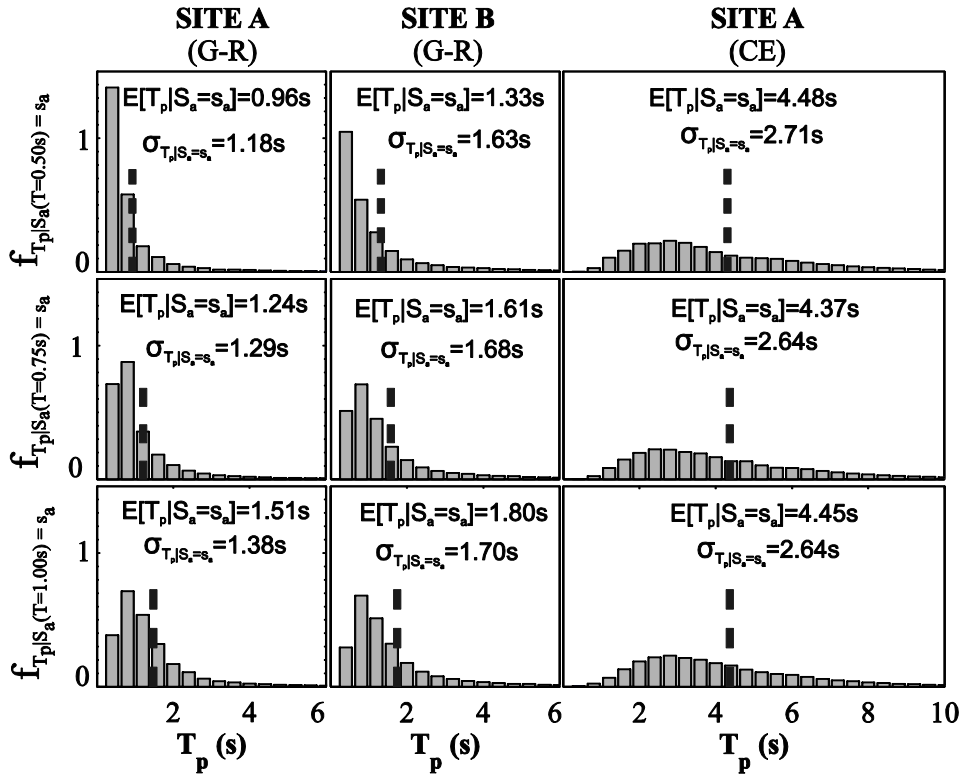


Figure 3.4. PDFs of pulse period  $T_p$ , resulting from disaggregation of NS hazard, conditional on pulse occurrence and  $S_a(T) = s_a$ , referring to 2745yr return period for each scenario (histograms normalized to unit area). Dashed lines indicate the location of the mean,  $E[T_p | S_a = s_a]$ , whose value is also shown along with standard deviation  $\sigma_{T_p | S_a = s_a}$ .

### 3.5.3 STRUCTURAL MODELS

The chosen set of structures consists of three reinforced concrete (R/C) plane frames: a 4-storey, a 5-storey, and a 6-storey frame (Figure 3.5). These frames were chosen to correspond to the internal frames of perfectly symmetric buildings without in-fills.

Furthermore, structure geometry was selected so that all frames would exhibit first-mode dominated dynamic elastic response (first mode participating mass ratios in excess of 80%), with first-mode periods of natural vibration  $T_1$  equal to 0.50s, 0.75s and 1.00s respectively, which justify the period range discussed above. The consideration of similar structures – bar first mode period – was a conscious choice, the objective being to evaluate the potentially different effects of FD at various spectral ordinates, whilst remaining within the DCM applicability domain.

All three structures were designed against gravity loads and seismic actions according to modern codes (EN-1992, EN-1998), in a manner that ensures flexure-dominated inelastic response when subjected to increasing lateral forces. More specifically, each frame was designed for inelastic response corresponding to a *behavior factor*  $\approx 4.0$  under the actions of the 975 yr return period site-specific, classical UHS (Figure 3.3a). Design values of  $S_a(T)$  are given in the last column of Table 3.2. These acceleration values are divided by the behavior factor to determine the actions under which the structures are expected to remain elastic. Material qualities assumed for design were C20/25 for concrete and S500/550 for reinforcing steel. A summary of final detailing is given in Figure 3.5.

All three frames were considered in the context of each of the three design scenarios described above, in the direction normal to the fault's strike (Figure 3.2), leading to eighteen cases because of the two return periods. Inelastic displacement demands were estimated using the DCM at two performance levels: *significant damage*, assumed to correspond to seismic action with a 5% probability of exceedance in 50 yr ( $T_R = 975$  yr), and *near collapse*, corresponding to seismic action with a 2% probability of exceedance in 50 yr ( $T_R = 2475$  yr).

Initially, pushover (base shear versus roof displacement) curves were obtained for all three structures (also shown in Figure 3.5). The non-linear structural models built for these inelastic static analyses, adopted a lumped plasticity approach, using a multi-linear moment-plastic rotation relation. The elastic stiffness of R/C members was modeled using a smeared crack approach. Moment-rotation relationships for each member were estimated using mean strength and stiffness properties for confined concrete (Mander et al., 1988) and reinforcing steel. The bilinear approximations of the resulting relations used the *collapse prevention* limiting values recommended in FEMA-356 (2000) for ultimate chord rotation capacity.

The static non-linear (pushover) analyses were carried out by applying a gradually increasing lateral force profile which remained unchanged throughout each analysis and corresponds to each structure's first mode excitation to base acceleration (first

mode eigenvectors shown in Figure 3.5). Second order (P- $\Delta$ ) effects were incorporated into the analyses on all accounts, yet collapse mechanisms were characterized by plasticization at the beam ends and the bases of ground floor columns (beam-sway mechanisms), as a consequence of conformity to capacity design rules (EN-1998) leading to positive post-yield stiffness of the equivalent SDOF systems.

### 3.6 IMPLEMENTING THE DCM IN NS CONDITIONS

Once the pushover curves were obtained, the constituent terms of the right-hand-side of Equation (3.10) had to be estimated separately. For the estimate of the elastic demand, which is needed to compute both  $\delta_{t|nopulse}$  and  $\delta_{t|pulse}$ , the NS-UHS computed for each design scenario and performance level was used (shown in Figure 3.3b, in addition to which  $S_a$  values are given in Table 3.2). Then, the non-impulsive contribution  $\delta_{t|nopulse}$  was obtained by simple implementation of the DCM in its traditional form using  $C_{R|nopulse}$  from Equation (3.3), in which subsoil coefficient  $\alpha$  was set equal to 90, corresponding to  $V_{s,30}=400$  m/s (NEHRP class C subsoil). For the estimation of the impulsive contribution  $\delta_{t|pulse}$ , Equations (3.4) and (3.7) were used to compute the mean inelastic displacement ratio for FD ground motions,  $C_{R|pulse} = E[C_R | S_a(T) = s_a, pulse]$ .

It is to recall that these target displacements, in the DCM, require a bilinear approximation of the pushover curve, which was constructed via the methodology suggested in FEMA-356 (2000). This method requires that the bilinear approximation intersect the pushover curve at the target displacement  $\delta_t$  thus resulting in some positive (in this case) post-yield stiffness. This hardening behavior is typically ignored when estimating  $C_{R|nopulse}$  via Equation (3.3). However, this matter will not be discussed at this point (see Chapter 5).

What should be mentioned is that this method of selecting the equivalent bilinear system, implies that the base shear corresponding to conventional yield,  $V_y$ , is dependent on target displacement  $\delta_t$ , thus the evaluation of both the impulsive and non-impulsive contributions requires some iteration for the estimation of strength reduction factor (see for example Baltzopoulos et al., 2013).

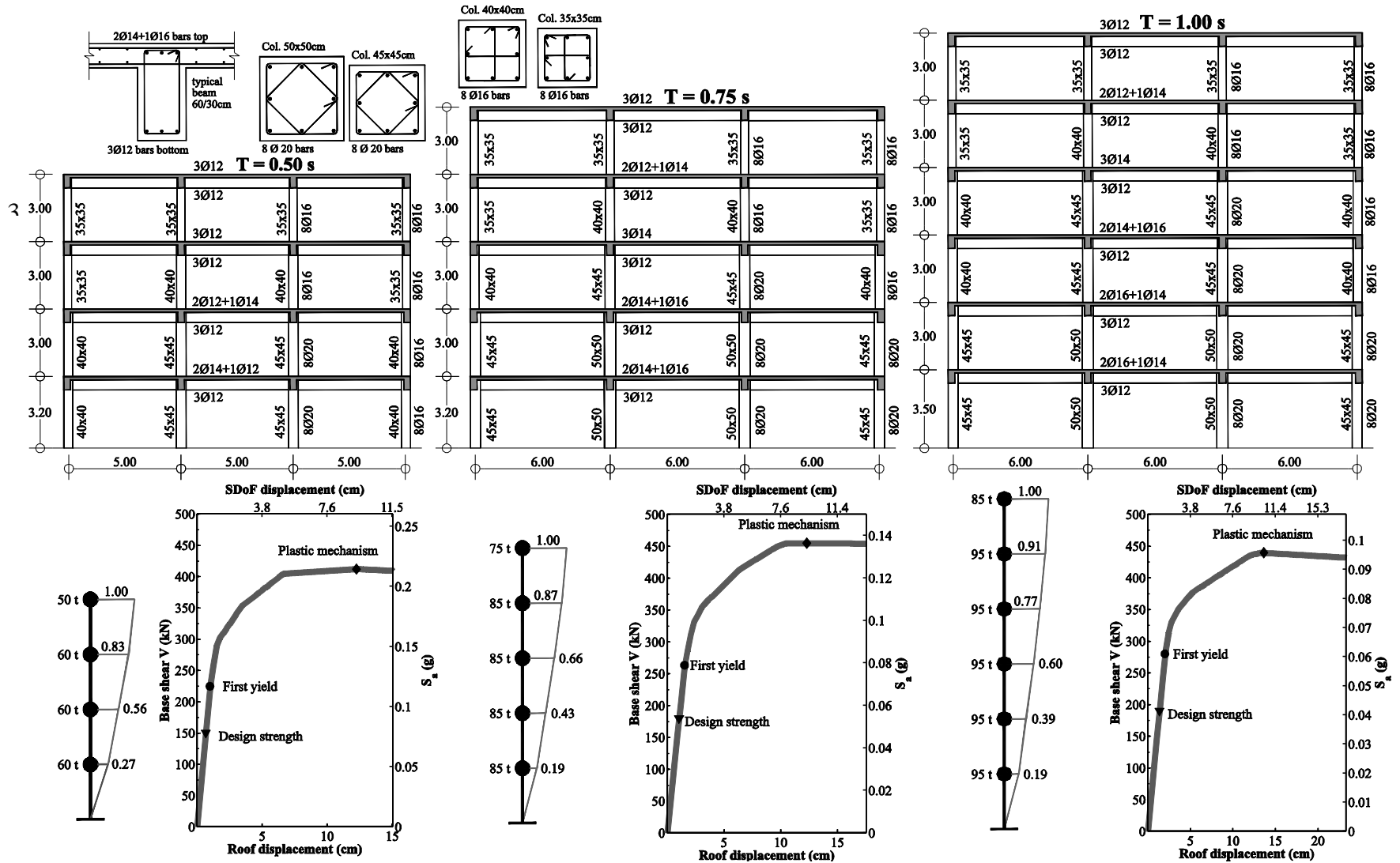


Figure 3.5. Geometry, detailing (flexural reinforcement), modal information and pushover curves for the three R/C frames used in the application.

(Page intentionally left blank)

A graphical representation (corresponding to the converged iteration) for each of the two inelastic displacement contributions considered in Equation (3.10), is given in Figure 3.6 for the 4-storey frame situated at Site A, under the assumption of G-R seismicity and for the near collapse performance level.

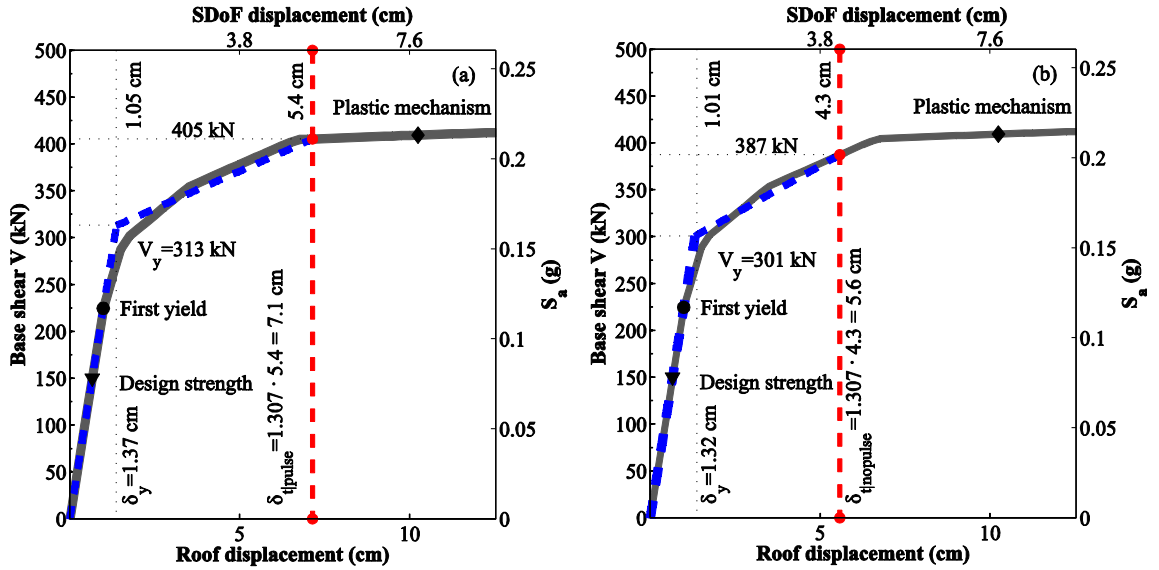


Figure 3.6. Graphical representation of application of the DCM for a 4-storey R/C frame ( $T=0.50$ s) at Site A under G-R seismicity. Target displacement estimates for near collapse performance level ( $TR=2475$  yr) considering impulsive (a) and non-impulsive (ordinary) contributions (b).

Given that, under these conditions, a 74% probability was computed for pulse occurrence conditional to the hazard threshold (i.e., from disaggregation of NS hazard), applying Equation (3.10) one obtains the result in Equation (3.11).

$$\delta_t^{NS} = \delta_{tipulse} \cdot 0.74 + \delta_{tinopulse} \cdot 0.26 = 7.1 \cdot 0.74 + 5.6 \cdot 0.26 = 6.7 \text{ cm} \quad (3.11)$$

So as to better appreciate this result, it is useful to also obtain a target displacement without explicitly accounting for FD effects, hereafter termed ordinary target displacement,  $\delta_t^{ord}$ . In order to evaluate  $\delta_t^{ord}$  one simply has to use the classical DCM (Equation 3.1) and the classical PSHA uniform hazard spectrum corresponding to each design scenario (Figure 3.3a), to represent elastic demand. For the case Equation (3.11) refers to (4-storey frame at Site A, G-R seismicity, near collapse), one obtains  $\delta_t^{ord} = 3.8$  cm, which means that accounting for FD lead to a 77% increase in target displacement. It may be worthwhile to underline that both target displacements  $\delta_{tinopulse}$  (ordinary component of NS demand) and  $\delta_t^{ord}$  (no

consideration of NS effects) are derived by applying coefficient  $C_{R|nopulse}$  (Equation 3.3), valid for ordinary ground motions, yet using different spectral values (from NS-PSHA and classical PSHA, respectively).

The results of the application of the DCM to all cases presented in the previous section are summarized in Table 3.3 to facilitate comparisons. It can be observed that the effect of FD on inelastic displacement demand was more pronounced for lower performance levels, which correspond to longer  $T_R$ .

Table 3.3. Summary of target displacement estimates resulting from application of the DCM. Two different performance levels per design scenario, per structure considered. Column  $C_{R|pulse}$  reports mean inelastic displacement ratio conditional on pulse occurrence while  $C_{R|nopulse}$  denotes mean inelastic displacement conditional on no pulse occurring.

		$T_R$	First mode period	$C_{R pulse}$	$C_{R nopulse}$	$\delta_{t pulse}$ (mm)	$\delta_{t nopulse}$ (mm)	$P[pulse S_a = s_a]$	$\delta_t^{NS}$ (mm)	$\delta_t^{ord}$ (mm)	$\frac{\delta_t^{NS} - \delta_t^{ord}}{\delta_t^{ord}}$
SITE A	Gutenberg-Richter	2475 yr	0.50	1.44	1.12	71	56	0.741	67	38	77%
			0.75	1.31	1.06	111	90	0.673	104	63	65%
			1.00	1.21	1.04	137	118	0.629	130	83	57%
	Characteristic	975 yr	0.50	1.17	1.08	40	37	0.687	39	24	63%
			0.75	1.09	1.04	60	56	0.602	58	40	46%
			1.00	1.04	1.02	72	70	0.513	71	53	34%
SITE B	Gutenberg-Richter	2475 yr	0.50	3.77	1.07	143	40	0.170	58	39	47%
			0.75	3.10	1.04	218	73	0.166	97	71	37%
			1.00	2.51	1.03	248	101	0.165	125	96	30%
	Characteristic	975 yr	0.50	3.13	1.05	75	25	0.100	30	24	25%
			0.75	2.03	1.02	83	42	0.073	45	40	12%
			1.00	1.72	1.01	94	55	0.060	57	53	8%
Gutenberg-Richter	2475 yr	0.50	1.62	1.09	60	40	0.280	46	36	27%	
		0.75	1.46	1.05	95	68	0.245	75	61	22%	
		1.00	1.28	1.03	113	91	0.243	96	81	19%	
	975 yr	0.50	1.17	1.05	29	26	0.225	27	24	11%	
		0.75	1.12	1.03	47	43	0.181	44	40	9%	
		1.00	1.06	1.02	60	57	0.150	57	53	8%	

A number of observations can also be made, by comparing the DCM estimates of inelastic displacement demand among the design scenarios considered herein. A comparison between Site A and Site B, under the working assumption that seismic hazard at both sites is dictated by the same single source following a G-R law, must necessarily focus on the fact that the position and orientation of Site A relative to the fault, is decidedly more unfavourable than that of Site B, when potential FD effects are concerned. Although this was in part expected beforehand (given existing

empirical models such as that of Iervolino and Cornell, 2008 and recent investigations of Chioccarelli and Iervolino, 2014) it is also confirmed in a most emphatic manner by the results of NS-PSHA and hazard disaggregation; probabilities of pulse occurrence given the hazard threshold computed at Site A are more than twice the ones computed for Site B and the amplification of spectral ordinates at Site A due to FD is accordingly more pronounced (Table 3.2).

Given the occurrence of hazard levels associated with near collapse performance, both sites appear most likely to be affected by pulse-like ground motions characterized by  $T_p$  between 0.50s and 1.00s, with the modal value for each case corresponding to a ratio of  $T/T_p \approx 1$ . This effect can be affirmed from the left-skewed probability densities of  $T_p$  (Figure 3.4) and can be attributed to the exponential distribution of magnitude associated with the G-R model. As a result, the realization of  $T/T_p$  ratios belonging in the range of high inelastic amplification (Ruiz-García, 2011, Iervolino et al., 2012, Akkar et al., 2004) is associated with low probability, conditional on the hazard. Thus, the difference between NS and ordinary structural response, at both sites, is primarily influenced by the elastic component, which is duly amplified by the more frequently occurring, shorter duration pulses.

A comparison, regarding FD effects, between the two different seismicity models considered at Site A comes in stark contrast with the one directly above. The CE model is associated with events of lower rate, yet greater average magnitude and consequently longer expected pulse duration, which leave the elastic spectral ordinates in the range considered largely unaffected (Figure 3.3 is particularly eloquent to this effect). Furthermore, the conditional probabilities of pulse occurrence from hazard disaggregation are lower than either of the two G-R cases; loosely speaking, the expected long-period pulses, are less likely to be responsible for reaching the hazard threshold at  $T = 0.50s \div 1.00s$  than ordinary ground motions are. However, due to the fact that the higher mean  $T_p$  corresponds to a  $T/T_p$  ratio, which translates into potentially aggressive pulse-like ground motions, expected inelastic demand is almost as large as under the G-R model scenario. In other words, the CE seismicity model, presents a case where, *for a given range of periods*, the NS elastic response spectrum hardly departs from the traditional case and yet expected inelastic demand greatly supersedes that of the classical case, resulting as a weighted average between the more frequent, benign ground motions and some rare pulse-like ground motions, which can cause larger excursions into inelasticity.

### 3.7 DCM VERSUS NON-LINEAR DYNAMIC ANALYSIS

Even though validating the results of non-linear static procedures is an open issue in earthquake engineering (e.g., Kalkan and Kunnath, 2007) and remains beyond the immediate purposes of the work presented herein, which acknowledges the DCM as an established procedure, it may be useful to ensure that dynamic RHA using recorded ground motions, consistent with the models above, provide comparable design targets. With this aim, out of the various cases addressed in the preceding sections, two were selected: the five- and six-storey frames ( $T_1=0.75s$  and  $1.00s$ , respectively) subjected to the 975 yr return period seismic hazard at site A in the M 7.0 CE scenario.

#### 3.7.1 SELECTION OF ORDINARY RECORDS

In this exercise, the pulse-like and non-pulse-like cases were treated separately with regard to the selection of real ground motions. For the non-pulse-like case (indicated above by the *nopulse* notation), a suite of 20 ordinary records was selected to match a target spectrum using the methodology proposed by Jarayam et al. (2011). Said target spectrum is a *conditional mean spectrum* (CMS), whose computation requires the average causal magnitude and Joyner-Boore distance,  $(\bar{M}, \bar{R}_{JB})$ , given absence of a directivity pulse. These values are obtainable from disaggregation of the 975 yr NS seismic hazard, at the two considered structural periods and are reported in Table 4, along with the number of standard deviations (in log-space) that separate the design value of  $S_a(T)$  from the median – a parameter known as epsilon ( $\epsilon$ ). Having obtained  $(\bar{M}, \bar{R}_{JB}, \epsilon)$ , the conditional mean spectral values at other periods and their conditional variances could be calculated, using the ground motion prediction equation of Boore and Atkinson (2008) and the correlation model of Baker and Jarayam (2008), for each of the two cases.

Table 3.4 Results from disaggregation of NS hazard (given absence of directivity pulse and occurrence of  $S_a$ ) used for the selection of the ordinary ground motion record set.

$T_1$	$S_a(T_1)$	$\bar{M}$	$\bar{R}_{JB}$	$\epsilon(S_a)$
0.75s	0.221g	7.0	48.5 km	0.865
1.00s	0.167g	7.0	52.6 km	0.897

As can be seen in Table 3.4, the values assumed by the conditioning parameters differ only slightly between the two cases, leading to similar shapes of conditional mean spectra. For this reason, a single suite of records was chosen to represent the ordinary component of seismic hazard at both periods (naturally with differing scale factor). The selected records (Table A.1) are from a subset of the NGA database (Jarayam et al., 2011) from which pulse-like ground motions were excluded and each was linearly scaled to exhibit the design  $S_a(T)$ . This ground motion selection strategy is summarized in terms of response spectra in Figure 3.7(a), where the target CMS can be seen and where each individual record has been scaled at a common  $S_a(0.75s) = 0.221g$ .

### 3.7.2 SELECTION OF PULSE-LIKE RECORDS

For the pulse-like case, a different record selection strategy had to be followed, due to the fact that  $S_a(T)$  is not a sufficient IM when pulse-like ground motions are concerned (Tothong and Cornell, 2008). For this reason, some methodologies for the selection and scaling of pulse-like records have been proposed by Baker and Cornell (2008) and Tothong and Luco (2007) based on advanced IMs; be that as it may, compatibility with current design practice and the DCM, requires that reference to the design spectrum – and therefore use of  $S_a$  as IM – be maintained.

The problem that the directivity case poses for record selection can be summarized as follows: for a specific structure with given strength, some pulse-like ground motions are particularly *aggressive*, resulting in high ductility demand while others prove relatively *benign*, leading to structural behavior reminiscent of ordinary records. Inclusion of arbitrary numbers of either type of record will thus lead to biased estimates of NS inelastic demand (Tothong and Cornell, 2008). Ideally, assembling a set of pulse-like records that closely reflects hazard at a NS site in terms of pulse period, should address the aforementioned problem, since it is known that  $T_p$  plays an important role in determining SDOF and MDOF inelastic demand (Ruiz-García, 2011, Iervolino et al., 2012, Akkar et al., 2004, Alavi and Krawinkler, 2004). However, this is not the case due to the small number of registered directivity ground motions. Indeed, if one attempts to closely match the marginal density of  $T_p$  from disaggregation – such as the one presented in Figure 3.8(a) – he is faced with the problem that in some  $T_p$  intervals there may be very few records to choose from – if any. Since it is unlikely that a sample as small as a couple of records will reproduce

the average trend of inelastic response for some interval of  $T_p$ , this can lead to biased estimates of NS inelastic demand. In order to address this problem posed by the relative scarcity of available pulse-like records within some specific  $T_p$  range restrictions, the following steps were taken: first, the cumulative distribution function (CDF) of  $T_p$  was used to divide the available dataset of pulse-like ground motions (which consists of the impulsive records used in Chapter 2 with the addition of some records from more recent events, some of which will be discussed in the next section), into 5 bins of equal probability (Figure 3.8b).

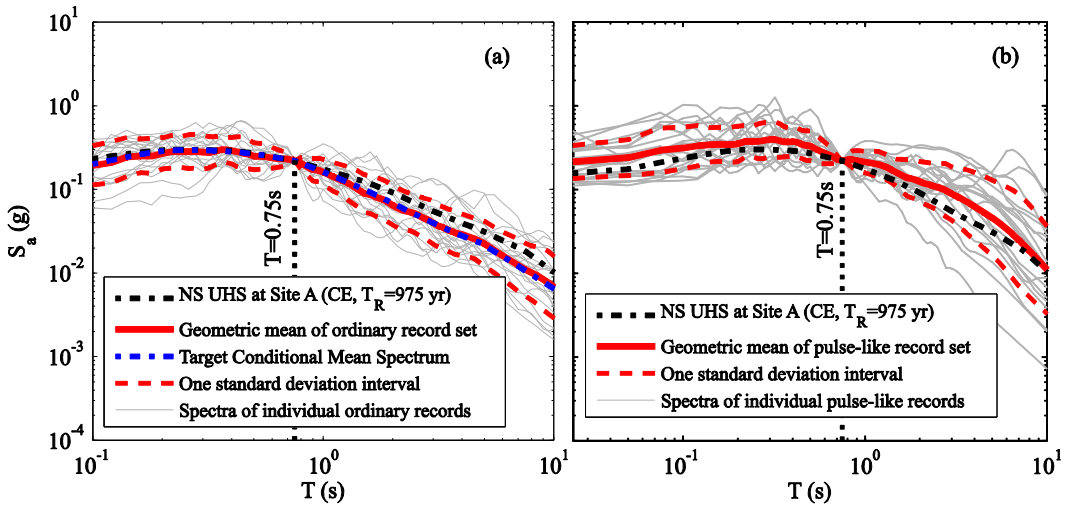


Figure 3.7. Response spectra of the ordinary (a) and pulse-like (b) scaled records selected for the non-linear dynamic analysis of the 5-storey R/C frame ( $T=0.75s$ ). Also shown is the NS uniform hazard (design) spectrum of the considered scenario and – in the case of the ordinary record set – the target conditional mean spectrum.

Given a target number of 20 pulse-like ground motions for the selection, this entails extracting four records from each bin. This strategy effectively relaxes the requisite of closely reflecting the distribution of  $T_p$  predicted by NS hazard yet – as an offset – provides more densely populated record bins from which to choose. This procedure is analogous to that employed by Almufti et al. (2013). The second step consisted is calculating the average pulse period  $\overline{T_p}$  for each bin, deriving the corresponding inelastic displacement ratio  $C_{R|pulse} \left( T_1 / \overline{T_p} \right)$  from Equation (3.4) and finally selecting four records from within each bin whose inter-bin average inelastic spectra match this  $C_{R|pulse}$  as closely as possible. Thus, even when a bin spans a range of rare pulse

periods, such as the one denoted on Figure 8b, the selection is guided towards the average trend exhibited by the entire dataset of impulsive ground motions in an effort to avoid bias due to the scarcity of records within the bin.

This record selection strategy resulted in two sets of pulse-like ground motions being assembled, one for each of the two cases considered. All pulse-like records were scaled to a common spectral ordinate at the first mode period of each structure. In the case of ordinary ground motions, it has been shown to some extent by Shome et al. (1999), that this type of scaling does not introduce bias to inelastic response. This approach was maintained for the pulse-like directivity case as well (see for example Figure 3.7b), since the target distributions of  $T_p$  were obtained from disaggregation conditional on occurrence of these  $S_a(T)$  values. In Figure 3.9, the degree with which these distributions were matched by the selected record sets can be seen. This is despite having relaxed the  $T_p$  matching criterion, due to the binning strategy adopted. The suites of design ground motions obtained (Table A.2) can be said to reflect the impulsive portion of NS seismic hazard for the considered cases.

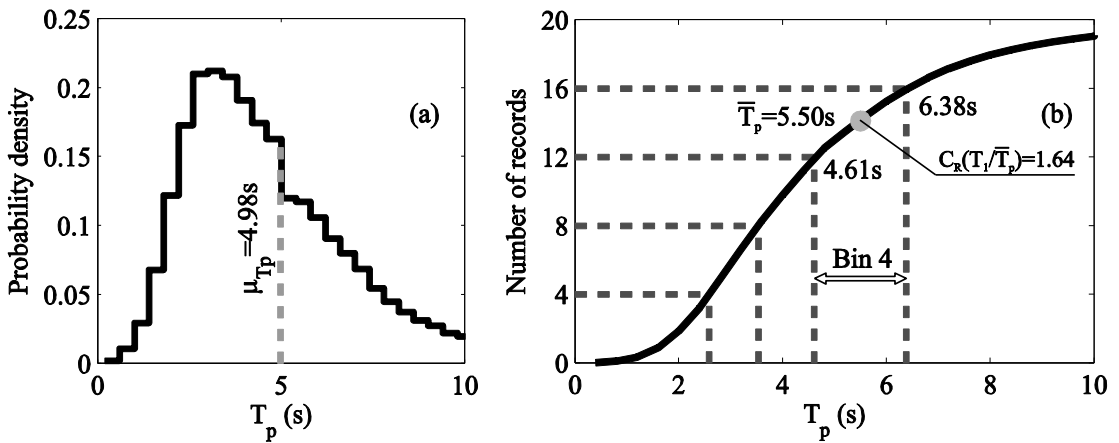


Figure 3.8. (a) PDF of pulse period from disaggregation of NS hazard ( $T=1.00s$ ,  $T_R=975$  yr) and (b) corresponding CDF multiplied by intended number of pulse-like records to be selected and divided into five bins of equal probability for the calculation of inelastic displacement ratio corresponding to the average pulse period of each bin.

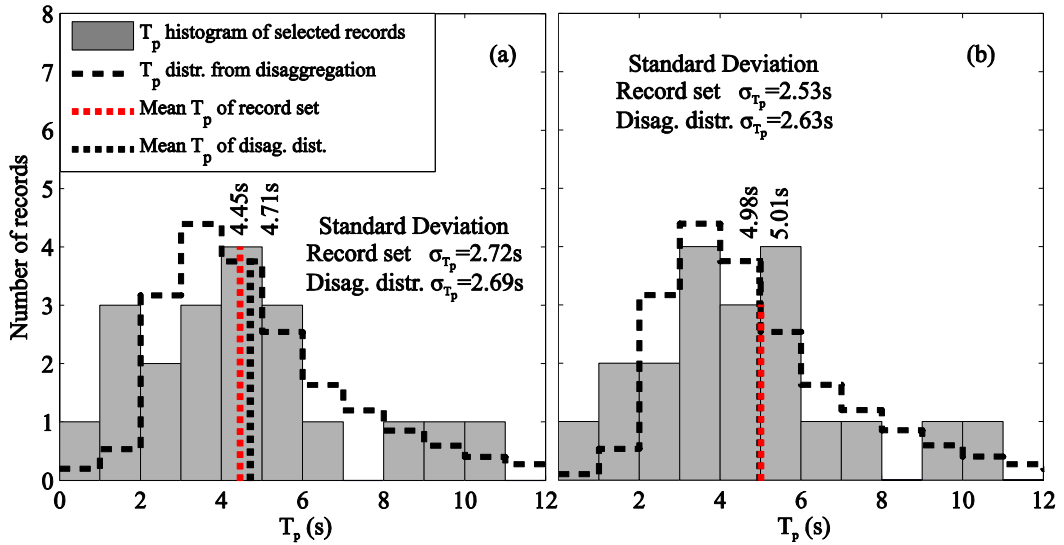


Figure 3.9. Comparison of target densities of pulse period with  $T_p$  histograms of the selected pulse-like ground motion sets for the  $T=0.75s$  five-storey frame (a) and the  $T=1.00s$  six-storey frame (b). The probability densities have been scaled in order for their areas to coincide with those of the histograms. Relevant statistics also are shown.

### 3.7.3 NON-LINEAR RESPONSE HISTORY ANALYSES

Having obtained these record sets, non-linear models of the two frames were finally each subjected to the two suites of scaled ordinary and pulse-like ground motions. Results in terms of peak roof displacement for each individual record can be found in Tables A.1-2 of the appendix. Note that in the case of the six-storey frame, the El Centro Array #10 record of the Imperial Valley earthquake (California, 1979) and the Lucerne record of the Landers earthquake (California, 1992) both caused collapse of the structure, even though the level of seismic hazard under consideration corresponds to a damage limitation performance level; thus, the roof displacement values reported in Table A.2 are the maximum values attained prior to the onset of dynamic instability. A summary of the dynamic RHA is given in Figure 3.10, where relevant response statistics and corresponding DCM estimates, carried over from Table 3.3, are also reported.

It can be observed that dynamic RHA results indicate an overestimation of inelastic demand due to directivity by the DCM adaptation to NS conditions, of the order of 12%. This can be partly attributed to the fact that the continuous lognormal model for  $T_p$  of Chioccarelli and Iervolino (2010) employed during NS-PSHA cannot be effectively reproduced by recorded ground motions due to the rarity of very long

duration directivity pulses, in excess of 10s. Furthermore, the RHA confirms the premise that NS inelastic demand due to potential directivity effects can supersede ordinary demand enough to merit special consideration. This is in agreement with the findings of previous studies by Akkar and Metin (2007) and Champion and Liel (2012 – note that Champion and Liel dealt with the effect of FD on collapse probability, while the present study deals with its effect on mean demand, rather than probability of exceeding capacity).

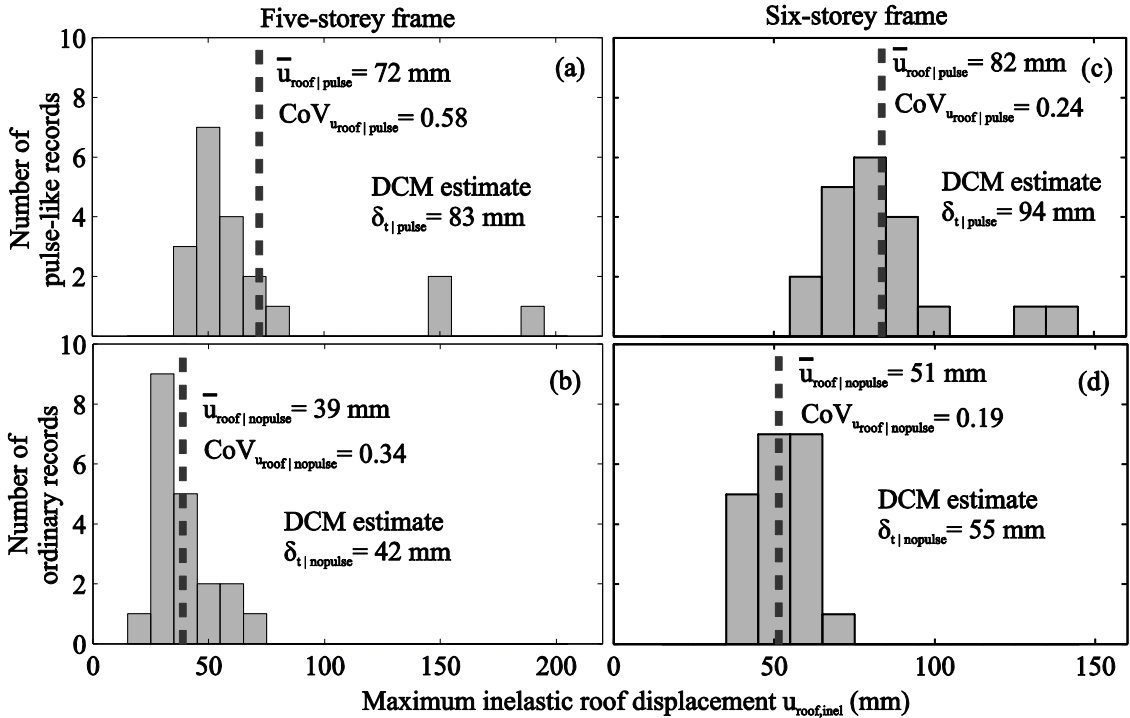


Figure 3.10. Histograms of maximum inelastic roof displacement resulting from non-linear dynamic RHA for the five-storey ( $T_1=0.75s$ ) frame subjected to the pulse-like (a) and ordinary (b) excitation suite as well as the respective results for the six-storey ( $T_1=1.00s$ ) frame (c) and (d).

### 3.8 DISCUSSION

The presented study dealt with the implementation of the DCM to estimate the design demand for structures in near-source conditions. The modifications required to adapt the DCM were discussed both in terms of elastic (i.e., seismic hazard) and inelastic demand. A set of illustrative applications was also provided, where single-fault NS design scenarios, assuming different site-to-source configurations and source seismicity, were considered in order to represent a variety of cases with respect to

expected forward directivity effects. The DCM was implemented in this context for modern-code-conforming R/C frames, and compared to design for classical hazard and inelastic demand.

The results may help to quantify the significance of accounting for NS-FD in structural design and assessment. Inasmuch as the DCM can provide a useful estimate of structural seismic performance in the inelastic range, FD was shown to induce appreciable increase – in an engineering sense – in displacement demand. More specifically, increments in the assessment of target displacement due to NS-FD effects range from 34%-77% in the case most prone to directivity amongst those examined, to 8%-27% in the case least prone to FD effects among those considered. This behaviour was further confirmed when dynamic RHA was performed using suites of ground motions carefully selected in order to reflect NS demand for such a design scenario.

Regarding inelastic structural demand at sites near the source, it was found that this can considerably (percentagewise) exceed demand as computed without accounting for directivity effects, particularly when longer return period performance levels are considered. Furthermore, it was shown that this discrepancy may be exacerbated at sites whose orientation with respect to the fault renders them particularly prone to FD ground motions.

Depending on the distribution of causal event magnitudes most likely to characterize a given source, potential directivity may be manifest by means of relatively short duration pulses, comparable with the periods of natural vibration of typical building structures. This type of impulsive records would mostly affect the elastic response of such structures; that being the case, computing design spectra by means of NS-PSHA should constitute the key step towards estimating NS inelastic response, combined with use of inelastic spectra for NS-FD. However, it was also shown that there are cases where NS effects have small-to-negligible influence on seismic hazard (expressed in elastic response IMs) around a specific spectral region, and yet produce more pronounced increase in mean inelastic demand for structures whose fundamental period places them in that portion of the elastic response spectrum. The non-linear dynamic analyses carried out corroborate this finding. It was shown that this effect can be explicitly accounted for in structural analysis by use of NS hazard disaggregation results, which provide additional information with respect to the design spectrum.

**CHAPTER 3 REFERENCES**

Akkar S, Metin A. Assessment of Improved Nonlinear Static Procedures in FEMA-440. *J Struct Eng –ASCE* 2007; **133**(9): 1237-1246.

Akkar S, Yazgan U, Gülkan P. Deformation limits for simple non-degrading systems subjected to near-fault ground motions. *Proc 13<sup>th</sup> World Conf Earthq Eng* 2004; Vancouver BC, Canada, Paper no. 2276.

Alavi B, Krawinkler H. Behavior of moment-resisting frame structures subjected to near-fault ground motions. *Earthquake Engng Struct Dyn* 2004; **33**(6): 687–706.

Almufti I, Motamed R, Grant DN, Willford M. Incorporation of Velocity Pulses in Design Ground Motions for Response History Analysis using a Probabilistic Framework. *Earthq Spectra* 2013; (in press).

ASCE, Prestandard and Commentary for the Seismic Rehabilitation of Buildings, FEMA-356, developed by ASCE for FEMA, Washington, D.C., 2000.

Baker JW. Identification of near-fault velocity and prediction of resulting response spectra. *Proc Geotech Earthq Eng and Struct Dyn IV* 2008; Sacramento, CA.

Baker JW, Cornell CA. Vector-valued intensity measures for pulse-like near-fault ground motions. *Eng Struct* 2008; **30**:1048-1057.

Baker JW, Jayaram N. Correlation of spectral acceleration values from NGA ground motion models. *Earthq Spectra* 2008; **24**: 299-317.

Baltzopoulos G, Chioccarelli E, Iervolino I. Accounting for near-source effects in the displacement coefficient method for seismic structural assessment. *Proc COMPDYN 2013, 4<sup>th</sup> ECCOMAS Thematic Conf Comp Methods Struct Dyn Earthq Eng* 2013; Kos Island, Greece, 12–14 June.

Bazzurro P, Cornell CA. Disaggregation of seismic hazard. *B Seismol Soc Am* 1999; **89**: 501–520.

Benjamin J, and Cornell, CA. Probability, Statistics and Decisions for Civil Engineers. McGraw-Hill Companies 1970.

Boore DM, Atkinson GM. Ground-motion prediction equations for the average horizontal component of PGA, PGV and 5%-damped PSA at spectral periods between 0.01 s and 10.0 s. *Earthq Spectra* 2008; **24**(1): 99–138.

BSSC, *NEHRP guidelines for the seismic rehabilitation of buildings*, FEMA-273, developed by ATC for FEMA, Washington, D.C., 1997.

CEN, EN 1992-1-1 Design of concrete structures. General rules and rules for buildings, European Committee for Standardization, Brussels, 2004.

CEN, EN 1998-1 Design of structures for earthquake resistance – Part 1: General rules seismic actions and rules for buildings, European Committee for Standardization, Brussels, 2004.

Champion C, Liel A. The effect of near-fault directivity on building seismic collapse risk. *Earthquake Engng Struct Dyn* 2012; **41**: 1391-1409.

Chenouda M, Ayoub A. Inelastic Displacement Ratios of Degrading Systems. *J Struct Eng - ASCE* 2008; **134**: 1030-1045.

Chioccarelli E, Iervolino I. Near-source seismic demand and pulse-like records: A discussion for L'Aquila earthquake. *Earthquake Engng Struct Dyn* 2010; **39**: 1039-1062.

Chioccarelli E, Iervolino I. Near-source seismic hazard and design scenarios. *Earthquake Engng & Struct Dyn* 2013; **42**: 603-622.

Chioccarelli E, Iervolino I. Sensitivity analysis of directivity effects on PSHA. *B Geofis Teor Appl* 2014; **55**(1): 41-53.

Dimakopoulou V, Fragiadakis M, Spyarakos C. Influence of modeling parameters on the response of degrading systems to near-field ground motions. *Eng Struct* 2013; **53**: 10-24.

Erduran E, Kunnath SK. Enhanced Displacement Coefficient Method for Degrading Multi-Degree-of-Freedom Systems. *Earthq Spectra* 2010; **26**(2): 311-326.

FEMA, Improvement of nonlinear static seismic analysis procedures, FEMA-440 prepared by ATC, Washington, D.C., 2005.

Gutenberg B, Richter CF. Frequency of Earthquakes in California. *B Seismol Soc Am* 1944; **34**: 185-188.

Iervolino I, Cornell CA. Probability of occurrence of velocity pulses in near-source ground motions. *B Seismol Soc Am* 2008; **98**(5): 2262–2277.

Iervolino I., Chioccarelli E, Baltzopoulos G. Inelastic Displacement Ratio of Near-Source Pulse-like Ground Motions. *Earthquake Engng Struct Dyn* 2012; **41**: 2351-2357.

Jayaram N, Lin T, Baker JW. A Computationally Efficient Ground Motion Selection Algorithm for Matching a Target Response Spectrum Mean and Variance. *Earthq Spectra* 2011; **27**(3): 797-815.

Kalkan E, Kunnath SK. Assessment of current nonlinear static procedures for seismic evaluation of buildings. *Eng Struct* 2007; **29**: 305-316.

Krawinkler H, Seneviratna GDPK. Pros and Cons of a Pushover Analysis of Seismic Performance Evaluation. *Eng Struct* 1998; **20**(4-6): 452-464.

Mander JB, Priestley MJN, Park R. Theoretical Stress-Strain Model for Confined Concrete. *J Struct Eng* 1988; **114**(8): 1804-1826.

Miranda E, Estimation of Inelastic Deformation Demands of SDOF Systems. *J Struct Eng* 2001; **127**(9): 1005-1012.

Reiter L. *Earthquake hazard analysis, issues and insights*. NY: Columbia University Press, 1990.

Ruiz-García J. Inelastic Displacement Ratios for Seismic Assessment of Structures Subjected to Forward-Directivity Near-Fault Ground Motions. *J Earthq Eng* 2011; **15**(3): 449-468.

Seneviratna GDPK, Krawinkler HK. *Evaluation of inelastic MDOF effects for seismic design*. Report no. 120, John A. Blume Earthquake Engineering Center, Stanford University, 1997.

Shahi SK, Baker JW. An Empirically Calibrated Framework for Including the Effects of Near-Fault Directivity in Probabilistic Seismic Hazard Analysis. *Bulletin of the Seismological Society of America* 2011; **101**(2): 742-755.

Shome N, Cornell CA, Bazzurro P, Carballo E. Earthquake, records and nonlinear responses. *Earthq Spectra* 1999; **3**(14): 469-500.

Somerville PG, Smith NF, Graves RW, Abrahamson NA. Modification of empirical strong ground motion attenuation relations to include the amplitude and duration effects of rupture directivity. *Seismol Res Lett* 1997; **68**: 199-222.

Tothong P, Cornell CA. Structural performance assessment under near-source pulse-like ground motions using advanced ground motion intensity measures. *Earthquake Engng Struct Dyn* 2008; **37**(7): 1013-1037.

Tothong P, Cornell CA, Baker JW. Explicit directivity-pulse inclusion in probabilistic seismic hazard analysis. *Earthq Spectra* 2007; **23**: 867-891.

Tothong P, Luco N. Probabilistic seismic demand analysis using advanced ground motion intensity measures. *Earthquake Engng Struct Dyn* 2007; **36**: 1837-1860.

Wells DL, Coppersmith KJ. New empirical relationships among magnitude, rupture length, rupture width, rupture area, and surface displacement. *Bulletin of the Seismological Society of America* 1994; **87**(4): 974-1002.

## Chapter 4

# Building an Extended Database of Near-Source Ground Motions Affected by Directivity

### 4.1 INTRODUCTION

As already discussed in Chapter 3, the relatively low number of available NS ground motions displaying directivity effects poses a challenge when attempting to evaluate structural performance in NS environments using naturally recorded accelerograms. This motivates researchers to take a closer look at NS acceleration recordings in search of signs of directivity or simply of impulsive character. During the time that has elapsed since the completion of the work presented in Chapter 2, new NS ground motions from recent seismic events have been made available to engineers. Thus, this study also follows this pattern, in order to take advantage of and incorporate the newly available information in the subsequent research.

Shahi and Baker sought to populate the list of pulse-like ground motions with records satisfying their classification criteria, including records where the causal effect of the pulse is not related to forward directivity (e.g., site effects, fling steps, basin effects etc.) and the orientation of the principal impulsive component deviates from the fault-normal. In quantitative terms, this approach bore undeniable fruits; the number of 91 pulse-like records identified by Baker (2007) rose to 179 in Shahi and Baker (2011) and 243 in a later work by the same authors (Shahi and Baker, 2014), which was based on the more extensive NGA West 2 ground motion database (Ancheta et al., 2013).

Even though it can be argued that ground motions with velocity pulses of diverse origins, may nonetheless cause similar structural response, the validity of pooling all pulse-like ground motion together should depend on the intended application. For example, it may not be appropriate to include pulses due to site-effects, when the objective is to estimate the probability of pulse occurrence due to FD.

The present study focuses on collecting pulse-like ground motions most likely related to rupture directivity. This is motivated by the fact that the ultimate objective

is a dataset of impulsive ground motions to be used for the characterization of NS structural response in relation to pulse duration  $T_p$ . Velocity pulses significantly deviating from the characteristic double-sided, early-arriving waveform associated with directivity, may not exhibit the same type of correlation between inelastic structural response and pulse period. Thus, even though the pulse identification approaches suggested Baker (2007) and Shahi and Baker (2014) are adopted for the most part, some effort is made to discern those velocity pulses most likely to have been the result of directivity for eventual inclusion in the database.

## 4.2 METHODOLOGY

Having as a starting point the dataset used for the regression analysis presented in Chapter 2, the quest for additional directivity ground motions mainly focuses on recent seismic events which provided a multitude of NS recordings, such as the Parkfield 2004 (California) event, the Darfield 2010 and Christchurch 2011 (New Zealand) events and the South Napa 2014 (California) event. It is noteworthy that the Chi-chi 1999 (Taiwan) event, which was very well documented and resulted in an uncommonly large number of NS recordings, accounts for a good portion of the difference in number of records between those used by Iervolino et al. (2012) and those identified as pulse-like in Shahi and Baker (2011). This will be discussed in some detail in the following paragraphs, as the NS records from the Chi-chi earthquake are put into scrutiny.

In all examined cases, both the Baker (2007) and Shahi and Baker (2014) pulse identification algorithms were employed. Baker (2007) classifies a ground motion as pulse-like when its pulse indicator (PI) score exceeds 0.85, a criterion shown in Equation (4.1) and simultaneously  $PGV \geq 30 \text{ cm/s}$ .

$$PI = \frac{1}{1 + e^{[-23.3 + 14.6 \cdot (PGV \text{ ratio}) + 20.5 \cdot (\text{energy ratio})]}} > 0.85 \quad (4.1)$$

The terms “PGV ratio” and “energy ratio” appearing in Equation (4.1), refer to the ratios of PGV and energy corresponding to the candidate impulsive waveform extracted from a given record, to the corresponding quantities of the original (prior to extraction) record.

On the other hand, the methodology proposed in Shahi and Baker (2014) defines PI as shown in Equation (4.2) and classifies a ground motion as pulse-like when  $PI > 0$ .

$$\begin{aligned}
 PI &= 9.384 \cdot (0.76 - PC - 0.0616 \cdot PGV) \cdot \\
 &\cdot (PC + 6.914 \cdot 10^{-4} \cdot PGV - 1.072) - 6.179 > 0, \\
 PC &= 0.63 \cdot (PGV \text{ ratio}) + 0.777 \cdot (\text{energy ratio})
 \end{aligned}
 \tag{4.2}$$

Even though the latter more recent algorithm was calibrated on a larger dataset, the results from implementation of the original algorithm of Baker (2007) are nevertheless of interest. Given that, in Baker (2007), PGV is not hardcoded into the classification criterion (as is the case in Equation 4.2), it can be used to provide some insight into lower amplitude motions whose waveforms might still bear the effects of directivity (e.g., Boatwright, 2007). Even though classification results between the two algorithms are not unanimous, it should be stressed that the signal processing part is common to both, as is (perhaps more importantly) the definition of pulse period as the pseudo-period of the highest-coefficient wavelet. Additionally, the pulse classification results of Hayden et al. (2012) were consulted wherever applicable.

Regarding the orientation in which directivity pulses are sought, there are several considerations and research findings to take into account. Even though directivity is generally expected in the fault-normal direction for both strike-slip and dip-slip faulting mechanisms (Somerville et al., 1997), it has been observed that reverse faulting sometimes refuses to follow this rule, with strong velocity pulses appearing at near-fault sites at orientations departing significantly from the strike-normal (Howard et al., 2005).

Furthermore, some larger magnitude events actually ruptured more than one fault; thus even events generally classified as strike-slip may contain portions of the rupture surface that include significant components of slip along the dipping direction. One such example is the Darfield (M7.0, New Zealand) 2010 earthquake, an event generally classified as strike-slip, which was nevertheless triggered by a reverse rupture (Holden et al., 2011).

For some events, a complicated geometry of the rupture surface has been inferred, which cannot be captured by the typical rupture-plane simplification; thus in those cases, the fault-normal direction may locally exhibit unexpected variation. Finally, there is the possibility for fling-step and directivity effects to be superimposed, particularly for sites near the projection of the up-dip extremity of a dip-slip rupture, making the directivity pulse and its orientation harder to discern. The Chichi (M7.6, Taiwan) 1999 earthquake, is a prime example of both of these effects.

For all of these reasons, this study subscribes to the approach of Shahi and Baker (2011 and 2014) i.e., considering more orientations than the fault-normal during

ground motion classification as pulse-like or ordinary. However, since the objective is to focus on directivity-induced pulses, the appropriate orientation of the horizontal component of ground motion is examined on a case-by-case basis with the aid of literature relevant to each event and/or ground motion record.

### **4.3 SEISMIC EVENTS CONSIDERED**

#### **4.3.1 PARKFIELD, CALIFORNIA 2004 EARTHQUAKE**

The Parkfield M6.0 event of 28/09/2004 ruptured a portion of the San Andreas fault in central California and provided a multitude of NS ground motion recordings (Shakal et al., 2004). Gillie et al. (2010), included 15 of those records in their study of directivity ground motions. Shahi and Baker (2014) on the other hand, identified 12 records from this event as pulse-like. These authors consider that directivity is the most likely cause of the pulse for 11 of these, which is a view shared in the present work.

#### **4.3.2 NEW ZEALAND 2010 AND 2011 EVENTS**

A common feature of the Darfield M7.0 (3/09/2010) and the Christchurch M6.2 (21/02/2011) New Zealand events is that they both provided a substantial amount of NS ground motions, the vast majority of which were recorded over deep alluvial deposits, including liquefiable top strata. As a matter of fact, some near-fault sites experienced widespread liquefaction during both events. This raises the question of whether or not some of the observed narrow-band NS ground motions owe their existence to site effects.

Furthermore, the Christchurch earthquake resulted from reverse-oblique rupture and according to Bradley and Cubrinovski (2011) any directivity-related pulses are to be found at orientations closer to the strike-parallel rather than the strike-normal direction. This meant that in the aftermath of the implementation of the classification algorithms, some judgment was required to separate impulsive waveforms that can be linked to directivity from those having other causal effects.

An example of this can be seen in Figure 4.1, where NS pulses from these two events, which are probably unrelated to directivity, are shown in the first two panels. In the first of these panels, part of the velocity time-history recorded at Styx Mill Transfer Station during the Darfield earthquake is shown. The very long velocity pulse indicated is most likely due to soft soil effects. This site is situated over a 28m thick alluvial deposit interspersed with layers of an estimated shear wave propagation velocity inferior to 200m/s (gravel content in some of the layers precluded cyclic mobility in both events).

In the second panel, the velocity time-history of the Lyttelton Port Company record from the Christchurch earthquake is shown. This was one of the few ground motions

from these events recorded on rock (at sea-level, behind the higher-altitude relief overlooking Christchurch from the south). However, rupture propagation and slip along the rupture surface were directed mostly away from this location, which is situated on the hanging-wall of the fault, diminishing the likelihood of directivity.

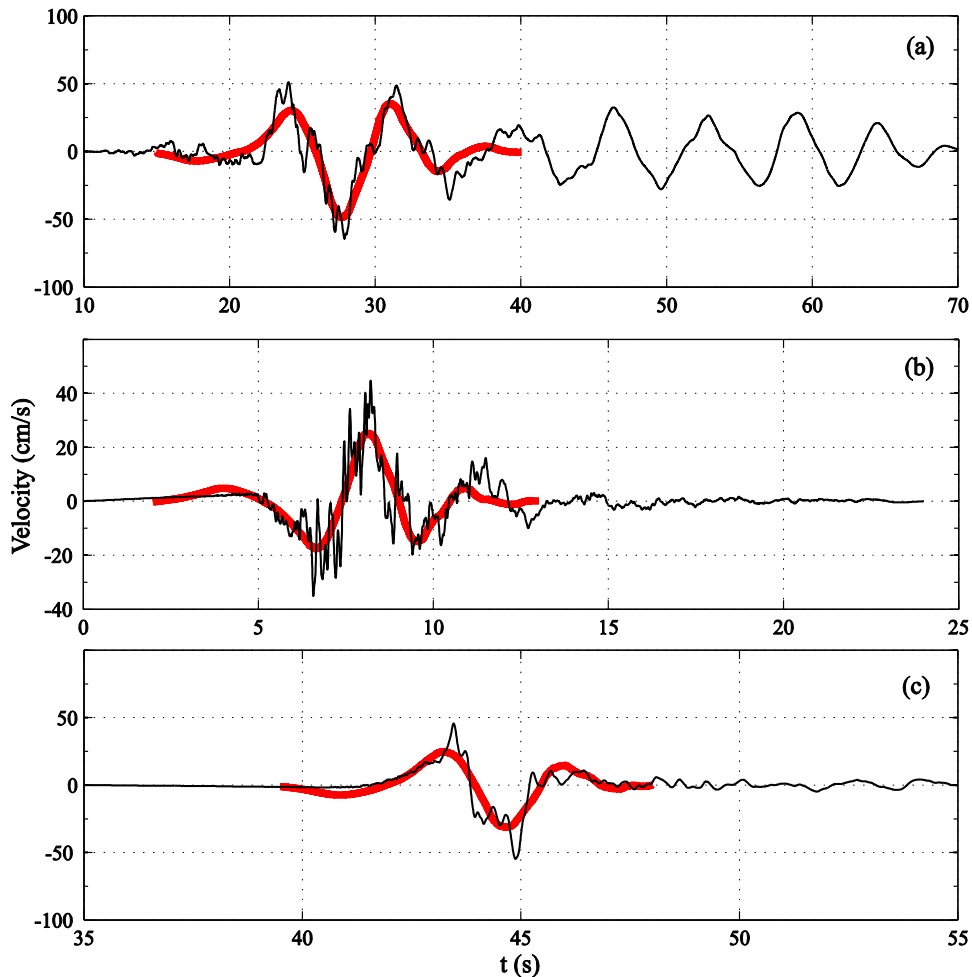


Figure 4.1: Examples of velocity pulses attributable to various causes (candidate pulses displayed in red). (a) Styx Mill Transfer Station record from the Darfield (New Zealand) 3/09/2010 event, pulse-like feature most likely caused by soft soil site-effects. (b) Lyttelton Port Company record from the Christchurch (New Zealand) 21/02/2011 event, impulsive characteristics possibly due to hanging-wall effects. (c) Lovall Valley, Loop Road record from the South Napa (California) 24/08/2014 event. Velocity pulse likely caused by forward rupture directivity.

One possible explanation for the pulse, which can be discerned underneath the higher-frequency portion of the record and is shown in the figure, is the constructive

interference of waves refracted on the discontinuity of the rupture surface back into the hanging wall. However, a documented interpretation is beyond the scope of this study.

### 4.3.3 CHICHI, TAIWAN 1999 EARTHQUAKE

The 1999 M7.6 Chichi (Taiwan) earthquake is notable, as already mentioned, for the large number of NS recordings it provided (no little thanks to the extents of the horizontal projection of the rupture surface). Records from this event were not taken into account by Iervolino and Cornell (2008) or Iervolino et al. (2012). However, this was not due to any lack of pulse-like records but due to the overabundance thereof, which could give rise to concerns of single-event bias in the models developed therein.

Another concern stemming from examination of the Chichi NS records, is the presence of many very long duration pulses (in excess of 6.0s) in combination with the complicated rupture geometry and faulting style. Fling step pulses in these records are possibly overlapping directivity pulses. Although this is not a problem in itself, the shape of the wavelet used in the classification algorithms of both Baker (2007) and Shahi and Baker (2014), is such that pulse period may be somewhat inflated in the presence of a single-sided pulse.

One such example can be seen in Figure 4.2, where the velocity time history of record TCU068 is shown, at an orientation half-way between the strike-normal and strike parallel.

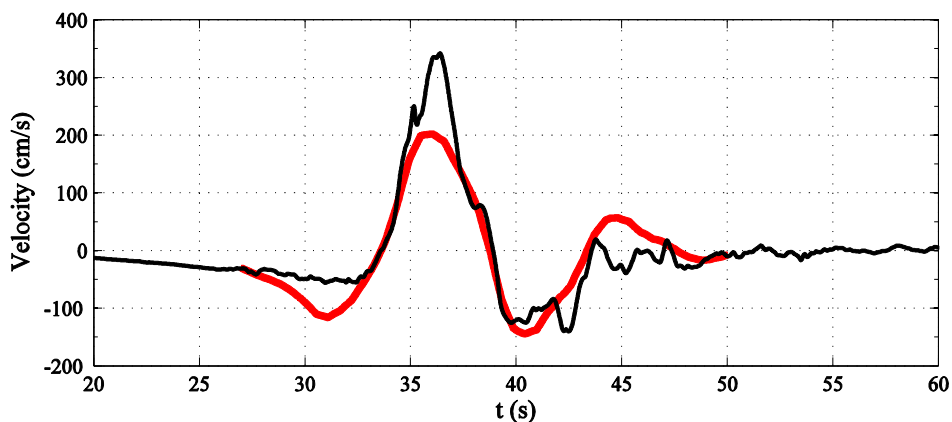


Figure 4.2. Velocity time history of TCU068 record from the 1999 Chichi (Taiwan) earthquake and extracted pulse according to Shahi and Baker (2014) superimposed in red. The first component Daubechies wavelet pseudo-period results in pulse period determined at 12.3s.

This station is notorious for one of the highest PGV values ever recorded and constitutes a frequently cited example of a fling-step pulse (e.g., Bolt, 2004). Fling step pulses, due to their one-sided nature, may pose a challenge to a single double-sided 2<sup>nd</sup> order Daubechies wavelet to accurately represent them (pulse period according to Baker, 2007, is defined based on the pseudo-period of the first wavelet component of the pulse). In this case, a pulse period of  $T_p = 12.3\text{s}$  is reported after implementation of the Shahi and Baker (2014) procedure. By comparison, pulse classification results of Hayden et al. (2012) reported in the NIST CGR (2011) document, assign a peak-to-peak velocity (PPV) duration of 6.0s, which is more consistent with the one-sided nature of the fling waveform.

In lack of a generally accepted methodology for identifying and isolating fling-step pulses, 17 records from this event were selected for inclusion in the database based on two criteria:

- The selected records were required to exhibit good correlation between pulse period  $T_p$  reported by the wavelet transform and predominant period  $T_g$ . Predominant period has often been used in the literature as an alternative definition for pulse period (e.g., Ruiz-García, 2011). It was defined by Miranda (1993) as the period where maximum pseudo-spectral velocity (PSV) is manifest. The correlation coefficient between these two definitions of pulse period within the Chichi records selected for inclusion in the FD dataset was found to be  $\rho_{T_p, T_g} = 0.92$ , where  $\rho_{T_p, T_g}$  is given in Equation (4.3) for a sample of  $n$  ground motions.

$$\rho_{T_p, T_g} = \frac{\hat{c}ov(T_p, T_g)}{\hat{\sigma}_{T_p} \cdot \hat{\sigma}_{T_g}}, \quad \hat{c}ov(T_p, T_g) = 1/n \cdot \sum_1^n (T_{p,i} - \bar{T}_p) \cdot (T_{g,i} - \bar{T}_g), \quad (4.3)$$

$$\hat{\sigma}_T = 1/n \cdot \sum_1^n (T_i - \bar{T})^2, \quad \bar{T} = 1/n \cdot \sum_1^n T_i$$

This value is superior to the one that characterizes the overall dataset (which is  $\rho_{T_p, T_g} = 0.83$  - see Figure 4.5b) and is considered as a first indication that cases of dubious pulse duration identification have been for the most part avoided.

- Handpicking of records for inclusion was further assisted by comparison of pulse characterization with the published results of the independent classification methodology of Hayden et al. (2012 and 2014). Note that the pulse classification algorithm in question, whose results can be found in the

NIST CGR (2011) report, involves the records being submitted to some preliminary filtering prior to the determination of PPV duration. This methodology (and corresponding definition of  $T_p$ ) leads to no pulse periods in excess of 6.0s being reported.

#### 4.3.4 OTHER NOTABLE SEISMIC EVENTS

Some other events that produced few NS records but were, nevertheless, included in this investigation were the 26/12/2003 Bam (Iran) M6.6 earthquake (see Ghayamghmian and Hisada, 2010) and the 3/11/2002 Denali (Alaska) M7.9 earthquake. The single record included in the database from the latter event is of particular interest (Ellsworth et al., 2004). Even though the Denali earthquake was a predominantly strike-slip event, the directivity pulse in the TAPS pump station #10 (see Figure 4.3) is not to be found exclusively in the fault-normal direction, but also in directions towards the strike.

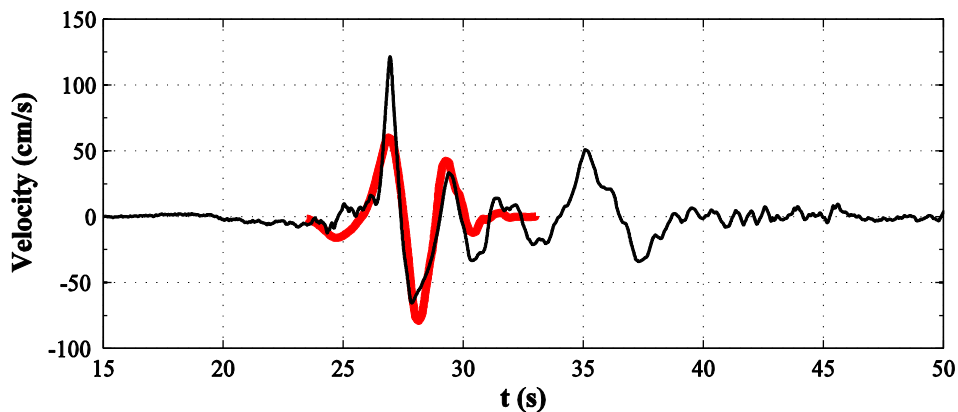


Figure 4.3: Denali (Alaska) 3/11/2002, TAPS pump station 10 velocity time history (azimuth of horizontal component 56°).

As a matter of fact, a permanent ground displacement of approximately 3.0m was recovered from the fault-parallel component, where a fling-step pulse is clearly visible. Furthermore, there are signs of supershear rupture on the Denali fault (see Ellsworth et al., 2004, for more details – the earthquake ruptured 3 different faults, for a total of 340 km rupture length; Pump station #10 was 3 km away from the Denali fault rupture surface and 85 km from the epicenter). According to Howard et al. (2005), supershear rupture may be responsible for fling-step and directivity effects being observed closer together orientation-wise.

Finally, 13 NS records from the South Napa (California) 24/08/2014 M6.0 event were subjected to the pulse classification algorithm proposed by Shahi and Baker (2014) and the 4 identified as pulse-like were included in the dataset. An example can be seen in the last panel of Figure 4.1.

#### 4.4 RESULTS AND DISCUSSION

As a result of the investigation summarized in the preceding sections, a total of 130 records were tagged as pulse-like directivity ground motions. A detailed list can be found in Appendix B, Table B.1. In Figures 4.4 and 4.5, some relevant statistics derived from this dataset are shown. Figure 4.4(a) shows the results of a linear regression of log-pulse period against earthquake magnitude. The regression parameters (slope, intercept and  $\hat{\sigma}_{\ln T_p}$ ) are very close to the ones obtained by Chioccarelli and Iervolino (2010), which is the model used in the NS-PSHA applications presented in Chapter 3. The definitions of the coefficient of determination  $R^2$  and the root of mean square error  $\hat{\sigma}_{\ln T_p}$  reported in Figure 4.4(a) are given as Equation (4.4) below (for a generic variable  $y$  sampled  $n$  times, with sample mean  $\bar{y}$  and model estimation for the mean  $\hat{y}$ ).

$$SSE = \sum_{i=1}^n (\hat{y}_i - y_i)^2, R^2 = 1 - \frac{SSE}{\sum_{i=1}^n (\hat{y}_i - \bar{y})^2}, \hat{\sigma}_y = \sqrt{\frac{SSE}{n-2}} \quad (4.4)$$

Figure 4.4(b) shows the linear correlation between pulse period and predominant period of the ground motion  $T_g$ .

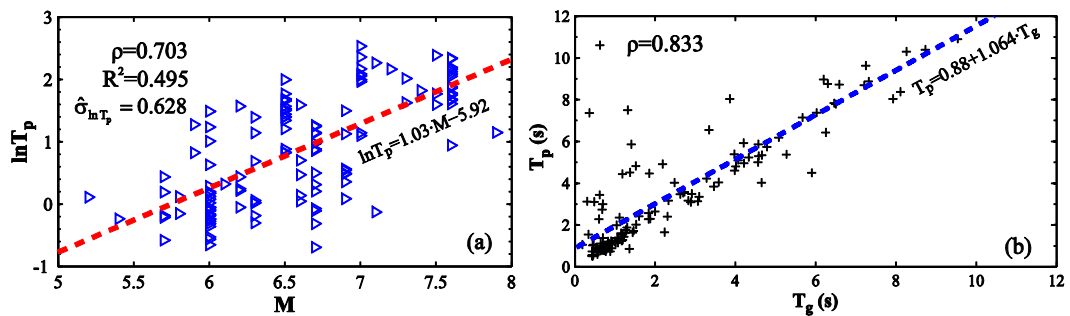


Figure 4.4: Linear regression of log-pulse period against magnitude (a) and linear correlation between pulse period ( $T_p$ ) and period of maximum PSV (or predominant period  $T_g$ ) (b).

Figure 4.5 shows the distribution of normalized residuals for PGV and spectral acceleration at a period of vibration equal to pulse duration  $T_p$ .

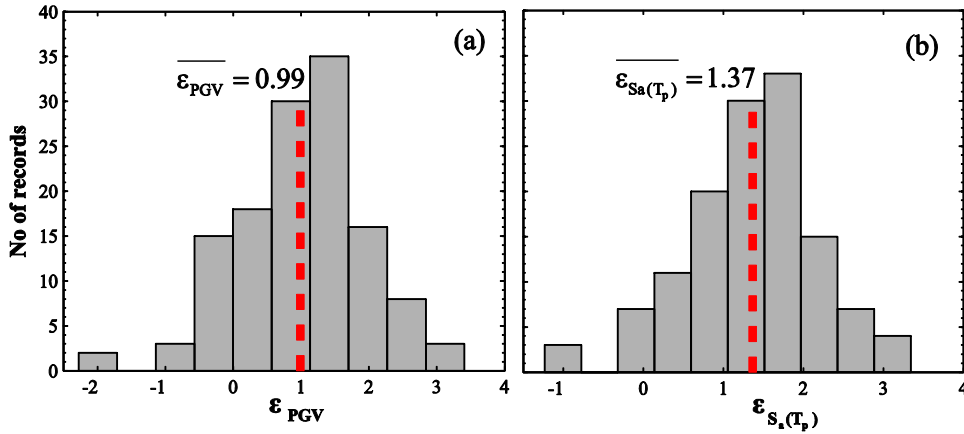


Figure 4.5: Normalized residuals for the peak ground velocity (a) and spectral pseudo-acceleration at  $T=T_p$  (b) for pulse-like directivity ground motions.

These residuals were calculated according to Equation (4.5) using the ground motion prediction equation of Boore and Atkinson (2008), which does not account for NS directivity (see also the discussion in Chapter 3).

$$\epsilon_{IM} = \frac{\log IM - \overline{\log IM}}{\sigma_{\log IM}} \quad (4.5)$$

In Equation (4.5) – which is given for a generic intensity measure  $IM$  –, overbar denotes mean and  $\sigma_{\log IM}$  standard deviation of the logarithms. As already mentioned in Chapter 3, the fact that these residuals exhibit non-zero mean, has led to various suggestions for corrections factors to be applied to GMPEs (e.g., Shahi and Baker, 2011) for use in current-practice NS-PSHA.

What should also be mentioned, is that not all ground motions considered pulse-like in Iervolino and Cornell (2008) and Iervolino et al. (2012) are included in the dataset. As a matter of fact, five of those records were excluded. The reason for this are the differences in waveform observed between some (corrected) records as originally recovered from the PEER NGA database (Chiou et al., 2004) and the same records as they were published in the NGA West 2 database, where a different correction protocol was followed –see Ancheta et al., (2013).

In the latter case, some older records were re-digitized and subjected to acausal Butterworth filters, with baseline correction being refrained from. While the different

processing protocols are very relevant (e.g., Boore and Akkar, 2003) the actual pulse-like features of the records in question were put very much in doubt after application of the NGA West 2 correction protocol, hence their exclusion.

This extended database of pulse-like FD ground motions, is used in the subsequent Chapter 5, where the response of non-trivial-backbone oscillators subjected to impulsive records is investigated.

**CHAPTER 4 REFERENCES**

Ancheta T, Darragh R, Stewart J, Seyhan E, Silva W, Chiou B, Wooddell K, Graves R, Kottke A, Boore D, Kishida T, Donahue J. *PEER NGA-West2 database, Technical Report 2013/03*. Pacific Earthquake Engineering Research Center, Berkeley, California, 2013.

Baker JW. Quantitative Classification of Near-Fault Ground Motions Using Wavelet Analysis. *Bulletin of the Seismological Society of America*, 2007; **97**(5), 1486-1501.

Boatwright J. The persistence of directivity in small earthquakes. *Bulletin of the Seismological Society of America* 2007; **97**(6):1850–1861.

Bradley BA, Cubrinovski M. Near-source Strong Ground Motions Observed in the 22 February 2011 Christchurch Earthquake. *Seismological Research Letters* 2011; **82** (6): 853-865.

Bolt B. Engineering Seismology, In: *Earthquake Engineering: From Engineering Seismology to Performance-Based Engineering*, eds. Bozorgnia Y, Bertero VV, CRC Press, FL, 2004.

Boore DM, Akkar S. Effect of causal and acausal filters on elastic and inelastic response spectra. *Earthquake Eng Struct Dyn* 2003; **32**: 1729–1748.

Boore DM, Atkinson GM. Ground-motion prediction equations for the average horizontal component of PGA, PGV and 5%-damped PSA at spectral periods between 0.01 s and 10.0 s. *Earthq Spectra* 2008; **24**(1): 99–138.

Chiou B, Darragh R, Gregor N, Silva W. NGA Project Strong-Motion Database. *Earthquake Spectra* 2008; **24**(1): 23-44.

Ellsworth WL, Celebi M, Evans JR, Jensen EG, Kayen R, Metz MC, Nyman DJ, Roddick JW, Spudich P, Stephens CD. Near-field ground motion of the 2002 Denali fault, Alaska, earthquake recorded at pump station 10. *Earthq Spectra* 2004; **20**(3): 597-615.

Ghayamghmian MR, Hisada Y. Near-fault strong motion complexity of the 2003 Bam earthquake (Iran) and low-frequency ground motion simulation. *Geophys. J. Int.* 2010; **170**: 679-686.

Gillie JL, Rodriguez-Marek A, McDaniel C. Strength reduction factors for near-fault forward-directivity ground motions. *Engineering Structures* 2010; **32**: 273-285.

Hayden C, Bray JD, Abrahamson NA, Acevedo-Cabrera AL. Selection of near-fault pulse motions for use in design. *15th World Conference on Earthquake Engineering*, 2012, Lisbon, Portugal.

Hayden C, Bray J, Abrahamson N. Selection of Near-Fault Pulse Motions. *J Geotech Geoenviron Eng* 2014, **140**(7).

Holden C, Beavan J, Fry B, Reyners M, Ristau J, Dissen R, Villamor P, Quigley M. Preliminary source model of the Mw 7.1 Darfield earthquake from geological, geodetic and seismic data. *Proceedings of the Ninth Pacific Conference on Earthquake Engineering Building an Earthquake-Resilient Society*, 14-16 April, 2011, Auckland, New Zealand.

Howard JK, Tracy CA, Burns RG. Comparing observed and predicted directivity in near-source ground motion. *Earthq Spectra* 2005; **21**(4): 1063–1092.

Miranda E. Site-Dependent Strength Reduction Factors. *Journal of Structural Engineering*, 1993; **119**(12): 3503-3519.

NIST GCR 11-917-15. *Selecting and Scaling Earthquake Ground Motions for Performing Response-History Analyses*. National Institute of Standards and Technology, Engineering Laboratory, Gaithersburg, Maryland, 2011.

Ruiz-García J. Inelastic Displacement Ratios for Seismic Assessment of Structures Subjected to Forward-Directivity Near-Fault Ground Motions. *J Earthq Eng* 2011; **15**(3): 449-468.

Shakal A, Haddadi H, Graizer V, Lin K, Huang M. Some Key Features of the Strong-Motion Data from the M 6.0 Parkfield, California, Earthquake of 28 September 2004. *Bulletin of the Seismological Society of America* 2006; **96**(4b): S90-S118.

Shahi SK, Baker JW. An efficient algorithm to identify strong velocity pulses in multi-component ground motions. *Bulletin of the Seismological Society of America* 2014, 104(5), 2456–2466.

Shome N, Cornell CA, Bazzurro P, Carballo E. Earthquake, records and nonlinear responses. *Earthq Spectra* 1999; **3**(14): 469-500.



## Chapter 5

# Near-source Pulse-like Seismic Demand for Multi-Linear Backbone Oscillators

### 5.1 INTRODUCTION

Estimating the seismic demand for structures expected to respond inelastically to future earthquakes attaining a certain intensity, is one of the key issues in performance based earthquake engineering (PBEE, see for example Krawinkler and Miranda, 2004). Procedures relating the structural seismic demand to that of an *equivalent* single-degree-of-freedom oscillator, collectively known as nonlinear static procedures, have carved their own niche in the PBEE framework and have gradually found their way into modern codes for seismic design and assessment.

One such procedure has already been the focus of attention in this work, when an extension of the DCM to account for NS directivity effects was proposed in Chapter 3. Initially, these static nonlinear procedures made recourse to inelastic spectra derived for simple elastic-perfectly-plastic or bilinear oscillators and the methodology of Baltzopoulos et al. (2014) does not stray from that path. However, the request for demand estimates that delve deeper into the inelastic range and arrive at quantifying dynamic collapse capacity, led researchers to also investigate the seismic demand of oscillators with more complex backbone curves such as the trilinear backbone depicted in Figure 5.1.

In order to fully describe this backbone curve mathematically in ductility - reduction factor normalized coordinates, three parameters are required: the slope  $\alpha_h$  of a plastic or hardening branch that simulates post-yield ductility and the slope  $\alpha_c$  and “capping point” ductility  $\mu_c$  of a softening branch that is typical of the behavior of most structures, either brittle or ductile, that reach a maximum strength and then exhibit in-cycle degradation that leads them to negative stiffness due to strength loss. The phenomena that actually lead to negative stiffness in a real structure can include

P-Δ effects and material strength degradation (often both). Negative stiffness can be encountered on the static pushover curves of many types of structures, such as braced steel frames, moment resisting steel frames, concrete frames or other types of structure that exhibit sensitivity to second order effects.

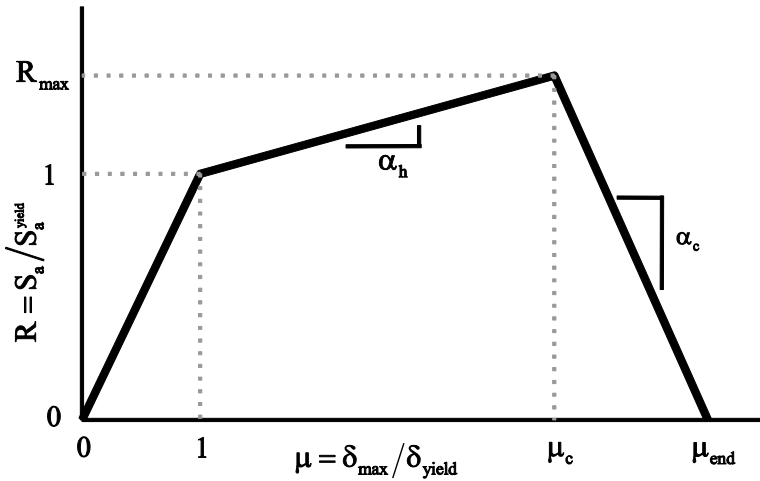


Figure 5.1. Representation of trilinear backbone curve in normalized coordinates (ductility  $\mu$  in the abscissa and reduction factor  $R$  in the ordinate) and defining parameters: post-yield hardening slope  $\alpha_h$ , softening branch negative slope  $\alpha_c$  and capping ductility  $\mu_c$  which separates the hardening and softening branches.

Incorporating all of these additional parameters into a tidy predictive equation can be a daunting task that will likely require a sacrifice of accuracy for simplicity. Vamvatsikos and Cornell (2006) introduced a methodology that employs incremental dynamic analysis (IDA, Vamvatsikos and Cornell, 2002) and a suite of 30 ordinary ground motions, to compute and model the median, as well as 16% and 84% fractile, IDA curves of multi-linear backbone oscillators. The resulting analytical model, intended for being directly incorporated into a software tool, eschews simplicity and compactness in favor of better fit to the data and the ability to represent the variability inherent in seismic response.

The study presented in this chapter, closely follows the methodology of Vamvatsikos and Cornell (2006), in order to develop an elaborate  $R$ - $\mu$ - $T/T_p$  relation for pulse-like NS motions and oscillators characterized by the generic trilinear backbone depicted in Figure 5.1. To this end, the suite of one hundred and thirty pulse-like-identified ground motions, presented in Chapter 4 is employed. The resulting

analytical model captures both the trend and heterogeneity of NS pulse-like seismic demand, while making the important inclusion of pulse period as a predictor variable.

## 5.2 INCREMENTAL DYNAMIC ANALYSIS AND THE *SPO2IDA* TOOL

Incremental dynamic analysis is a procedure to semi-empirically estimate probabilistic seismic structural demand and capacity. This well-established procedure, typically entails a non-linear numerical model of the structure which is subjected to a suite of ground motion records, all scaled at a common IM level. This IM level is gradually increased by applying a common scale factor simultaneously to all the records, in order to reveal the entire range of post-yield response of the structure, conditional to several IM values, up to global dynamic instability and consequent collapse.

During IDA, structural response to a single record is usually represented by plotting two scalars against each other: a ground motion intensity measure characterizing the various scaled incarnations of the record and an engineering demand parameter (EDP) characterizing the amplitude of response. EDP is usually selected to be some measure of local or global structural deformation (e.g., maximum roof displacement or maximum interstory drift for a frame structure). The ground motion IM should be monotonically scalable and should ideally possess some further desirable properties, such as *sufficiency*, *efficiency* and *scaling robustness* (see Luco and Cornell, 2007). Commonly used IMs are PGA and 5% damped, first mode period spectral acceleration  $S_a(T_1, 5\%)$ .

By plotting EDP responses to the various scaled versions of a single record on the abscissa and corresponding IM level on the vertical axis, one obtains a single record IDA curve. IDA curves start with a linear segment corresponding to elastic response and then evolve into, generally speaking, non-monotonic functions of ground motion IM. An IDA curve eventually culminates into a *flat-line*, a horizontal segment of continuously increasing EDP at constant IM level, signifying the onset of global dynamic instability.

Once a set of IDA curves has been collected, representing the entire suite of ground motions, it is an efficient practice to *summarize* the curves into sample fractile statistics. Typically sample medians, 16% and 84% fractiles are calculated; employing these particular statistics to obtain summary IDA curves has certain advantages:

- fractiles are invariant with respect to monotonic one-on-one transformations of the variables (see Benjamin and Cornell, 1970).
- these fractile values fit well with the common assumption that the conditional distribution of EDP given IM can be represented by a lognormal distribution, when 16% and 84% would be one standard deviation of the logs distant from the median.
- once a certain portion of the records begin to collapse the structure, other statistics such as sample mean, become impossible to calculate, while counted sample fractiles are still a valid option (see Shome and Cornell, 2000).

While single IDA curves may be non-monotonic and even discontinuous, summary fractile IDA curves are usually better-behaved, being monotonic and continuous more often than not. For more details on the intricacies of this method, the interested reader is referred to Vamvatsikos and Cornell (2002 and 2004). Given that the structural model should ideally be sufficiently complex so as to be able to represent the full repertoire of non-linear responses and eventual failure mechanisms and the suite of records large enough to account for the inherent variability of seismic loading, it is fair to say that IDA can be a computationally intensive procedure.

This fact motivated Vamvatsikos and Cornell (2006) to develop a software tool which provides a shortcut, at the cost of introducing some approximation in the process. Having observed that summary IDA curves of SDOF systems with multi-linear backbone curves exhibit a consistent behavior in correspondence with each segment of the backbone (elastic, post-yield hardening, post-cap softening and residual strength segments, the first three represented in Figure 5.1), they used IDA to investigate the response of a large population of oscillators with varying backbone parameters.

Having thus mapped the behavior of many backbone shapes against a suite of ordinary ground motions, not affected by directivity, they proposed an intricate analytical model, aptly named the *SPO2IDA* tool, capable of reproducing the IDA curves of these SDOF systems without having to run any analysis. Taking into consideration the well-established methodologies that allow studying the inelastic response of first-mode dominated MDOF systems by means of a substitute SDOF approximation (which were discussed in some length in Chapter 3), it becomes clear that *SPO2IDA* is essentially nothing less than a complex R- $\mu$ -T relation. What sets *SPO2IDA* apart from the more traditional R- $\mu$ -T relations, its complexity

notwithstanding, is the fact that it also provides information on the dispersion of seismic response around the central value.

A sample application of SPO2IDA can be seen in Figure 5.2, which shows estimated fractile IDA curves for an oscillator with natural period of vibration  $T=1.0s$ , plotted over its backbone curve (SPO2IDA tool available online at the time of writing at <http://users.ntua.gr/divamva/software/spo2ida-allt.xls> , last accessed on the 15th of March, 2015).

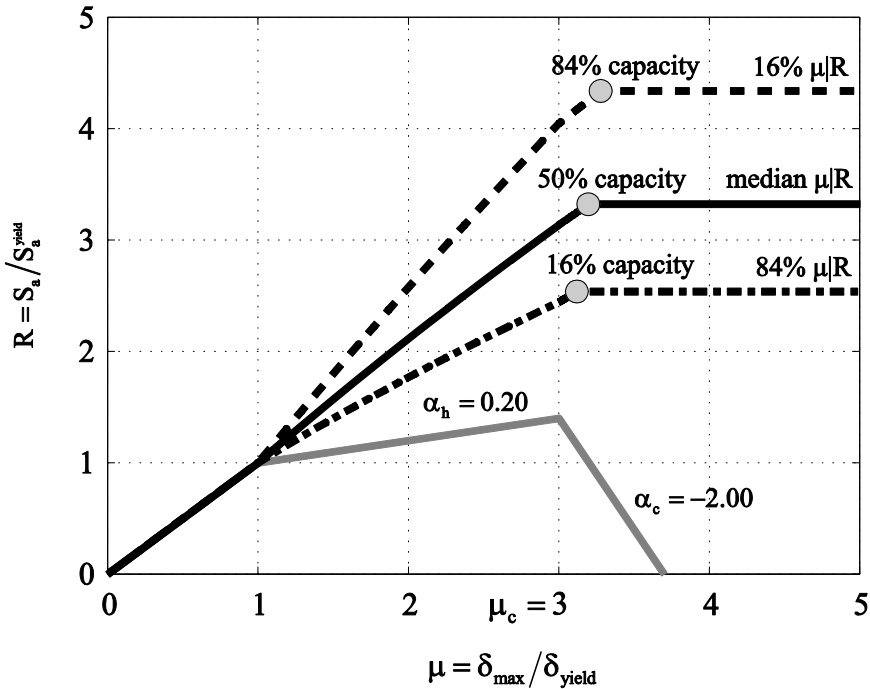


Figure 5.2. SPO2IDA estimates of the 16%, 50% and 84% fractile IDA curves for an oscillator with natural period of vibration  $T=1.0s$ , superimposed over the oscillator’s trilinear backbone curve. The backbone is defined by hardening post-yield slope 20% of the elastic, capping ductility at  $\mu_c = 3.0$  and a softening branch with descending slope of -200%.

The objective of the study presented in this chapter, is to follow in the footsteps of Vamvatsikos and Cornell (2006) and employ IDA on SDOF systems using the set of pulse-like records assembled in Chapter 4 (Table B.1 of Appendix B) in order to develop the equivalent of an  $R-\mu-T/T_p$  relation appropriate for NS FD ground motions, which also takes the shape parameters of a trilinear backbone curve into account.

### 5.3 MODELLING NEAR-SOURCE PULSE-LIKE SEISMIC DEMAND FOR TRI-LINEAR BACKBONE OSCILLATORS USING IDA

#### 5.3.1 PREDICTOR VARIABLES

A parametric model that predicts the fractile IDA curves of pulse-like FD ground motions (which will occasionally be referred to as “*pulse-like IDAs*” for brevity in the following) for SDOF oscillators featuring a generic trilinear backbone will necessarily include all the parameters that uniquely define the geometry of the backbone curve. This means that post-yield hardening slope  $\alpha_h$ , capping ductility  $\mu_c$  and post-cap descending slope  $\alpha_c$  (see Figure 5.1) should all be included as predictor variables in the model, as in Vamvatsikos and Cornell (2006). An additional variable that must be included in the model is pulse period, by virtue of its demonstrable predictor value for the inelastic response of this type of ground motion (Iervolino et al., 2012).

In this case, pulse period is included as the denominator of the normalized period ratio  $T/T_p$ , in a manner analogous (but subtly different as will be seen below) to the regression model presented in Chapter 2. As a consequence, the ground motion IM adopted for the IDAs is strength reduction factor  $R$ , defined as per Equation (5.1). EDP of choice for the SDOF systems is ductility  $\mu$  defined as the ratio of maximum displacement to displacement at yield – Equation (5.2).

$$R = \frac{S_a(T_i = \kappa \cdot T_{p,i}, \xi = 5\%)}{S_a^{\text{yield}}(T_i, 5\%)}, \quad \kappa = \frac{T}{T_p} \in [0.10, 2.00] \quad (5.1)$$

$$\mu = \frac{\delta_{\text{max}}}{\delta_{\text{yield}}} \quad (5.2)$$

This effectively means that IDA curves computed in this study for given values of the  $T/T_p$  ratio, collect the responses of oscillators with different vibration periods (since, in general, every record has a different pulse duration  $T_p$  associated with it) and thus only make sense as cross-sectional data when plotted in normalized  $\mu, R$  coordinates.

In the regression model for pulse-like inelastic displacement ratios of Iervolino et al. (2012), whose development was presented in Chapter 2, it was considered that the predictive equation should not extend to  $T/T_p$  ratios smaller than 0.20. The

reasoning behind this choice was the desire to avoid mixing the response of very low-period oscillators, which is characterized by high ductility demands even when ordinary records are concerned, with the response of moderate-to-long period oscillators subjected to long duration pulses. However, the non-linear RHA results presented in Chapter 3 suggest that moderate-to-long period oscillator inelastic response may still be slightly over-represented in the low  $T/T_p$  ratio region. This concern led to a different approach being adopted in this case. While the  $T/T_p \geq 0.20$  condition is maintained throughout, an additional restriction is imposed, that of only considering response data at each  $T/T_p$  cross-section for which  $T \geq 0.30s$ .

As a consequence, fractile pulse-like IDA curves obtained for  $T/T_p \leq 0.45$  are derived from progressively less records, with a maximum of 49 records out of 130 being excluded at  $T/T_p = 0.20$ . This “excess data” can be used to derive a supplementary model for  $T < 0.30s$  and  $0.20 \leq T/T_p \leq 0.40$  (for  $T/T_p > 0.40$ , a separate low-period oscillator model would not make much sense, since no waveforms with pulse duration of less than 0.50s have been classified as impulsive – consult Table B.1).

### 5.3.2 HYSTERETIC RULE

During development of the predictive model for pulse-like inelastic displacement ratios of Iervolino et al. (2012), only bilinear SDOF oscillators with positive post-yield stiffness and a kinematic hardening hysteretic rule were considered. However, it was found by Rahnama and Krawinkler (1993) — and later confirmed by Vamvatsikos and Cornell (2006) — that when oscillators, which feature a descending branch are concerned, this type of hysteretic rule is not representative of how actual structures have been observed to behave during experiments.

With this information in mind, a peak-oriented, moderately pinching hysteresis rule developed by Ibarra and Krawinkler (2005) was adopted for the present study. This hysteretic rule does not include any cyclic strength degradation, but this is considered to be of secondary importance. Strength degradation only tends to supersede the shape of the backbone in importance when severe degradation is encountered in low-period structures; however, given the range of pulse-periods associated with the NS-FD record suite employed in this study (see Chapter 4 and Appendix B) the model is more oriented towards moderate to long period structures and cyclic degradation is not included in the hysteretic rule used in the analyses.

### 5.3.3 EQUIVALENT DUCTILITY CONCEPT

A straightforward way of tackling the problem of modelling pulse-like IDAs could be to run a very large number of individual incremental dynamic analyses in an attempt to span the entire parameter space of  $\alpha_c$ ,  $\alpha_h$ ,  $\mu_c$  and  $T/T_p$ . However, structural responses exhibit a complicated interdependency with respect to the four parameters (backbone characteristics and normalized period), which cannot be regarded independently one from another; this means that considering all their meaningful combinations leads to a population of SDOF oscillators numbering in the thousands and an amount of IDAs which can be very copious to obtain and manage.

Fortunately, one can take advantage of the experience accumulated by Vamvatsikos and Cornell (2006) to drastically reduce the amount of necessary analyses. More specifically, it was found that the equivalent ductility  $\mu_{eq}$  concept (see Figure 5.3), which was introduced by the aforementioned authors in their analogous study of ordinary ground motion IDAs, can also be employed in the case at hand.

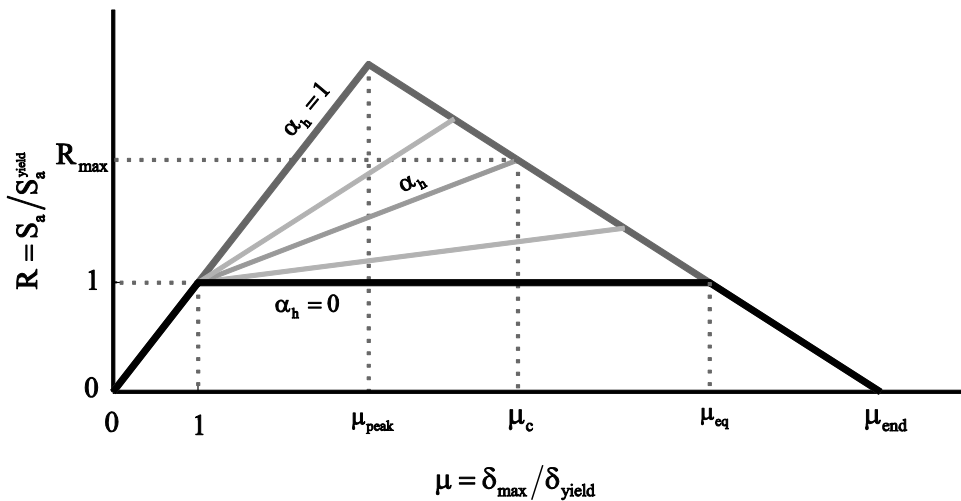


Figure 5.3. Schematic representation of the “equivalent ductility”  $\mu_{eq}$  concept.

Vamvatsikos and Cornell (2006) found that oscillators with a generic backbone containing both a hardening segment and negative-stiffness softening branches with

coincident post-capping slope  $\alpha_c$ , such as those shown in Figure 5.3, have a very similar part of the IDA between capping ductility  $\mu_c$  and the flat-line. The flat-line actually develops at some point slightly prior to reaching zero strength at  $\mu_{\text{end}}$ , which is given by Equation (5.3).

$$\mu_{\text{end}} = \mu_c + \frac{1 + \mu_c \cdot \alpha_h - \alpha_h}{|\alpha_c|} \quad (5.3)$$

Furthermore, flat-line height among these oscillators varies in an almost linear fashion between the two extremes marked by  $\alpha_h = 0$  and  $\alpha_h = 1$  in Figure 5.3. Therefore, for any tri-linear oscillator with given capping ductility  $\mu_c$ , one needs only determine ductility at maximum strength reduction factor  $\mu_{\text{peak}}$ , given by Equation (5.4) and equivalent ductility  $\mu_{\text{eq}}$  where an  $\alpha_h = 0$  oscillator meets the common negative branch and is given by Equation (5.5).

$$\mu_{\text{peak}} = \frac{1 + \mu_c \cdot |\alpha_c| + \alpha_h \cdot (\mu_c - 1)}{1 + |\alpha_c|} \quad (5.4)$$

$$\mu_{\text{eq}} = \mu_c + \frac{\alpha_h \cdot (\mu_c - 1)}{|\alpha_c|} \quad (5.5)$$

As long as a comprehensive model is available for these limit cases, linear interpolation can be used to provide the IDA curves of the intermediate oscillators. One such example of median pulse-like IDA curves for a set of fully-trilinear backbone oscillators is given in Figure 5.4. These oscillators all belong to the same “family” of backbone curves, characterized by  $\mu_{\text{eq}} = 8$ . It can be seen that the corresponding capacity points follow a distinct descending pattern, as  $\mu_c$  approaches  $\mu_{\text{eq}}$ .

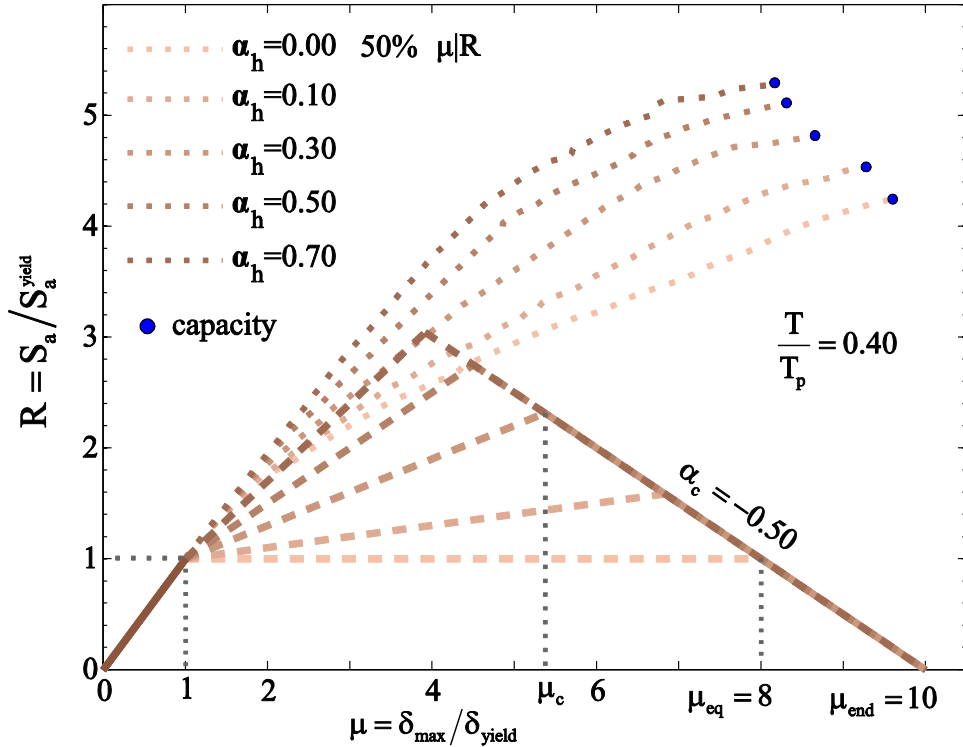


Figure 5.4. Median pulse-like IDAs for a family of coincident post-capping slope oscillators with  $\mu_{eq} = 8$  and  $T/T_p = 0.40$ . Earlier arrival at capping ductility consistently leads to almost proportionately earlier arrival at capacity.

### 5.3.4 SCOPE OF THE MODEL

The SPO2IDA framework provides a powerful methodology for the development of a model that is tantamount to an  $R$ - $\mu$ - $T/T_p$  relation. This model comes in the form of predictive equations (to be elaborated below) for what was previously termed “pulse-like IDAs”. However, it cannot be stressed enough that these IDAs resulting from scaling a suite of NS-FD ground motions to various levels of the  $S_a(T_i, 5\%) / S_a^{yield}(T_i, 5\%)$  ratio (see Equation 5.1), cannot and should not be used to *directly* estimate statistics of structural response, in the same way that one would use an ordinary ground motion IDA.

The reason behind this, is that  $S_a(T_1, \xi)$  is not a *sufficient* IM with respect to inelastic drift response when NS FD is involved – as was already discussed in Chapter 3 (see also Tothong and Cornell, 2008). Due to this fact, estimates of NS structural demand

that maintain use of  $S_a(T_1, \xi)$  as IM, also take pulse period  $T_p$  into account (e.g, Champion and Liel, 2012, Baltzopoulos et al., 2014).

However, as was shown in Chapter 3, for a given NS site, at different levels of  $S_a(T_1, \xi)$ , the probability of FD effects being causal for the occurrence of said level of IM, as well as the pulse periods responsible, vary. Simply put, no single stripe of  $T/T_p$  can be representative of all the scale factors on the IM axis at an actual site.

Therefore, pulse-like IDAs should be regarded as building blocks to be used towards estimating NS seismic demand and capacity, rather than direct estimators thereof. Put in other words, the analytical model elaborated below, should be regarded as an  $R$ - $\mu$ - $T/T_p$  relation, which needs to incorporate site-specific information on  $T_p$  before it can provide results directly applicable in a PBEE framework.

## 5.4 DEVELOPMENT OF THE ANALYTICAL MODEL

### 5.4.1 intermediate steps towards attaining the full model

Fractile IDA curves obtained for SDOF systems belonging to the same “family” of trilinear backbones with coincident post-cap negative stiffness, were observed by Vamvatsikos and Cornell (2006) to possess certain similarities among them. It has been already elaborated in section 3.3 of this chapter, that the same properties were confirmed to apply to pulse-like IDAs. This allows the problem to be split into smaller “modules” that can be addressed – to a certain extent – independently of one another, thus facilitating the overall process.

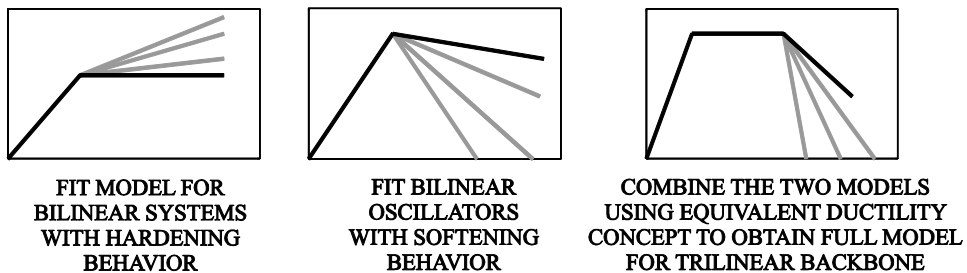


Figure 5.5. Schematic representation of the modular approach towards obtaining a model for the complete trilinear backbone: individual components of the model are developed separately and then combined.

A brief overview of each step follows, so that the subsequent part on the more technical aspects of developing the model can be put into perspective:

- The first step involves dealing exclusively with bilinear oscillators exhibiting hardening (positive slope) post-yield behavior. Pulse-like IDAs spanning the two-parameter space of normalized period  $T/T_p$  and hardening slope  $\alpha_h$  are obtained and processed. An analytical function is subsequently fit against the 16%, 50% and 84% fractile IDA curves. This part of the model, a function of  $T/T_p$  and  $\alpha_h$ , is considered applicable also for oscillators with a full trilinear backbone, from the yield point up to the point of capping ductility  $\mu_c$ .
- The second step deals with bilinear oscillators which exhibit exclusively softening (negative slope) post-yield behavior this time. Same as in the previous step, pulse-like IDAs for various combinations of  $T/T_p$  and capping stiffness  $\alpha_c$  are obtained and used to fit a separate analytical model for the

summary IDA curves. However, negative post-yield stiffness systems, contrary to their hardening bilinear counterparts, eventually reach a point of collapse. These capacity points are therefore located on the fractile IDA curves and an additional functional form is fit for the prediction of their emergence on the previous model. The collapse capacity prediction for the bilinear negative-stiffness system corresponds to the upper-bound interpolation limit for the collapse capacity of the generic trilinear system (the  $\alpha_h = 1$  backbone “yielding” at  $\mu_{peak}$  in the family of backbones shown in Figure 5.3).

- The third and final step in the procedure, requires consideration of oscillators with fully trilinear backbones but with  $\alpha_h = 0$ . Fixing the post-yield slope at the horizontal, pulse-like IDAs are obtained for various values of  $T/T_p$ ,  $\alpha_c$  and  $\mu_c$ . Subsequently, the fractile collapse capacity points are located. These capacities correspond to the “equivalent ductility” backbone, shown in Figure 5.3 plotted with a black line. They also constitute the upper-bound for the interpolation leading to the collapse capacity of the generic trilinear oscillator. These data are therefore used in order to update the collapse capacity model, which should now include  $\mu_{eq}$  and  $\mu_{peak}$  as additional predictor variables and be applicable to any trilinear backbone.

This procedure is schematically summarized in Figure 5.4. At the end, the predictive model for the full trilinear backbone is composed of three equations:

1. one equation describing the pulse-like IDA fractiles up the point of capping ductility  $\mu_c$ ;
2. a second one describing behavior from  $\mu_c$  up to the point of collapse capacity;
3. and a third which predicts flat-line height.

## 5.4.2 CURVE-FITTING STRATEGY AND FUNCTIONAL FORMS

### 5.4.2.1 Bilinear oscillators with hardening post-yield behavior

The analytical functional form selected to model the pulse-like IDA curves for bilinear oscillators with hardening (positive post-yield slope) is given by Equation

(5.6). It is a rational function (in log-space) of ductility given reduction factor fractiles, containing a total of four parameters to be determined by fitting the model to the data.

$$\ln \mu_{x\%} = \frac{a_{x\%} \cdot \ln^2 R + b_{x\%} \cdot \ln R}{c_{x\%} \cdot \ln R + d_{x\%}}, \quad R \in \left(1, R_{(100-x)\%}(\mu_c)\right], \quad x = \{16, 50, 84\} \quad (5.6)$$

The fit follows a *two-stage procedure*: the first stage entails obtaining non-linear least squares estimates of the model parameters  $a_{x\%}$ ,  $b_{x\%}$ ,  $c_{x\%}$  and  $d_{x\%}$  for each distinct backbone (uniquely characterized by  $\alpha_h$ ), normalized period  $T/T_p$  and  $x\%$  fractile IDAs, for a total of 900 instances of parameter estimation. Subsequently, a linear model represented by Equation (5.7) is fit to each of the parameters, in order to capture their dependence on the remaining variables of the problem, namely  $\alpha_h$  and  $T/T_p$ . This second stage entails a total of twelve two-dimensional fits, since for each one of the four parameters, three fractile curves must be accommodated.

$$a_{x\%}, b_{x\%}, c_{x\%}, d_{x\%} = \sum_i \theta_{x\%,i} \cdot p_i(\alpha_h) \cdot q_i\left(\frac{T}{T_p}\right), \quad (5.7)$$

$$\alpha_h \in [0, 0.8), \quad T/T_p \in [0.1, 2.0]$$

The terms  $p_i(\alpha_h)$  and  $q_i\left(\frac{T}{T_p}\right)$  represent simple functions of the variables in parentheses. The following considerations led to the selection of the model jointly represented by Equations (5.6) and (5.7):

- The model should pass through zero in log-space (point 1,1 in regular  $\mu, R$  coordinates) in order to be able to smoothly blend into the preceding elastic part.
- Typical concavity of the fractile  $\mu_{x\%}|R$  IDA curves (especially of the 50% and 84% fractiles) is sometimes reversed in pulse-like IDAs which can exhibit convex initial segments. This is usually observed at higher  $T/T_p$  ratios (above the ones associated with the more aggressive impulsive records for a given oscillator) and post-yield hardening slopes below 15%. While predominantly concave IDA curves are nicely captured by the parabolic (in log-space) equation adopted by Vamvatsikos and Cornell (2006), a model

that smoothly transitions between the two will inevitably need to be more complex, as Equation (5.6) undoubtedly is.

- The model should be able to accommodate slant asymptotes, since in many cases, the initial curvature of the fractile IDAs degenerates into a linear trend. This behavior is characteristic of longer-period systems with  $T/T_p > 1.0$ , particularly when  $\alpha_h > 0.30$ .
- As hardening slope  $\alpha_h$  approaches unity, response will inevitably tend towards the elastic. This practically means that the three fractile IDAs being modelled should collapse to a single unit slope line. Capturing this behavior when fitting Equation (5.7) up to and including  $\alpha_h = 1.0$  can be unnecessarily troublesome, hence the  $0 \leq \alpha_h < 0.80$  limit reported in that equation. Given that already at  $\alpha_h = 0.8$  the three fractiles become for the most part indistinguishable from one another, it is much simpler to interpolate between this and infinitely elastic response, rather than seek to fit the model for steeper post-yield slopes.
- The post-yield response of the bilinear oscillators in question can extend to a theoretically infinite value of ductility, as no dynamic instability will ever occur. However, for practical reasons, a limitation should be imposed up to which the model will be fit. In this case it was chosen to fit Equation (5.6) against the data up to and including  $\mu = 10$ .

Note that the distinction between *linear* and *non-linear* for the curve-fitting of the models involved in this two-stage procedure, refers to linearity (or lack thereof) with respect to the parameters of each model ( $\theta_{x\%,i}$  and  $a_{x\%}$  through  $d_{x\%}$ , respectively) and not the functional forms of the predictor variables involved. Thus, Equation (5.6) represents a non-linear model because the Jacobian of the least-squares optimization problem is not independent of the model parameters. In practical terms, this means that to obtain estimates of the parameters, one must resort to iterative solution schemes which require sets of initial guess values as input. Random selection of starting parameter vectors is not advisable; an unfortunate set of initial conditions can cause the iterations to get bogged down near a local minimum or even failure to converge to a solution altogether.

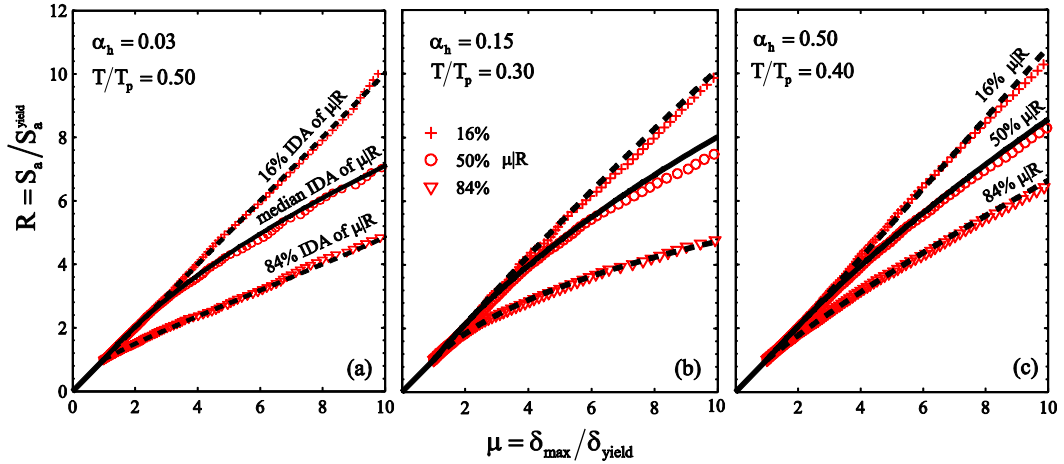


Figure 5.6. Comparison of the fitted model of Equation (5.6) with the underlying data for SDOF systems (a) with  $\alpha_h = 3\%$  at  $T/T_p = 0.50$ , (b)  $\alpha_h = 15\%$  at  $T/T_p = 0.30$  and (c)  $\alpha_h = 50\%$  at  $T/T_p = 0.40$ .

In order to overcome this technical difficulty, a round of preliminary fits was first carried out. Two-parameter linear, parabolic and hyperbolic models were fit to each curve in succession. The fit with the highest  $R^2$  score (defined in Equation 4.4) among the three was then used to calibrate the corresponding initial vector for the complete model. Notice that Equation (5.6) will degenerate into one of the aforementioned simpler models, as some parameters tend to zero or unity (also, it is those limit cases that are most likely to cause numeric instability of a least-squares algorithm). This approach proved efficient in overcoming this problem.

A sample of the obtained results can be seen in Figure 5.6, where the fitted curves for all 3 fractile  $\mu_{x\%} | R$  IDA curves are plotted against the analysis results for three oscillators with increasing post-yield stiffness and for different  $T/T_p$  ratios. Coefficient estimates for Equation (5.7) can be found in Tables C.1-4 of the Appendix.

#### 5.4.2.2 Bilinear oscillators with softening (negative slope) post-yield behavior

As already mentioned above, the appearance of a softening on the backbone curve, automatically introduces the question of collapse capacity into the problem. In the trilinear backbones examined here (where no residual strength part is taken into

consideration), the segment with negative post-yield slope will eventually cross the zero capacity axis at  $\mu_{\text{end}}$  - see Equation (5.4). Dynamic instability, indicated by the characteristic IDA flat-line will actually occur at a ductility level slightly lower than  $\mu_{\text{end}}$ . The height of the flat-line will be henceforth referred to as collapse capacity  $R_{\text{cap}}$  while the corresponding ductility will be indicated as  $\mu_{\text{cap}}$  (ductility at capacity, not to be confused with capping ductility  $\mu_c$ ).

In the case of bilinear oscillators, ascending post-yield slopes starting from close to unity and running up to (and including) the horizontal, were examined in the previous section. However, as soon as the slope of the backbone past the yielding point begins to descend, the additional variable of flat-line height  $R_{\text{cap}}$  must be also accounted for by the model.

Contrary to the hardening case, for which Equation (5.6) gives fractile  $\mu_{x\%} | R$  IDAs, for the negative post-yield slope case it was chosen to fit a reduction factor given ductility (fractile  $R_{x\%} | \mu$ ), model, which is given by Equation (5.8) and supplemented by Equation (5.9).

$$\ln R_{x\%} = \frac{a_{x\%} \cdot \ln \mu}{\ln \mu + b_{x\%}}, \quad \mu \in \left(1, \mu_{\text{cap}(100-x)\%}\right], \quad x = \{16, 50, 84\} \quad (5.8)$$

$$a_{x\%}, b_{x\%} = \sum_i \theta_{x\%,i} \cdot p_i \left( |\alpha_c| \right) \cdot q_i \left( \frac{T}{T_p} \right), \quad (5.9)$$

$$\alpha_c \in [-4.0, -0.05], \quad T/T_p \in [0.1, 2.0]$$

According to Vamvatsikos and Cornell (2004) the  $\mu_{x\%} | R$  and  $R_{(100-x)\%} | \mu$  fractile IDA curves are almost identical, even when the typical IDA properties of continuity and monotonicity are slightly violated. Therefore, collapse capacity  $R_{\text{cap},x\%}$  should also appear on the corresponding  $\mu_{(100-x)\%} | R$  curve. The motivation behind this change of course, lies in the prediction of collapse capacity. As can be seen in Figure 5.7, the tangent slope of each summary IDA curve, progressively decreases as ductility approaches  $\mu_{\text{end}}$ . This means that, as strength reduction factor approaches  $R_{\text{cap}}$ , small variations in reduction factor correspond to much greater variations in ductility.

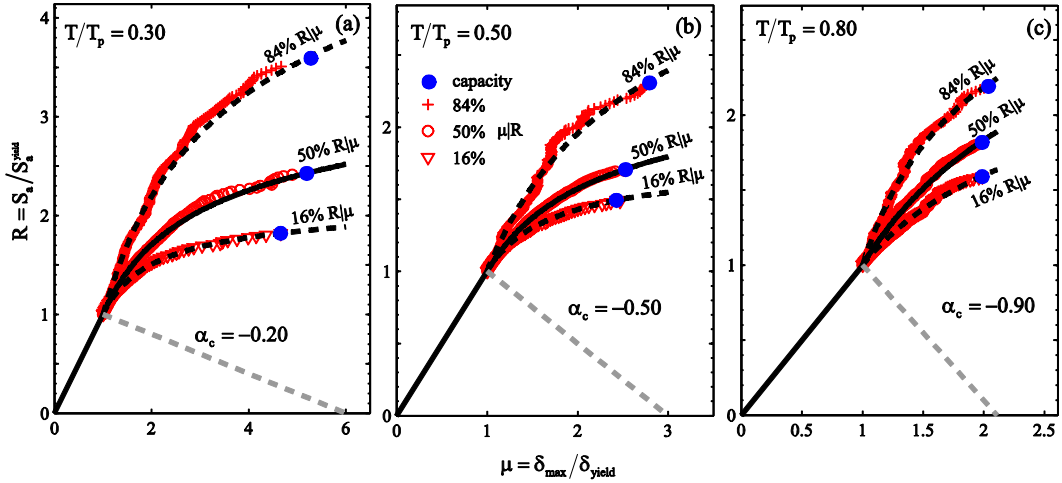


Figure 5.7. Model fit of Equation (5.8) plotted over calculated SDOF pulse-like IDAs for oscillators with (a)  $\alpha_c = -0.20$  at  $T/T_p = 0.30$ , (b)  $\alpha_c = -0.50$  at  $T/T_p = 0.50$  and (c)  $\alpha_c = -0.90$  at  $T/T_p = 0.80$ . Note that the fitted model has been extended past the collapse capacity point only for presentation reasons.

This observation has an important practical implication. Given a *hypothetical* model for  $R_{x\%}|\mu$  or  $\mu_{(100-x)\%}|R$  fractile IDAs with *zero fitting error* (i.e., a hypothetical model exactly reproducing the data) and a separate model for  $R_{cap}$ , some inevitable fitting error in the latter will cause the point of collapse not to fall exactly on the predicted IDA curve. Recalling now the observation about the tangent slope of the curve, it becomes apparent that a small fitting error in predicted flat-line height can cause the flat-line to intersect the IDA “too early” or even unrealistically “late” (beyond  $\mu_{end}$ ).

On the other hand, if one were to adopt a model that predicts ductility at collapse capacity ( $\mu_{cap}$ ), any fitting error would perturb the prediction along the abscissa (assuming  $\mu$  is plotted on the horizontal axis as in Figure 5.7) resulting in negligible difference on the corresponding reduction factor. However, modelling  $\mu_{cap}$  does not automatically resolve the problem; an ordinary least squares fit of Equations (5.8-9) does not guarantee that the  $R_{x\%}|\mu$  curve passes through  $R_{cap}$ . For this reason, the finally adopted solution is the combination of a *weighted* least squares fitting scheme for Equation (5.8) with a model for  $\mu_{cap,x\%}$  fractiles given by Equations (5.10-11).

$$\mu_{\text{cap},x\%} = \mu_c + c_{x\%} \cdot \frac{1 + \alpha_h \cdot (\mu_c - 1)}{|\alpha_c|} \quad (5.10)$$

$$\alpha_h \in [0, 0.8), \alpha_c \in [-4.0, -0.05), x = \{16, 50, 84\}$$

$$c_{x\%} = \beta_{x\%} \cdot \frac{\mu_c - \mu_{\text{peak}}}{\mu_{\text{eq}} - \mu_{\text{peak}}}, \quad (5.11)$$

$$\beta_{x\%} = \{0.85, 1.00, 1.05\} \text{ for } x = \{16, 50, 84\}$$

This concept, employs an adaptive weighting scheme when fitting Equation (5.8) to the data; the point of collapse capacity is given an increased weight until the fitted curve passes through this point within a prescribed tolerance on the ordinate axis (reduction factor). Essentially, the model is “forced” to prioritize capturing the point of collapse capacity with increased accuracy. Thus, we may consider that  $R_{\text{cap},x\%} \approx R_{x\%} | \mu = \mu_{\text{cap},(100-x)\%}$  as per Equation (5.8), having ensured that this estimate is less susceptible to fitting error than direct modelling of the flat-line height.

Finally, it should be noted that throughout Equations (5.8-11) applicability of the model is reported for cap stiffness  $\alpha_c$  greater than 5% (in absolute value). As a matter of fact, the model was also fitted for values of  $0.01 \leq |\alpha_c| \leq 0.05$ . However, as  $|\alpha_c|$  approaches zero and consequently oscillator response begins to resemble that of an elastic-perfectly plastic system, the summary IDA curves exhibit some atypical behavior such as non-monotonicity and irregular fluctuations of collapse capacity (for such systems collapse occurs at uncharacteristically large ductilities). As a consequence, Equation (5.8) does not perform as well in this region; however, it was deemed preferable to maintain this more compact model by inserting the  $|\alpha_c| > 0.05$  disclaimer, rather than attempt to fit a more complicated model to accommodate this marginal inconvenience.

Note that Equation (5.11) corresponds to a linear interpolation (one for each fractile curve). Even though the observed trend is not strictly linear over the entire parameter space this approximation is very attractive in its simplicity. It is also good enough when  $|\alpha_c| > 0.05$ . Coefficient estimates for Equation (5.9) can be found in Tables C.5 and C.6 of the Appendix.

5.4.2.3 Full trilinear backbone oscillators

The analytical models whose development was presented in the preceding paragraphs, can be combined to obtain a prediction for pulse-like IDAs of oscillators in procession of a fully-trilinear backbone curve. The empirical principles underlying this approach have already been either detailed or alluded to in the last two sections. What remains is an illustration of their application.

Such an application is shown in Figure 5.8, for an oscillator characterized by backbone parameters  $\alpha_h = 0.20$ ,  $\mu_c = 6$  and  $\alpha_c = -0.50$ .

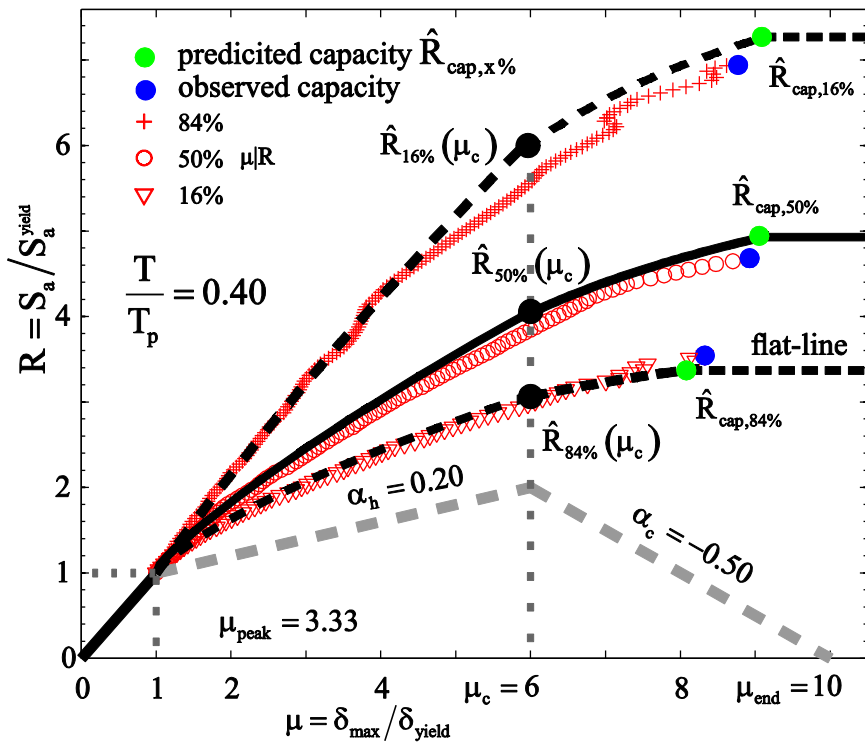


Figure 5.8. Model prediction of the fractile pulse-like IDAs for a trilinear backbone oscillator ( $\alpha_h = 0.20$ ,  $\alpha_c = -0.50$  and  $\mu_c = 6$ ) at  $T/T_p = 0.40$ .

In order to obtain this composite prediction, Equation (5.6) is implemented for as long as  $\mu_{x\%} \leq \mu_c$ , with each segment culminating at reduction factor levels indicated as  $\hat{R}_{x\%}(\mu_c)$  in Figure 5.8. Subsequently, the negative slope part is modeled, by using Equation (5.8) for an interval of ductility  $(\mu_c - \mu_{peak}) < \mu \leq (\mu_{cap} - \mu_{peak})$ . This

segment is adjusted in height at the intersection with the previous model, so that the  $\hat{R}_{x\%}(\mu_c)$  points will belong to both segments, in the interest of continuity.

## 5.5 DISCUSSION OF THE RESULTS

### 5.5.1 COMPARISON WITH CHAPTER 2 DATA

Both the present model and that of Iervolino et al. (2012), which was presented in Chapter 2 of this work, seek to estimate inelastic responses of SDOF systems to pulse-like NS ground motions. Therefore, any meaningful comparison between the two should be desirable as it can potentially offer some additional insights.

However, a direct comparison between predictions of the analytical equations is devoid of meaning, since the present model is intended to predict median demand  $\mu_{50\%}|R$  while the older model predicts mean constant-strength inelastic displacement ratio – Equation (5.12).

$$E[C_R|R] = E\left[\frac{\mu}{R}|R\right] = \frac{E[\mu|R]}{R} \quad (5.12)$$

From Equation (5.12), where  $E[\cdot]$  denotes the mathematical expectation operator, it can be surmised that even for a given reduction factor  $R$ , a direct comparison between the two model estimates does not make sense, since it is known that for the skewed lognormal-like conditional distribution of  $\mu|R$ , the median differs from the mean or  $\mu_{50\%} \neq E[\mu]$  (see also Benjamin and Cornell, 1970).

A comparison that can nevertheless be made, is between the actual data, both sets of which are available. Thus, for the purpose of this comparison, median ductility given reduction factor,  $\mu_{50\%}|R$ , was calculated from the raw data employed in Chapter 2 for the parameter estimation of Equation (2.5) (also in Iervolino et al., 2012) for certain cases and plotted against the data (and model fit) of the present investigation in Figure 5.9.

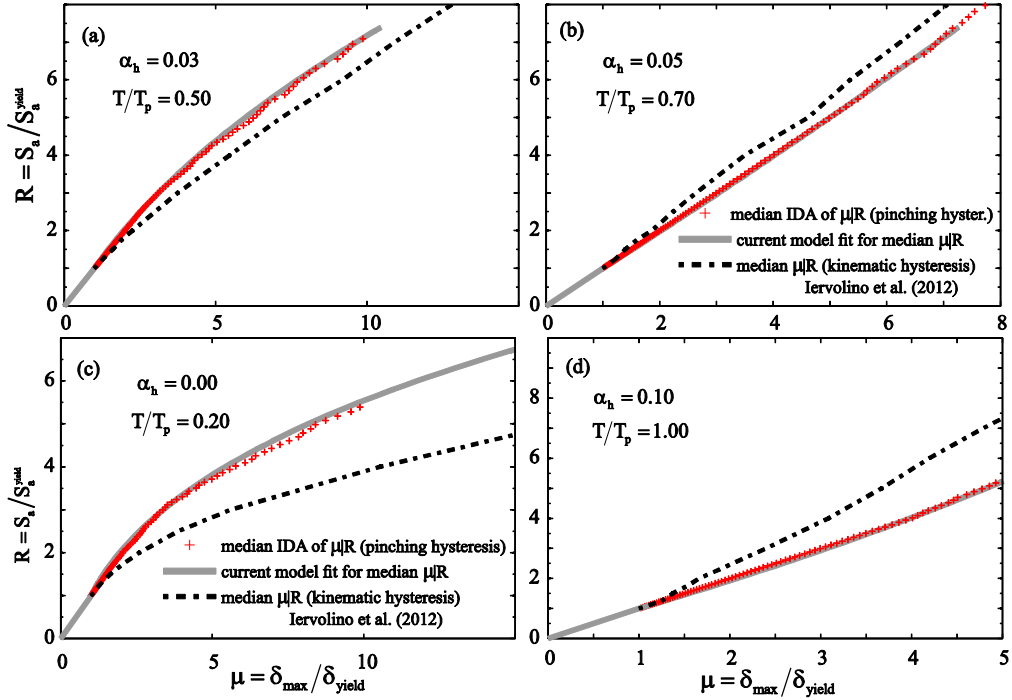


Figure 5.9. Comparison between median pulse-like ductility demand given reduction factor  $\mu_{50\%} |R$  obtained by in Chapter 2 (see also Iervolino et al., 2012) and the present study for bilinear oscillators with (a)  $\alpha_h = 0.03$  at  $T/T_p = 0.50$ , (b)  $\alpha_h = 0.05$  at  $T/T_p = 0.70$ , (c)  $\alpha_h = 0.0$  at  $T/T_p = 0.20$  and (d)  $\alpha_h = 0.10$  at  $T/T_p = 1.00$ .

Prior to drawing any conclusions from Figure 5.7, a brief reminder of the intrinsic differences among the two sets of inelastic responses is in order:

- The regression analysis behind Equation (2.5) used a dataset of 81 pulse-like NS ground motions while the present study used 130 (Table B.1 in the Appendix). Out of those records, 75 were common to both sets.
- SDOF responses calculated in Chapter 2, employed a kinematic hardening hysteretic rule, whilst the current study used moderately pinching hysteresis.
- While for the model of Equation (2.5) all available records at each  $T/T_p$  cross-section were used, this study imposed a  $T \geq 0.30s$  restriction, as previously discussed.
- Ductility demand in Chapter 2 was obtained at 15 R-values within the range  $R \in [1.25, 8.0]$ , while each IDA in this study is more finely sampled at 61 points per curve.

This being said, the most prominent differences can be observed in Figure 5.9(c) where the responses of an elastic-perfectly-plastic oscillator at  $T/T_p = 0.20$  are shown. This can be attributed to the explicit exclusion of some lower-period oscillator responses in this study, causing the ductility demands (and consequently the fitted model) to appear more benign at this particular  $T/T_p$  ratio.

Regarding the comparisons shown in the remaining panels of Figure 5.7, i.e. (a),(b) and (d) it should be said that these results are “isolated” from this low-period exclusion effect as almost no records are eliminated to bar the involvement of uncharacteristically low period oscillators when  $T/T_p \geq 0.50$ .

The main culprits for the observable differences, in these three cases, are sample size and different hysteretic rule adopted (kinematic hardening for the development of Equation 2.5 and moderately pinching for the present study). It is, however, not possible to partition said differences among the two causes. What should be mentioned, is that major differences in response between these two different types of hysteresis are mostly to be expected for systems which include a negative stiffness branch in their backbone curve, rather than the hardening bilinear systems involved in this comparison.

Overall, there is no observable trend of demand in one case consistently superseding the other across the entire parameter space. However, there does appear to be a tendency for the results of this study to display greater ductility demand given reduction factor in the higher  $T/T_p$  regions.

## 5.5.2 CURVE-FITTING VS. REGRESSION

In Chapter 2, non-linear regression analysis was employed to derive the predictive model for  $C_{R|pulse}$ . In this study, on the other hand, the term *least-squares curve fitting* was consistently (and consciously) used, whenever reference to model parameter estimation had to be made. This difference in methodology perhaps merits a brief commentary.

Inelastic responses in terms of ductility  $\mu$  or inelastic displacement ratio  $C_R$  are, so-called, cross-sectional data. This means that sample conditional means and variances can be calculated at any “cross-section”, i.e., given fixed values of  $R$ ,  $T/T_p$  (or all predictor variables in general). Least-squares regression analysis seeks to estimate

the parameters of the conditional expectation function (i.e., the model), by minimizing the sum of squared errors  $\sum_{i=1}^m \sum_{j=1}^n (\hat{y}_i - y_{ij})^2$ , where  $\hat{y}_i$  is the model prediction at the  $i$ -th cross-section and  $y_{ij}$  the  $j$ -th response of the  $i$ -th cross-section ( $m$  being the number of points one chooses to discretize the predictors such as  $R$ ,  $T/T_p$  and  $n$  being the number of ground motions considered, also termed “degrees of freedom” of the probabilistic model). In this case, the data  $y_{ij}$  must display constant variance (a property termed homoscedasticity) and identical distribution across all  $i$ . An equivalent way of stating this which is often encountered in the literature, is that the *residuals*  $\varepsilon_{ij} = \hat{y}_i - y_{ij}$  should follow zero-mean, identical distributions. In fact, the distributions must be Gaussian for least squares to provide the “best” estimate for the model parameters (identical Gaussian distributions automatically satisfy constant variance – see for example Bates and Watt, 1988).

On the other hand, if one first obtains the conditional sample means at each cross-

section as  $\bar{y}_i = \sum_{j=1}^n y_{ij} / n$ , one can attempt to *fit a parametric curve*  $\hat{y}$  to this sample

mean, by estimating the vector of parameters that minimizes the sum of squared errors  $\sum_{i=1}^m (\hat{y}_i - \bar{y}_i)^2$ . Such curve-fitting can also be suitable for sample fractiles, as

is the case with the data at hand, since on each fractile curve for each  $\mu$  value corresponds a single  $R$  value (and vice-versa).

Note that sometimes the term “error” is used in both cases of regression and curve-fitting. However, regression errors and curve-fitting errors are far from being the same thing. In regression analysis, the errors refer to the deviations of the dependent variable responses from the “true” model for the mean; naturally, these are not observable – one can only estimate the residuals, i.e., the deviations from the fitted model. In other words, regression residuals, or errors, are the stochastic perturbations of the random variable around its mean that constitute its distribution (Bates and Watt, 1988). Therefore, goodness-of-fit tests entail checking if the residuals are actually distributed as hypothesized. Curve fitting errors on the other hand, carry no information on the probabilistic distribution of the dependent variable; in this case increasing goodness-of-fit entails bringing the errors as close to zero as possible.

In the case of bilinear oscillators with hardening post-yield behavior, it is possible to define the conditional distribution of response ductility  $\mu$  for any value of the strength

reduction factor  $R$ . Therefore, performing regression analysis in order to develop a seismic demand model for such a system is feasible.

However, when systems with negative stiffness branches are examined, this is no longer the case. With increasing levels of reduction factor, some records will cause those systems to collapse. The occurrence of collapses, means that the expectation function in terms of a continuous EDP can no longer be defined and therefore regression is no longer an option. On the other hand, it is still possible to calculate the sample fractiles of EDP (see Shome and Cornell, 2000) and perform a curve-fit against those.

### 5.5.3 POTENTIAL APPLICATIONS

The present study dealt with the development of an analytical model that captures central tendency and dispersion of seismic demand and capacity for trilinear SDOF oscillators subjected to NS pulse-like ground motions. Despite the fact that the model provides output in the form of fractile IDA curves, these should not be employed to directly estimate the conditional distribution of  $EDP|IM$ . The reason behind this is the fact that the IDA curves refer to a given  $T/T_p$  ratio, rather than a specific structure.

Therefore, the model acts like an  $R-\mu-T/T_p$  relation, which must be combined with site-specific information on pulse period and likelihood of directivity. As such, it could be employed in a manner analogous to the methodology of Baltzopoulos et al. (2014) in order to render a static non-linear procedure, for example the capacity spectrum method (Fajfar, 1999), applicable in NS conditions.

It should also be mentioned in no uncertain terms that an analytical model as elaborate as this, is clearly intended exclusively for software implementation. In this light, it is conceivable that the goodness-of-fit for Equations (5.7) and (5.9) can be improved by replacing the linear models with non-parametric fits, which can be coded just as easily.

Another potential application of the model, can be its integration within an analysis tool such as SPO2IDA, which already provides seismic capacity and demand information for the case of ordinary ground motions. An integration of these two models (ordinary and pulse-like approximate IDAs) combined with NS hazard information at multiple stripes of IM level, should be able to simulate the results of multi-stripe dynamic analysis in NS conditions.

An illustrative example of this concept is presented in Figure 5.10. In the first panel, Figure 5.10(a), the median SPO2IDA “ordinary” prediction for a bilinear oscillator characterized by a  $T=1.0s$  period of natural vibration, post-yield hardening slope  $\alpha_h = 0.20$  and spectral acceleration at yield  $S_a^{yield} = 0.10g$  is compared against various median IDAs which incorporate pulse-like effects in both arbitrary and systematic fashion.

The median IDAs used for the comparison, consist of one curve obtained by running IDA for a set of randomly selected pulse-like ground motions (Table B.1), another obtained by means of Equation (5.6) for  $T/T_p = 0.40$  and a third curve obtained by integrating Equation (5.6) over various potential pulse periods from a site-specific

NS design scenario (to follow). A final comparison is made with an IDA curve that accounts for both the ordinary and pulse-like component of seismic demand at the site, each weighted by its respective likelihood.

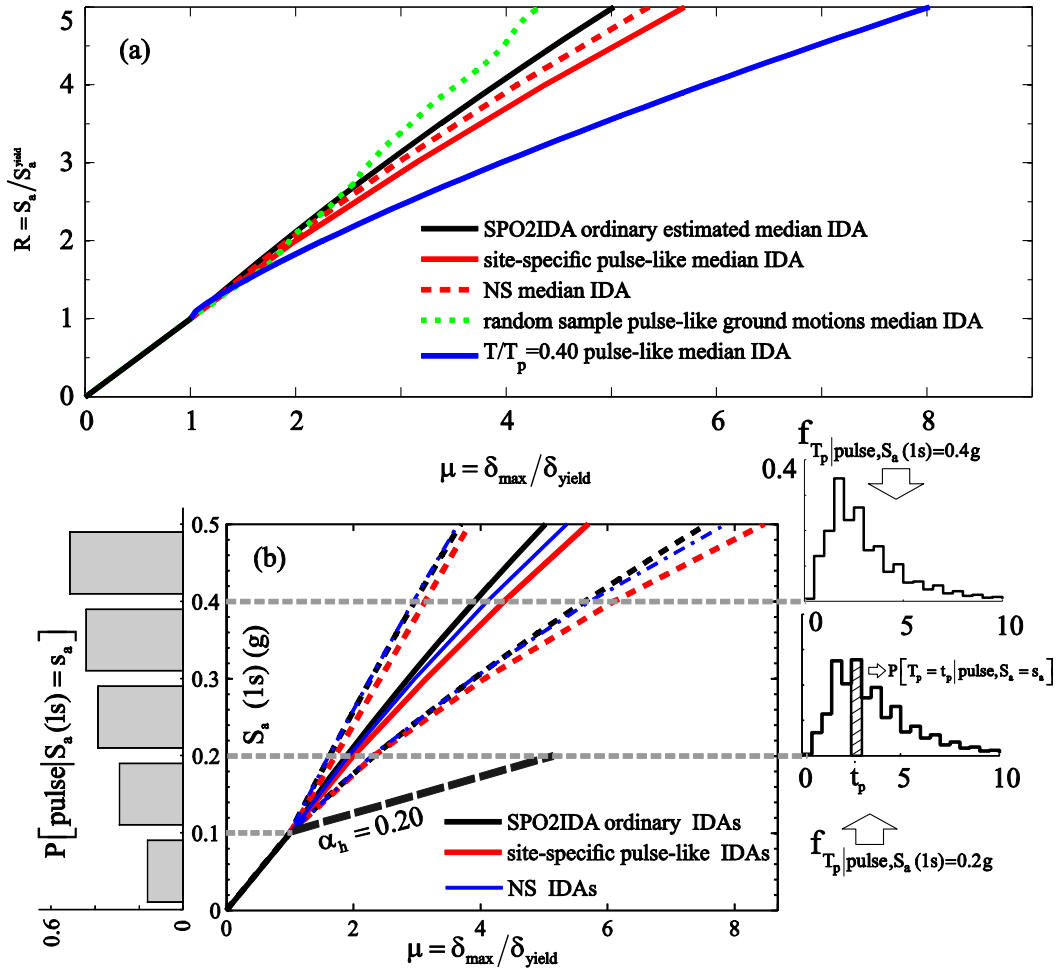


Figure 5.10. (a) Ordinary SPO2IDA median prediction for a bilinear oscillator with vibration period  $T=1.0s$ , post-yield hardening slope  $\alpha_h = 0.10$  and spectral acceleration at yield  $S_a^{yield} = 0.10g$  compared with curves incorporating pulse-like effects in both arbitrary and systematic fashion.

(b) Information obtained from site-specific NS hazard incorporated into the pulse-like IDA model to obtain site-specific IDA curves.

The NS scenario under consideration refers to a site being affected by a seismic source characterized by a nearly vertical strike-slip mechanism, with seismicity governed by an M7 characteristic earthquake model and maximum rupture area of

1330km<sup>2</sup>. The site is 5km distant from the horizontal projection of the assumed fault plane and therefore some directivity effects are to be expected.

NS hazard at the site expressed in terms of spectral acceleration at the oscillator's period was disaggregated for various values of  $S_a(1s) = s_a$  chosen to translate into reduction factors  $1 < R \leq 5$ . Thus, the conditional densities of pulse period  $f_{T_p | \text{pulse}, S_a(1s)=s_a}$  are obtained at each stripe of reduction factor.

This information is incorporated into Equation (5.6) by assuming that ductility given demand follows a lognormal distribution, leading to Equation (5.13), where the abbreviated notation  $P_{t_{p,i}}$  is used to indicate the conditional probability mass  $P[T_p = t_{p,i} | \text{pulse}, S_a(1s) = s_a]$ , resulting from discretizing  $f_{T_p | \text{pulse}, S_a(1s)=s_a}$  (see Figure 5.10b) in order to avoid integral notation when writing the law of conditional expectation.

$$E[\ln \mu | R, \text{pulse}] \approx \sum_i \ln \mu_{50\%}(R, T/t_{p,i}) \cdot P_{t_{p,i}} \quad (5.13)$$

Under the same assumption of log-normality, the law of conditional variance can be written as in Equation (5.14), where the notation  $\text{Var}[\cdot]$  indicates the second central moment (variance) operator. It should be mentioned that Equations (5.13) and (5.14) refer to expected value and variance of ductility demand given pulse occurrence; this condition has been omitted from terms showing dependence on  $T_p$  in order to maintain a more parsimonious notation. In the same spirit, the condition  $S_a(1s) = s_a$  which holds for all expected values and variances is replaced by strength reduction factor  $R$  in all following equations (for the specific structure, yield force is known).

$$\begin{aligned} \text{Var}[\ln \mu | R, \text{pulse}] &\approx \sum_i \text{Var}[\ln \mu | R, T/T_p] \cdot P_{t_{p,i}} + \\ &+ \sum_i \left[ E[\ln \mu | R, \text{pulse}] - \ln \mu_{50\%}(R, T/t_{p,i}) \right]^2 \cdot P_{t_{p,i}}, \text{ where} \quad (5.14) \\ \text{Var}[\ln \mu | R, T/T_p] &= 1/4 \cdot \left[ \ln \mu_{84\%}(R, T/t_{p,i}) - \ln \mu_{16\%}(R, T/t_{p,i}) \right]^2 \end{aligned}$$

This procedure and its end result (in terms of both mean and variance), are illustrated in the second panel, Figure 5.10(b). To the right of the IDA curves plot, the conditional densities of pulse period for two stripes of  $S_a(1s) = 0.2g$  and

$S_a(1s) = 0.4g$  are shown, while on the left of the vertical axis, the probabilities of pulse occurrence being causal of  $S_a(1s) = s_a$ ,  $P[\text{pulse}|S_a(1s) = s_a]$  are plotted, which are also the result of NS hazard disaggregation.

The final step of the procedure consists of accounting for both cases, i.e. occurrence of directivity pulse and absence thereof, in a single set of IDA curves. As already mentioned, the SPO2IDA prediction serves as an estimate of the ordinary component of seismic demand in this example. Applying the laws of conditional expectation and variance one more time, Equations (5.15) and (5.16) are obtained, where  $E[\ln \mu | R, \text{nopulse}]$  is the logarithm of the median SPO2IDA prediction and  $\text{Var}[\ln \mu | R, \text{nopulse}] = 1/4 \cdot [\ln \mu_{\text{SPO2IDA}, 84\%}(R) - \ln \mu_{\text{SPO2IDA}, 16\%}(R)]^2$ .

$$E[\ln \mu | R] = E[\ln \mu | R, \text{pulse}] \cdot P[\text{pulse} | R] + E[\ln \mu | R, \text{nopulse}] \cdot (1 - P[\text{pulse} | R]) \quad (5.15)$$

$$\begin{aligned} \text{Var}[\ln \mu | R] = & \text{Var}[\ln \mu | R, \text{pulse}] \cdot P[\text{pulse} | R] + \\ & + \text{Var}[\ln \mu | R, \text{nopulse}] \cdot (1 - P[\text{pulse} | R]) + \\ & + (E[\ln \mu | R, \text{pulse}] - E[\ln \mu | R])^2 \cdot P[\text{pulse} | R] + \\ & + (E[\ln \mu | R, \text{nopulse}] - E[\ln \mu | R])^2 \cdot (1 - P[\text{pulse} | R]) \end{aligned} \quad (5.16)$$

These results lead to the curves labeled “NS IDAs” in Figure 5.10(b).

Overall, it can be observed that the assumption of a specific pulse period being considered representative across all scale factors of the IDA can lead to overestimation of NS seismic demand, when said pulse period corresponds to a fraction of structural period associated with aggressive NS FD ground motions.

On the other hand, a random sample of pulse-like ground motions, where  $T_p$  is not accounted for explicitly, can result in demand which is even less than the ordinary estimate (albeit said ordinary estimate corresponds to an analytical model).

Finally, consideration of  $T_p$  in manner consistent with NS hazard, can result in seismic demand which supersedes the ordinary estimate, when site-to-source geometry renders the site prone to FD effects. In this example, the NS median seismic demand represented by the corresponding IDA curve shows a trend of increasing detachment from the ordinary curve as  $S_a$  levels increase.

## CHAPTER 5 REFERENCES

Baker JW. Identification of near-fault velocity and prediction of resulting response spectra. *Proc Geotech Earthq Eng and Struct Dyn IV* 2008; Sacramento, CA.

Baltzopoulos G, Chioccarelli E, Iervolino I. The displacement coefficient method in near-source conditions. *Earthquake Engng Struct. Dyn* 2014; DOI: 10.1002/eqe.2497.

Bates DM, Watt DG. *Nonlinear Regression Analysis and its Applications*, John Wiley & Sons Inc, 1988.

Benjamin JR, Cornell CA. *Probability Statistics and Decision for Civil Engineers*. McGraw-Hill: New York, 1970.

Champion C, Liel A. The effect of near-fault directivity on building seismic collapse risk. *Earthquake Engng Struct Dyn* 2012; **41**: 1391-1409.

Fajfar P. Capacity spectrum method based on inelastic spectra. *Earthquake Engng Struct. Dyn* 1999; **28**, 979-993.

Ibarra LF, Krawinkler H. *Global Collapse of Frame Structures under Seismic Excitations*. Report No.152, The John A. Blume Earthquake Engineering Center, Dpt. of Civil and Environmental Engineering, Stanford University, Stanford CA, 2005.

Iervolino I, Chioccarelli E, Baltzopoulos G. Inelastic Displacement Ratio of Near-Source Pulse-like Ground Motions. *Earthquake Engng Struct Dyn* 2012; **41**: 2351-2357.

Krawinkler H, Miranda E. Performance-Based Earthquake Engineering, In: *Earthquake Engineering: From Engineering Seismology to Performance-Based Engineering*, eds. Bozorgina Y, Bertero VV, CRC Press, FL, 2004.

Luco N, Cornell CA. Structure-specific scalar intensity measures for near-source and ordinary earthquake ground motions. *Earthquake Spectra* 2007; **23**(2):357–92.

Rahnama M, Krawinkler H. *Effects of soft soils and hysteresis model on seismic demands*. Report No. 108, The John A. Blume Earthquake Engineering Center, Stanford University, Stanford CA, 1993.

Shome N, Cornell CA. Structural seismic demand analysis: Consideration of collapse. *Proceedings of the 8th ASCE Specialty Conference on Probabilistic Mechanics and Structural Reliability*, paper 119. Notre Dame 2000; 1–6.

Tothong P, Cornell CA. Structural performance assessment under near-source pulse-like ground motions using advanced ground motion intensity measures. *Earthquake Engng Struct Dyn* 2008; **37**(7): 1013-1037.

Vamvatsikos D, Cornell CA. Incremental dynamic analysis. *Earthquake Engng Struct. Dyn* 2002; **31**, 491-514.

Vamvatsikos D, Cornell CA. Applied incremental dynamic analysis. *Earthquake Spectra* 2004; **20**(2):523–553.

Vamvatsikos D, Cornell CA. Direct estimation of the seismic demand and capacity of MDOF systems through incremental dynamic analysis of an SDOF approximation. *Journal of Structural Engineering (ASCE)* 2005; **131**(4):589–599.

Vamvatsikos D, Cornell CA. Direct estimation of the seismic demand and capacity of oscillators with multi-linear static pushovers through IDA. *Earthquake Engng Struct. Dyn* 2006; **35**, 1097-1117.



# Chapter 6

## Summary and Conclusions

This thesis dealt with the issue of seismic structural performance evaluation in near-source conditions, where inelastic response estimates should account for potential forward directivity effects.

In Chapter 2 the functional form for prediction of near-source pulse-like inelastic displacement ratio, was investigated. It was found that an additional term is necessary with respect to analogous equations used to fit trends from ordinary ground motions and also that  $T/T_p$  should be included among the predictors. An asymmetric-bell term, centered at different points depending on  $R$ , was suitable to fit  $C_R$  in the low  $T/T_p$  range. This resulted in two opposite bumps in two different spectral regions, and builds up consistent with recent literature on the same topic and on what observed for soft soil site records, which are also characterized by a predominant period.

Parameters for this relationship were determined in a two-step nonlinear regression, for a range of strength reduction factors, using a previously identified set of fault normal pulse-like records. Finally, standard deviation of residual data was also fitted by an analytical equation as a function of the  $T/T_p$  ratio. These results were used in Chapter 3, where design procedures specific for near-source conditions are developed.

Chapter 3 discussed the adaptation of the Displacement Coefficient Method to estimate the design demand for structures in near-source conditions. The modifications required to adapt the DCM were discussed both in terms of elastic and inelastic demand. An investigation in the form of illustrative applications was presented, involving a variety of single-fault NS design scenarios. In this context, the NS-DCM was implemented for modern-code-conforming R/C frames, and compared to design for classical hazard and inelastic demand.

The results of the pushover-based DCM, were compared to results obtained from dynamic RHA, which was performed using suites of ground motions carefully selected in order to reflect NS demand for the corresponding design scenarios.

The DCM results for the NS design scenarios, indicated that FD could induce appreciable increase in displacement demand; increments in estimated target displacements due to NS-FD effects were in the range of 34%-77% for the scenario most prone to directivity amongst those examined and 8%-27% for the case least affected by FD effects among those considered. This behaviour was further confirmed by the dynamic RHA results.

Another important finding was the fact that the extent to which NS inelastic demand exceeds ordinary demand, as computed without accounting for directivity effects, increases when longer return period performance levels are considered. Furthermore, it was shown that this discrepancy may be exacerbated at sites whose orientation with respect to the fault renders them particularly prone to FD ground motions.

It was also observed that, depending on the distribution of causal event magnitudes most likely to characterize a given source, potential directivity may be manifest by means of relatively short duration pulses, comparable with the periods of natural vibration of typical building structures. This type of impulsive records would mostly affect the elastic response of such structures and therefore, the key step towards estimating NS inelastic response becomes computing design spectra by means of NS-PSHA.

However, it was also shown that there are cases where NS effects have small-to-negligible influence on seismic hazard (expressed in elastic response IMs) around a specific spectral region, and yet produce more pronounced increase in average inelastic demand for structures with vibration periods that spectral region. The non-linear dynamic analyses carried out also corroborate this finding. It was demonstrated that this effect can be explicitly accounted for in structural analysis by use of NS hazard disaggregation results, which provide additional information with respect to the design spectrum.

In Chapter 4, near-source ground motions from recent seismic events, were investigated for signs of directivity and impulsive characteristics, using both well-established as well as more recent procedures of pulse identification. Ground motions identified as pulse-like were further examined under the light of relevant publications, so as to discern those pulses most likely caused by directivity effects rather than other unrelated phenomena. This resulted in the compilation of a database comprising one-hundred and thirty near-source pulse-like ground motions, which were employed in subsequent research, presented in Chapter 5.

Chapter 5 saw the use of IDA to investigate the response of oscillators with trilinear backbone curves to NS pulse-like ground motions. To this end, an analytical model was developed for the prediction of pulse-like IDA curves. This model also makes the important inclusion of pulse period as a predictor variable.

In the illustrative application of the model which was provided, it was observed that the assumption of a specific “aggressive” pulse period being considered representative across all scale factors of the IDA can lead to overestimation of NS seismic demand.

On the other hand, a random sample of pulse-like ground motions, where  $T_p$  is not accounted for explicitly, can result in a distorted estimate of NS seismic demand. Finally, consideration of  $T_p$  in manner consistent with NS hazard, can result in seismic demand which supersedes the ordinary estimate, when site-to-source geometry renders the site prone to FD effects. In the example application provided, the NS median seismic demand showed a trend of increasing separation from the ordinary curve, towards higher ductility demands, with increasing  $S_a$  levels.



## **APPENDIX A**

*Ground motion records and response history analysis results - Chapter 3.*

Table A.1: Set of ordinary ground motion records used for the RHA of the 5- and 6-storey frames and results for maximum roof displacement.

No	Earthquake Name	Station Name	Year	M	Mech.	R <sub>JB</sub> km	ClstD km	V <sub>s,30</sub> m/s	PGV cm/s	SF 0.75s	SF 1.00s	u <sub>roof,max</sub> 5st. mm	u <sub>roof,max</sub> 6st. mm
1	Borrego Mountain	San Onofre - So Cal Edison	1968	6.6	S-S	129	129	443	3.7	3.602	3.022	37	49
2	Cape Mendocino	Fortuna - Fortuna Blvd	1992	7.0	R	16	20	457	24.7	0.975	0.907	45	54
3	Chi-Chi, Taiwan	CHY090	1999	7.6	R-O	58	58	215	17.0	1.339	1.154	62	57
4	Chi-Chi, Taiwan	CHY104	1999	7.6	R-O	18	18	223	54.9	0.324	0.544	43	60
5	Chi-Chi, Taiwan	HWA049	1999	7.6	R-O	47	51	273	22.4	0.666	0.710	30	41
6	Chi-Chi, Taiwan	ILA010	1999	7.6	R-O	78	80	474	8.3	1.683	2.812	40	46
7	Chi-Chi, Taiwan	ILA067	1999	7.6	R-O	33	39	553	14.3	0.680	0.643	26	35
8	Chi-Chi, Taiwan	TCU085	1999	7.6	R-O	55	58	1000	7.5	2.787	2.869	32	38
9	Chi-Chi, Taiwan	TTN033	1999	7.6	R-O	56	59	273	6.7	2.323	2.205	73	62
10	Chi-Chi, Taiwan	WNT	1999	7.6	R-O	2	2	664	55.4	0.295	0.317	33	52
11	Chi-Chi, Taiwan-04	CHY035	1999	6.2	S-S	25	25	474	12.3	1.328	0.629	23	48
12	Hector Mine	Little Rock Post Office	1999	7.1	S-S	147	147	442	4.6	1.705	2.361	27	37
13	Hector Mine	Valyermo Forest Fire Station	1999	7.1	S-S	136	136	345	6.2	2.675	3.921	28	60
14	Hector Mine	Wrightwood - Nielson Ranch	1999	7.1	S-S	113	113	345	5.4	2.776	6.346	31	65
15	Kocaeli, Turkey	Tekirdag	1999	7.5	S-S	164	165	660	3.8	2.460	3.161	29	48
16	Landers	Baker Fire Station	1992	7.3	S-S	88	88	271	9.7	1.990	1.522	39	67
17	Landers	La Crescenta - New York	1992	7.3	S-S	148	148	446	3.6	3.557	2.218	62	57
18	Loma Prieta	Bear Valley #10, Webb Res.	1989	6.9	R-O	67	68	304	8.5	1.720	1.850	36	64
19	Northridge-01	West Covina - S Orange Ave	1994	6.7	R	51	52	309	5.8	2.390	1.788	34	43
20	Tabas, Iran	Dayhook	1978	7.4	R	0	14	660	28.2	0.511	0.489	46	47

R<sub>JB</sub>: Closest distance to horizontal projection of the fault plane.

ClstD: Closest distance to the fault plane.

Rupture mechanisms S-S: Strike-Slip, R: Reverse, R-O: Reverse-Oblique

PGV: Peak Ground Velocity

SF: Scale Factor

Table A.2: Set of pulse-like ground motion records used for the RHA of the 5- and 6-storey frames and results for maximum roof displacement.

No	Earthquake Name	Station Name	Year	M	Mech.	R <sub>JB</sub> km	ClstD km	V <sub>s,30</sub> m/s	PGV cm/s	T <sub>p</sub> s	SF 0.75s	SF 1.00s	U <sub>roof,max</sub> 5st. mm	U <sub>roof,max</sub> 6st. mm
1	Coyote Lake	Coyote Lake Dam (SW Abut)	1979	5.7	S-S	5.3	6.1	597	19.8	0.56	0.809	-	47	-
2	San Fernando	Pacoima Dam (up. left abut)	1971	6.6	R	0.0	1.8	2016	116.5	1.60	0.212	-	62	-
3	Northridge-01	LA Dam	1994	6.7	R	0.0	5.9	629	77.1	1.65	0.225	0.205	55	69
4	Loma Prieta	Gilroy Array #2	1989	6.9	R-O	10.4	11.1	271	45.7	1.72	0.321	0.357	49	67
5	Imperial Valley-06	Agrarias	1979	6.5	S-S	0.0	0.7	275	54.4	2.30	0.533	0.494	41	76
6	Northridge-01	Newhall - W Pico Canyon Rd.	1994	6.7	R	2.1	5.5	286	87.8	2.41	0.290	0.203	81	78
7	Northridge-01	Sylmar - Olive View Med FF	1994	6.7	R	1.7	5.3	441	122.7	3.11	0.277	-	49	-
8	Cape Mendocino	Fortuna - Fortuna Blvd	1992	7.0	R	16.0	20.0	457	22.3	3.14	0.942	-	43	-
9	Imperial Valley-06	EC Meloland Overpass FF	1979	6.5	S-S	0.1	0.1	186	115.0	3.35	0.554	0.315	149	94
10	Northridge-01	Sylmar - Converter Sta	1994	6.7	R	0.0	5.4	251	130.3	3.48	-	0.121	-	62
11	Northridge-01	Sylmar - Converter Sta East	1994	6.7	R	0.0	5.2	371	116.6	3.49	-	0.229	-	61
12	Westmorland	Parachute Test Site	1981	5.9	S-S	16.5	16.7	349	35.8	3.58	0.645	-	58	-
13	Imperial Valley-06	El Centro Array #6	1979	6.5	S-S	0.0	1.4	203	111.9	3.84	-	0.389	-	82
14	Imperial Valley-06	Brawley Airport	1979	6.5	S-S	8.5	10.4	209	36.1	4.03	1.785	0.785	146	78
15	Imperial Valley-06	El Centro Array #5	1979	6.5	S-S	1.8	4.0	206	91.5	4.05	0.404	-	65	-
16	Imperial Valley-06	El Centro Array #10	1979	6.5	S-S	6.2	6.2	203	46.9	4.49	1.576	0.898	195	127*
17	Imperial Valley-06	El Centro Array #4	1979	6.5	S-S	4.9	7.1	209	77.9	4.61	-	0.335	-	73
18	Landers	Lucerne	1992	7.3	S-S	2.2	2.2	685	140.3	5.10	0.327	0.384	49	102*
19	Imperial Valley-06	El Centro Array #3	1979	6.5	S-S	10.8	12.9	163	41.1	5.24	-	1.321	-	89
20	Imperial Valley-06	El Centro Array #8	1979	6.5	S-S	3.9	3.9	206	48.6	5.39	0.551	-	40	-
21	Kocaeli, Turkey	Gebze	1999	7.5	S-S	7.6	10.9	792	52.0	5.87	0.905	0.752	62	79
22	Chi-Chi, Taiwan	TCU101	1999	7.6	R-O	2.0	2.0	273	61.5	6.00	-	0.552	-	91
23	Northridge-01	Lake Hughes #9	1994	6.7	R	24.9	25.4	671	7.3	6.33	4.309	5.287	55	69
24	Imperial Valley-06	El Centro Array #11	1979	6.5	S-S	12.5	12.5	196	41.1	7.36	-	0.783	-	101
25	Darfield, N. Zealand	Templeton School (TPLC)	2010	7.0	S-S	6.0	6.0	250	64.4	8.93	0.920	-	71	-
26	Chi-Chi, Taiwan	TCU128	1999	7.6	R-O	13.0	13.0	600	71.0	9.01	-	0.646	-	92
27	Duzce, Turkey	Lamont 1060	1999	7.1	S-S	25.8	25.9	782	11.3	9.63	6.217	4.191	50	78
28	Chi-Chi, Taiwan	TCU051	1999	7.6	R-O	8.0	8.0	273	41.2	10.39	0.754	-	72	-
29	Chi-Chi, Taiwan	TCU087	1999	7.6	R-O	7.0	7.0	474	41.3	10.40	-	1.093	-	70

\* Record caused collapse of the structure; reported roof displacement corresponds to the maximum reliable value from the analysis (maximum roof displacement attained prior to the onset of dynamic instability).

## APPENDIX B

*Dataset of pulse-like near-source ground motions - Chapter 4.*

Table B.1: Complete dataset of pulse-like ground motion records

Earthquake Name	Station Name	Year	M	F. Mech.	R <sub>epi</sub> km	R <sub>JB</sub> km	Clst D km	EN-1998 Site class	PGA g	PGV cm/s	T <sub>p</sub> s	$\epsilon_{PGV}$	$\epsilon_{Sa(Tp)}$	Azi-muth deg.	FN Pulse
Drama	Drama	1985	5.2	N-O	15.6	11.6	11.6	C	0.06	4.5	1.12	0.63	0.90	145	Yes
San Fernando	LA - Hollywood Stor FF	1971	6.6	R	39.5	22.8	22.8	C	0.17	17.6	4.91	0.41	1.10	195	Yes
San Fernando	Lake Hughes #1	1971	6.6	R	26.1	22.2	27.4	B	0.15	18.3	1.15	0.75	1.45	200	Yes
San Fernando	Lake Hughes #4	1971	6.6	R	24.2	19.5	25.1	B	0.15	8.4	1.05	-0.44	0.04	200	Yes
San Fernando	Pacoima Dam (upper left abut)	1971	6.6	R	11.9	0.0	1.8	A	1.43	116.5	1.60	3.02	3.21	195	Yes
Landers	Lucerne	1992	7.3	S-S	44.0	2.2	2.2	A	0.71	140.3	5.10	2.46	2.26	239	Yes
Landers	Yermo Fire Station	1992	7.3	S-S	86.0	23.6	23.6	C	0.22	53.2	7.50	1.51	1.60	225	Yes
Irpinia	Bagnoli Irpinio	1980	6.9	N	22.7	8.1	8.2	B	0.19	29.3	1.76	1.17	1.60	223	Yes
Irpinia	Sturmo (STN)	1980	6.9	N	30.4	6.8	10.8	B	0.31	61.6	3.09	1.79	2.00	223	Yes
Coyote Lake	Coyote Lake Dam - SW Abut.	1979	5.7	S-S	8.0	5.3	6.1	B	0.24	21.3	0.56	1.25	1.85	246	Yes
Coyote Lake	Gilroy Array #6	1979	5.7	S-S	4.4	0.4	3.1	B	0.37	35.8	1.21	1.23	1.69	246	Yes
Coyote Lake	SJB Overpass, Bent 3 g.l.	1979	5.7	S-S	23.9	20.4	20.7	B	0.10	5.0	0.83	-0.06	0.73	246	Yes
Coyote Lake	San J. Bautista - Hwy 101/156	1979	5.7	S-S	23.9	20.4	20.7	B	0.08	4.9	0.81	-0.10	0.65	246	Yes
Mammoth Lakes	Convict Creek	1980	5.7	S-S	8.6	2.9	9.5	B	0.18	13.2	1.55	-0.55	-0.03	360	Yes
San Salvador	Geotech Investig Center	1986	5.8	S-S	7.9	2.1	6.3	B	0.51	67.8	0.86	2.23	1.51	302	Yes
San Salvador	National Geografical Inst	1986	5.8	S-S	9.5	3.7	7.0	B	0.61	92.2	1.13	3.11	2.95	231	No
Kobe, Japan	Takatori	1995	6.9	S-S	13.1	1.5	1.5	C	0.68	169.6	1.62	1.86	1.92	140	Yes
Kobe, Japan	Takarazuka	1995	6.9	S-S	38.6	0.0	0.3	C	0.65	72.6	1.43	0.03	0.35	140	Yes
Kobe, Japan	KJMA	1995	6.9	S-S	18.3	0.9	1.0	C	0.86	105.7	1.09	0.76	1.41	318	Yes
Santa Barbara	Santa Barbara Courthouse	1978	5.9	R-O	3.2	0.0	12.2	B	0.21	15.8	2.28	-0.89	-0.14	205	Yes
Westmorland	Parachute Test Site	1981	5.9	S-S	20.5	16.5	16.7	C	0.17	35.8	3.58	2.70	3.25	334	Yes
Whittier Narrows	Bell Gardens - Jaboneria	1987	6.0	R-O	11.8	10.3	17.8	C	0.20	16.1	0.73	0.19	0.97	190	Yes
Whittier Narrows	Compton - Castlegate St	1987	6.0	R-O	19.8	18.3	23.4	C	0.32	27.0	0.78	1.78	2.15	190	Yes
Whittier Narrows	Downey - Co Maint Bldg	1987	6.0	R-O	16.0	15.0	20.8	C	0.19	28.0	0.79	1.63	1.85	190	Yes

*(continues on next page)*

Earthquake Name	Station Name	Year	M	Fault Mech.	R <sub>epi</sub> km	R <sub>JB</sub> km	Clst D km	EN-1998 Site class	PGA g	PGV cm/s	T <sub>p</sub> s	ε <sub>PGV</sub>	ε <sub>Sa(Tp)</sub>	Azi-muth deg.	FN Pulse
Whittier Narrows	Glendale - Las Palmas	1987	6.0	R-O	21.7	14.7	22.8	B	0.29	16.8	0.59	1.01	1.33	190	Yes
Whittier Narrows	LA - W 70th St	1987	6.0	R-O	20.9	16.8	22.2	C	0.17	16.1	0.90	0.64	1.25	190	Yes
Whittier Narrows	LB - Orange Ave	1987	6.0	R-O	20.7	19.8	24.5	C	0.23	31.5	0.95	2.44	2.69	190	Yes
Whittier Narrows	LB - Rancho Los Cerritos	1987	6.0	R-O	25.5	24.6	28.6	C	0.16	20.1	0.92	1.79	2.00	190	Yes
Whittier Narrows	Lakewood - Del Amo Blvd	1987	6.0	R-O	22.7	22.4	26.7	C	0.29	32.1	0.95	2.32	2.30	190	Yes
Whittier Narrows	Norwalk - Imp Hwy, S Grnd	1987	6.0	R-O	15.0	14.4	20.4	C	0.25	27.5	0.83	1.57	1.43	190	Yes
Whittier Narrows	Santa Fe Springs - E.Joslin	1987	6.0	R-O	11.7	11.5	18.5	C	0.42	46.0	0.76	2.40	2.17	190	Yes
N. Palm Springs	North Palm Springs	1986	6.1	R-O	10.6	0.0	4.0	C	0.67	58.3	1.38	0.76	1.05	197	Yes
Morgan Hill	Coyote Lake Dam - SW Abut.	1984	6.2	S-S	24.6	0.2	0.5	B	1.03	68.7	0.95	1.40	1.83	58	Yes
Morgan Hill	Gilroy Array #6	1984	6.2	S-S	36.3	9.9	9.9	B	0.33	27.2	1.24	1.67	1.99	58	Yes
Superstition Hills	Parachute Test Site	1987	6.5	S-S	16.0	1.0	1.0	C	0.45	141.0	2.28	1.91	1.78	37	Yes
Erzican	Erzincan	1992	6.7	S-S	9.0	0.0	4.4	C	0.46	68.7	2.65	0.28	0.57	32	Yes
Kocaeli	Arcelik	1999	7.5	S-S	53.7	10.6	13.5	B	0.21	11.9	10.9	-1.90	0.02	184	Yes
Kocaeli	Gebze	1999	7.5	S-S	47.0	7.6	10.9	B	0.27	43.6	5.87	0.49	1.05	184	Yes
Kocaeli	Yarimca	1999	7.5	S-S	19.3	1.4	4.8	C	0.28	90.6	4.95	-0.12	0.46	25	Yes
Duzce	Bolu	1999	7.1	S-S	41.3	12.0	12.0	C	0.82	65.8	0.88	1.27	1.94	88	Yes
Duzce	Lamont 1060	1999	7.1	S-S	44.4	25.8	25.9	B	0.03	9.5	9.63	-0.35	1.10	173	No
Cape Mendocino	Petrolia	1992	7.0	R	4.5	0.0	8.2	B	0.70	94.5	3.00	0.58	0.64	260	Yes
Cape Mendocino	Fortuna - Fortuna Blvd	1992	7.0	R	29.6	16.0	20.0	B	0.10	20.3	3.14	-0.02	1.61	260	Yes
Loma Prieta	Gilroy Array #2	1989	6.9	R-O	29.8	10.4	11.1	C	0.41	45.7	1.72	0.70	1.26	38	Yes
Loma Prieta	Saratoga - Aloha Ave	1989	6.9	R-O	27.2	7.6	8.5	B	0.45	42.8	4.47	0.47	0.24	38	Yes
Loma Prieta	Gilroy - Historic Bldg.	1989	6.9	R-O	28.1	10.3	11.0	C	0.27	43.6	1.64	0.62	0.91	147	Yes
Northridge	Jensen Filter Plant Admin Bld	1994	6.7	R	13.0	0.0	5.4	B	0.41	112.9	3.16	1.16	1.82	32	No
Northridge	Jensen Filter Plant Gen Bld	1994	6.7	R	13.0	0.0	5.4	B	0.61	83.1	3.53	0.91	1.74	32	Yes
Northridge	LA Dam	1994	6.7	R	11.8	0.0	5.9	B	0.34	66.4	1.65	0.67	0.84	32	Yes
Northridge	Newhall - W Pico Canyon Rd.	1994	6.7	R	21.6	2.1	5.5	C	0.41	114.0	2.41	1.32	1.35	32	Yes
Northridge	Pacoima Dam (downstr)	1994	6.7	R	20.4	4.9	7.0	A	0.31	23.0	0.50	0.91	1.20	32	Yes
Northridge	Pacoima Dam (upper left)	1994	6.7	R	20.4	4.9	7.0	A	1.22	92.9	0.90	3.40	3.34	32	Yes
Northridge	Rinaldi Receiving Sta	1994	6.7	R	10.9	0.0	6.5	C	0.81	135.4	1.23	1.38	1.22	32	Yes
Northridge	Sylmar - Converter Sta	1994	6.7	R	13.1	0.0	5.4	C	0.64	95.2	3.48	0.92	1.62	32	Yes

*(continues on next page)*

Earthquake Name	Station Name	Year	M	Fault Mech.	R <sub>epi</sub> km	R <sub>JB</sub> km	Clst D km	EN-1998 Site class	PGA g	PGV cm/s	T <sub>p</sub> s	ε <sub>PGV</sub>	ε <sub>Sa(Tp)</sub>	Azi-muth deg.	FN Pulse
Northridge	Sylmar - Converter Sta East	1994	6.7	R	13.6	0.0	5.2	B	0.84	116.6	3.49	1.21	1.45	32	Yes
Northridge	Sylmar - Olive View Med FF	1994	6.7	R	16.8	1.7	5.3	B	0.73	98.9	3.11	1.28	0.73	32	Yes
Northridge	Newhall - Fire Station	1994	6.7	R	20.3	3.2	5.9	C	0.70	116.0	1.37	1.63	1.43	21	Yes
Northridge	LA - Sepulveda VA Hospital	1994	6.7	R	8.5	0.0	8.4	B	0.75	77.8	0.93	0.51	1.00	271	Yes
Northridge	Pacoima Kagel Canyon	1994	6.7	R	19.3	5.3	7.3	B	0.53	56.8	0.73	1.17	1.52	33	No
Imperial Valley	Aeropuerto Mexicali	1979	6.5	S-S	2.5	0.0	0.3	C	0.27	40.7	2.42	-0.33	-0.13	233	Yes
Imperial Valley	Agrarias	1979	6.5	S-S	2.6	0.0	0.7	C	0.31	54.4	2.30	0.29	0.32	233	Yes
Imperial Valley	Brawley Airport	1979	6.5	S-S	43.2	8.5	10.4	C	0.16	39.4	4.03	0.88	1.16	233	Yes
Imperial Valley	EC County Center FF	1979	6.5	S-S	29.1	7.3	7.3	C	0.24	56.0	4.52	1.40	0.99	233	Yes
Imperial Valley	El Centro Array #10	1979	6.5	S-S	28.8	8.6	8.6	C	0.17	51.0	4.49	1.35	1.54	233	Yes
Imperial Valley	El Centro Array #11	1979	6.5	S-S	29.5	12.6	12.6	C	0.39	45.6	7.36	1.45	1.76	233	Yes
Imperial Valley	El Centro Array #3	1979	6.5	S-S	28.7	10.8	12.9	D	0.21	42.4	5.24	1.08	1.33	233	Yes
Imperial Valley	El Centro Array #4	1979	6.5	S-S	27.1	4.9	7.1	C	0.37	82.3	4.61	1.78	2.27	233	Yes
Imperial Valley	El Centro Array #5	1979	6.5	S-S	27.8	1.8	4.0	C	0.38	96.2	4.05	1.62	2.07	233	Yes
Imperial Valley	El Centro Array #6	1979	6.5	S-S	27.5	0.0	1.4	C	0.45	111.1	3.84	1.80	2.19	233	Yes
Imperial Valley	El Centro Array #7	1979	6.5	S-S	27.6	0.6	0.6	C	0.47	113.4	4.23	1.79	1.77	233	Yes
Imperial Valley	El Centro Array #8	1979	6.5	S-S	28.1	3.9	3.9	C	0.45	52.3	5.39	0.83	1.48	233	Yes
Imperial Valley	El Centro Differential Array	1979	6.5	S-S	27.2	5.1	5.1	C	0.41	62.6	5.86	1.33	1.17	233	Yes
Imperial Valley	Holtville Post Office	1979	6.5	S-S	19.8	5.4	7.5	C	0.25	47.1	4.80	0.86	1.36	233	Yes
Imperial Valley	El Centro - Meloland	1979	6.5	S-S	19.4	0.1	0.1	C	0.21	40.7	3.35	-0.36	0.82	233	Yes
L'Aquila	Gran Sasso (Assergi)	2009	6.3	N	14.0	6.4	6.4	B	0.19	7.5	3.13	-0.88	-1.10	52	Yes
L'Aquila	Lab. Gran Sasso	2009	6.3	N	18.8	11.1	11.2	B	0.02	2.2	4.03	-2.28	-1.23	52	Yes
L'Aquila	V. Aterno Centro Valle	2009	6.3	N	4.4	0.0	6.3	B	0.53	34.2	1.06	0.58	0.69	110	No
L'Aquila	V. Aterno Colle Grilli	2009	6.3	N	4.5	0.0	6.8	B	0.41	32.6	1.02	0.84	1.27	52	Yes
L'Aquila	V. Aterno F. Aterno	2009	6.3	N	4.6	0.0	6.6	B	0.43	25.6	0.74	0.21	0.11	52	Yes
L'Aquila	L'Aquila - Parking	2009	6.3	N	1.8	0.0	5.4	B	0.27	18.1	1.99	-0.17	0.53	52	Yes
L'Aquila	Ortucchio	2009	6.3	N	48.8	35.1	37.2	B	0.04	3.7	0.83	-0.28	0.21	52	Yes
L'Aquila	AQU	2009	6.3	N	6.3	-	-	B	0.31	17.2	1.02	-0.59	-1.09	52	Yes
Tabas	Tabas	1978	7.4	R	55.2	1.8	2.1	B	0.80	129.7	6.19	1.45	2.23	0	No

(continues on next page)

Earthquake Name	Station Name	Year	M	Fault Mech.	R <sub>epi</sub> km	R <sub>JB</sub> km	Clst D km	EN-1998 Site class	PGA g	PGV cm/s	T <sub>p</sub> s	ε <sub>PGV</sub>	ε <sub>Sa(Tp)</sub>	Azi-muth deg.	FN Pulse
Denali	TAPS Pump Station #10	2002	7.9	S-S	84.4	0.2	2.7	C	0.33	121.5	3.16	0.00	-0.12	56	Yes
Kalamata	Kalamata (bsmt) (2 <sup>nd</sup> tr.)	1986	5.4	N	7.1	4.0	5.6	B	0.27	27.0	0.79	2.29	2.38	75	Yes
El Mayor	El Centro Array #12	2010	7.2	S-S	58.0	10.0	11.3	C	0.41	72.6	8.72	1.26	1.95	83	No
Christchurch	Pages Road Pumping Station	2011	6.2	R-O	4.9	1.9	2.0	C	0.75	123.1	4.82	2.36	2.79	135	Yes
Christchurch	Christchurch Resthaven	2011	6.2	R-O	7.6	5.1	5.1	D	0.73	97.5	1.55	2.17	2.43	71	No
Darfield	CBGS	2010	7.0	S-S	47.0	18.1	18.1	C	0.20	60.0	12.6	1.59	1.70	346	Yes
Darfield	DSLCL	2010	7.0	S-S	13.4	5.3	8.5	C	0.24	65.9	7.83	0.60	1.76	44	No
Darfield	LINC	2010	7.0	S-S	33.8	5.1	7.1	C	0.45	116.4	7.37	1.67	1.45	359	Yes
Darfield	LPCC	2010	7.0	S-S	54.3	25.2	25.7	B	0.33	30.2	10.6	1.65	1.80	358	Yes
Darfield	NNBS	2010	7.0	S-S	55.5	26.8	26.8	C	0.20	56.5	8.04	1.84	1.67	154	Yes
Darfield	ROLCL	2010	7.0	S-S	26.9	0.0	1.5	C	0.39	85.8	7.14	0.19	1.35	151	Yes
Darfield	Shirley Library	2010	7.0	S-S	51.0	22.3	22.3	C	0.16	65.7	8.76	1.95	1.84	157	Yes
Parkfield	PARKFIELD - EADES	2004	6.0	S-S	10.0	1.4	2.9	B	0.45	35.9	1.22	0.37	0.81	41	Yes
Parkfield	Slack Canyon	2004	6.0	S-S	31.5	1.6	3.0	B	0.35	53.2	0.85	1.60	2.29	0	No
Parkfield	Parkfield - Cholame 1E	2004	6.0	S-S	11.4	1.7	3.0	C	0.48	51.7	1.33	0.93	0.90	58	Yes
Parkfield	Parkfield - Cholame 2WA	2004	6.0	S-S	11.5	1.6	3.0	D	0.55	57.9	1.08	1.35	1.54	67	Yes
Parkfield	Parkfield - Cholame 3E	2004	6.0	S-S	11.9	5.0	5.6	B	0.62	31.0	0.52	0.96	1.66	66	Yes
Parkfield	Parkfield - Cholame 3W	2004	6.0	S-S	12.2	2.6	3.6	C	0.55	43.4	1.02	0.87	0.99	27	Yes
Parkfield	Parkfield - Cholame 4W	2004	6.0	S-S	12.3	3.3	4.2	B	0.58	38.3	0.70	1.00	1.33	43	Yes
Parkfield	Parkfield - Fault Zone 1	2004	6.0	S-S	8.4	0.0	2.5	D	0.73	82.0	1.19	1.98	1.84	13	No
Parkfield	Parkfield - Fault Zone 9	2004	6.0	S-S	10.0	1.2	2.9	B	0.16	27.0	1.13	-0.21	0.56	63	Yes
Parkfield	Parkfield - Fault Zone 12	2004	6.0	S-S	11.0	0.9	2.7	C	0.38	56.6	1.19	0.98	1.54	49	Yes
Parkfield	Parkfield - Stone Corral 1E	2004	6.0	S-S	7.2	2.9	3.8	C	0.85	43.4	0.57	0.88	1.27	56	Yes
Chi-Chi	CHY006	1999	7.6	R-O	40.5	9.8	9.8	B	0.32	58.3	2.57	0.52	1.25	291	Yes
Chi-Chi	CHY101	1999	7.6	R-O	32.0	9.9	9.9	C	0.39	108.9	5.34	1.35	1.86	6	No
Chi-Chi	TCU026	1999	7.6	R-O	106	56.0	56.1	B	0.11	45.7	8.37	2.29	2.52	57	No
Chi-Chi	TCU029	1999	7.6	R-O	79.2	28.0	28.0	B	0.23	62.7	5.29	1.67	2.53	155	No
Chi-Chi	TCU031	1999	7.6	R-O	80.1	30.2	30.2	B	0.11	63.3	5.93	1.96	2.51	123	Yes
Chi-Chi	TCU033	1999	7.6	R-O	93.1	40.9	40.9	B	0.16	41.6	8.97	1.41	2.35	71	No
Chi-Chi	TCU034	1999	7.6	R-O	87.9	35.7	35.7	B	0.27	45.2	8.87	1.33	2.16	72	No

(continues on next page)

Earthquake Name	Station Name	Year	M	Fault Mech.	R <sub>epi</sub> km	R <sub>JB</sub> km	Clst D km	EN-1998 Site class	PGA g	PGV cm/s	T <sub>p</sub> s	ε <sub>PGV</sub>	ε <sub>Sa(T<sub>p</sub>)</sub>	Azimuth deg.	FN Pulse
Chi-Chi	TCU036	1999	7.6	R-O	67.8	19.8	19.8	B	0.13	63.2	5.38	1.46	2.47	131	Yes
Chi-Chi	TCU040	1999	7.6	R-O	69.0	22.1	22.1	B	0.11	47.5	6.43	0.80	1.74	162	No
Chi-Chi	TCU046	1999	7.6	R-O	68.9	16.7	16.7	B	0.14	31.3	8.04	0.01	1.38	112	Yes
Chi-Chi	TCU059	1999	7.6	R-O	53.4	17.1	17.1	C	0.13	64.1	7.78	0.89	1.69	45	No
Chi-Chi	TCU063	1999	7.6	R-O	35.5	9.8	9.8	B	0.17	79.0	6.55	1.14	1.70	136	Yes
Chi-Chi	TCU065	1999	7.6	R-O	26.7	0.6	0.6	C	0.81	136.7	5.74	0.36	1.15	113	Yes
Chi-Chi	TCU075	1999	7.6	R-O	20.7	0.9	0.9	B	0.31	105.0	5.00	0.47	1.13	109	Yes
Chi-Chi	TCU087	1999	7.6	R-O	55.6	7.0	7.0	B	0.12	45.4	10.4	-0.05	1.18	91	Yes
Chi-Chi	TCU101	1999	7.6	R-O	45.1	2.1	2.1	B	0.18	76.7	10.3	-0.24	0.67	70	No
Chi-Chi	TCU103	1999	7.6	R-O	52.4	6.1	6.1	B	0.13	67.1	8.69	0.44	1.39	75	No
Morgan Hill	Hollister Diff Array #1	1984	6.2	S-S	52.8	26.4	26.4	C	0.10	12.3	1.28	0.22	0.54	58	Yes
Northridge	Wadsworth VA, N. Grounds	1994	6.7	R	19.6	14.6	23.6	B	0.27	32.4	2.36	1.02	0.96	32	Yes
Bam	Bam	2003	6.6	S-S	12.6	0.1	1.7	B	0.81	124.2	2.02	1.76	1.61	277	Yes
South Napa	Napa Fire Station 3	2014	6.0	S-S	12.3	-	3.3	C	0.41	74.2	4.44	1.97	1.78	62	Yes
South Napa	Huichica Creek	2014	6.0	S-S	3.5	-	4.4	C	0.30	21.5	2.74	-0.09	0.33	284	No
South Napa	Lovall Valley Loop Road	2014	6.0	S-S	12.0	-	6.4	C	0.25	33.0	3.44	1.06	0.44	21	Yes
South Napa	Napa College	2014	6.0	S-S	7.1	-	4.5	C	0.26	42.1	1.88	1.13	0.91	296	Yes

R<sub>epi</sub>: Epicentral distance.

R<sub>JB</sub>: Closest distance to horizontal projection of the fault plane.

ClstD: Closest distance to the fault plane.

Rupture mechanisms S-S: Strike-Slip, R: Reverse, N: Normal, N-O: Normal-Oblique, R-O: Reverse-Oblique.

PGA: Peak Ground Acceleration of the rotated pulse-like component.

PGV: Peak Ground Velocity of the rotated pulse-like component.

T<sub>p</sub>: Pulse period according to Baker (2007), Shahi and Baker (2014).

ε<sub>PGV</sub>: Number of (logarithmic) standard deviations between the PGV of the pulse-like component and the median GMPE prediction of Boore and Atkinson (2008) - GMPE not corrected for NS directivity.

ε<sub>Sa(T<sub>p</sub>)</sub>: Number of (logarithmic) standard deviations between pseudo spectral acceleration of the pulse-like component at a period of vibration equal to the pulse period T<sub>p</sub> and the corresponding median GMPE prediction of Boore and Atkinson (2008) - GMPE not corrected for NS directivity.

Azimuth: Angle of considered pulse-like component with respect to the north, measured clockwise (towards the east).

FN pulse: Pulse-like component considered is found within 30° from the strike-normal direction.





## APPENDIX C

*Parameter estimates for Equations (5.7) and (5.9) - Chapter 5.*

Table C.1. Parameter estimates for Equation (5.7), hardening case.

Term	$a_{x\%}$		
	$\theta_{16\%}$	$\theta_{50\%}$	$\theta_{84\%}$
1	-0.0579	0.709	0.3563
$\alpha_h^2$	1.143	0.9455	1.673
$(T/T_p)$	0.05928	-1.091	-0.8523
$\alpha_h \cdot (T/T_p)$	2.211	-0.5751	-1.459
$\alpha_h^3 \cdot (T/T_p)$	-6.639	-1.467	-1.677
$(T/T_p)^2$	0.2184	0.391	0.3602
$\alpha_h \cdot (T/T_p)^2$	-7.46	1.235	3.385
$\alpha_h^2 \cdot (T/T_p)^2$	8.41	-0.4376	-2.392
$\alpha_h^3 \cdot (T/T_p)^2$	3.486	0.8756	1.031
$\alpha_h \cdot (T/T_p)^3$	2.993	-0.469	-1.38
$\alpha_h^2 \cdot (T/T_p)^3$	-4.379	0.04628	0.9802
$(T/T_p)^{-1}$	0.01686	-0.05234	0.03751
$\alpha_h \cdot (T/T_p)^{-1}$	-0.18	-0.2762	-0.3229
$\alpha_h \cdot (T/T_p)^{-2}$	0.009609	0.02143	0.01129

Table C.2. Parameter estimates for Equation (5.7), hardening case.

Term	$b_{x\%}$		
	$\theta_{16\%}$	$\theta_{50\%}$	$\theta_{84\%}$
1	0.9399	0.1484	1.391
$(T/T_p)$	-0.06906	-0.4983	-0.08103
$\alpha_h \cdot (T/T_p)$	0.08591	1.34	0.05425
$\alpha_h^3 \cdot (T/T_p)$	0.1857	0.6156	1.06
$(T/T_p)^2$	0.1156	-0.4888	-0.1534
$\alpha_h \cdot (T/T_p)^2$	-1.754	-1.791	-2.974
$\alpha_h^2 \cdot (T/T_p)^2$	1.831	1.257	1.819
$\alpha_h \cdot (T/T_p)^3$	0.6658	0.776	1.359
$\alpha_h^2 \cdot (T/T_p)^3$	-0.8087	-0.6114	-1.016
$(T/T_p)^{-1}$	-0.007072	0.0704	-0.06475
$\alpha_h \cdot (T/T_p)^{-1}$	-0.002928	0.242	-0.2341
$\alpha_h \cdot (T/T_p)^{-2}$	0.002318	-0.02144	0.03188

Table C.3. Parameter estimates for Equation (5.7), hardening case.

Term	$c_{x\%}$		
	$\theta_{16\%}$	$\theta_{50\%}$	$\theta_{84\%}$
1	-0.7705	0.00	0.4972
$\alpha_h^2$	-0.3457	-	-0.9563
$(T/T_p)$	2.528	-	-0.64
$\alpha_h \cdot (T/T_p)$	-1.805	-	0.1551
$(T/T_p)^2$	-0.8327	-	0.1908
$\alpha_h^2 \cdot (T/T_p)^3$	0.3976	-	0.08431
$\alpha_h \cdot (T/T_p)^{-1}$	0.3336	-	0.2391
$\alpha_h \cdot (T/T_p)^{-2}$	-0.03537	-	-0.02022
$\ln^2(T/T_p)$	0.1562	-	-0.061

Table C.4. Parameter estimates for Equation (5.7), hardening case.

Term	$d_{x\%}$		
	$\theta_{16\%}$	$\theta_{50\%}$	$\theta_{84\%}$
1	1.07	1.00	0.9576
$\alpha_h^2$	0.0316	-	0.1033
$\alpha_h \cdot (T/T_p)$	-0.1796	-	-0.04133
$(T/T_p)^2$	0.04143	-	0.1901
$\alpha_h \cdot (T/T_p)^{-1}$	-0.00396	-	-0.00281
$\ln^2(T/T_p)$	-0.01293	-	-0.00543

Table C.5. Parameter estimates for Equation (5.9), softening case.

Term	$a_{x\%}$		
	$\theta_{16\%}$	$\theta_{50\%}$	$\theta_{84\%}$
1	46.78	102.4	122.9
$ \alpha_c  \cdot (T/T_p)$	-29.32	-61.87	-74.7
$ \alpha_c ^3 \cdot (T/T_p)$	0.6924	1.534	1.894
$ \alpha_c  \cdot (T/T_p)^2$	20.94	42.47	50.66
$ \alpha_c ^3 \cdot (T/T_p)^2$	-0.2796	-0.6327	-0.7733
$ \alpha_c  \cdot (T/T_p)^3$	-4.739	-9.19	-10.86
$(T/T_p)^{-1}$	-1.173	-2.141	-2.619
$( \alpha_c +1)^{-1}$	-45.32	-102.6	-122.7
$( \alpha_c +1)^{-4}$	69.34	146.2	170.3
$ \alpha_c  \cdot (T/T_p)^{-1}$	-1.547	-3.867	-4.703
$ \alpha_c  \cdot (T/T_p)^{-2}$	0.1182	0.2859	0.35

Table C.6. Parameter estimates for Equation (5.9), softening case.

Term	$b_{x\%}$		
	$\theta_{16\%}$	$\theta_{50\%}$	$\theta_{84\%}$
1	62.92	102.3	132.6
$ \alpha_c  \cdot (T/T_p)$	-36.83	-59.61	-77.89
$ \alpha_c ^3 \cdot (T/T_p)$	0.8968	1.475	1.967
$ \alpha_c  \cdot (T/T_p)^2$	25.00	40.31	52.18
$ \alpha_c ^3 \cdot (T/T_p)^2$	-0.3636	-0.6126	-0.8093
$ \alpha_c  \cdot (T/T_p)^3$	-5.377	-8.576	-11.03
$(T/T_p)^{-1}$	-0.8819	-1.585	-2.197
$( \alpha_c +1)^{-1}$	-64.59	-105.3	-135.8
$( \alpha_c +1)^{-4}$	92.95	150.3	190.2
$ \alpha_c  \cdot (T/T_p)^{-1}$	-2.375	-4.031	-5.21
$ \alpha_c  \cdot (T/T_p)^{-2}$	0.1599	0.281	0.3673

